UTPP-67

Measurement of the Photon Angular Distribution in the W+Photon Production in 1.8 TeV Proton-Antiproton Collisions

Makoto SHIMOJIMA

A dissertation submitted to the Doctoral Program
in Physics, the University of Tsukuba
in partial fulfillment of the requirements
for the degree of Doctor of Philosophy (Science)

January, 1997

Measurement of the Photon Angular Distribution in the W+Photon Production in 1.8 TeV Proton-Antiproton Collisions

January 1997

Makoto SHIMOJIMA

A dissertation submitted to the Doctoral Program

in Physics, the University of Tsukuba

in partial fulfillment of the requirements for the

degree of Doctor of Philosophy (Science)

Abstract

As a novel test of the gauge sector of the Standard Model of electroweak interactions, we present here the first measurement of the photon angular distribution in the Wγ production in $p\bar{p}$ interactions at $\sqrt{s} = 1.8$ TeV, which was carried out with the CDF detector at the Fermilab Tevatron. The photon angular distribution is of particular interest because the Standard Model predicts a presence of a *radiation amplitude zero*, which arises from a complete destructive interference between the Wγ production processes. The radiative W decay processes however tend to fill this zero and distinguishing the production processes from the radiative W decay processes is one of the key issues in this analysis.

In the 110 pb^{-1} of CDF data collected during the 1992–1995 run (Run I), we looked for isolated photons in W inclusive samples and obtained 202 candidate events in the electron and muon channels for central photons with transverse momentum $P_T > 7$ GeV/c which were separated from the charged lepton by more than 0.7 in pseudorapidity-phi space. From this sample radiative decay events were further suppressed by requiring the minimum 3-body invariant mass to be larger than 80.41 GeV and by tightening the lepton-photon angular separation cut from 0.7 to 1.5; a total of 56 events survived.

The photon angular distribution is plotted in the Wγ rest frame using these 56 events. The distribution is compared with the Standard Model predictions including background contributions such as W + *jets* where a jet fakes a photon, and with

the flat signal hypothesis, where the Standard Model predictions were replaced with a flat distribution. The data were found to be consistent with the Standard Model predictions at the 80% significance level and with the flat signal distribution only at the 44% level, implying presence of a radiation amplitude zero, as expected by the Standard Model.

Acknowledgements

I would like to express my appreciation to Professor Koji Takikawa, my thesis advisor and the leader of the Japanese CDF collaboration, for his guidance and encouragements throughout my graduate career. He has provided me with advice in many phases of my study.

I would like to thank Professor Kuni Kondo, our ex-leader, for giving me the opportunity to join the CDF collaboration and for his continuous support.

Professor Itsuo Nakano and Professor K. Hara taught me how and what to consider in a physics experiment. It has been they from whom I learned how to work out a task of various degrees of difficulty. It was fun spending a whole summer with them at Urbana-Champaign building CMP chambers, too.

Professor S. Kim is appreciated for his continuous encouragement and criticism towards my work.

Discussion with the Diboson Group members, especially with Professor Steve Errede, Dr. Doug Benjamin, and Dr. Bob Wagner, was vital and very helpful. Steve provided us with the FMC fast detector simulation program.

Professor Ulrich Baur kindly let us use his Monte Carlo program for this analysis and gave prompt answers to my naive questions.

I would like to thank Professor Tony Liss for his generous hospitality during my stay at the University of Illinois at Urbana-Champaign.

I enjoyed working as an ACE and as the HV expert during Run IA. I owe a lot

to Drs. Steve Hahn, Jim Haylen, Jim Patrick, Aseet Mukherjee, and other detector experts.

Encouragements from various people including Drs. Larry Nodulman, Fumi Ukegawa, and Mark Samuel are very much appreciated.

I would like to thank the Fermilab staff and the technical staff of the participating institutions for their vital contributions. This work was supported by the Ministry of Education, Science and Culture of Japan, the U.S. Department of Energy, and the National Science Foundation.

Contents

List of Tables

List of Figures

Chapter 1

Introduction

The Standard Electroweak Theory of Weinberg, Glashow, and Salam [1,3–5] is extremely successful in explaining various experimental results — at present, experiment and theory agree at the 0.1–1% level in the determination of the vector boson couplings to the various fermions. It is however not as well understood in some areas, one important component being the non-Abelian self couplings of the weak vector gauge bosons. This is mainly due to very small cross sections of the processes involving two bosons. Table 1.1 lists the expected total production cross sections and event yields of various diboson processes at the Tevatron energies. Until recently, before the first W pair event at LEP 2 was recorded on 10th July, 1996 [58], Tevatron at Fermilab was the only accelerator that accelerated beams to high enough energy to produce W bosons (after the S$\bar{\text{p}}$pS at CERN stopped its operation in 1990).

The production of Wγ pairs provides an excellent opportunity to study the WWγ

Gauge Boson Pair Process	Total Production Cross Section (pb)	50 pb^{-1} Event Yield
WW	6.0	10
WZ	1.2	0.5
ZZ	0.7	0.1
Wγ	10.0	75
Zγ	9.0	20

Table 1.1: Diboson total production cross sections in pb at the Tevatron energy. The WW, WZ, and ZZ entries are summed over all e-μ final state combinations. The Wγ and Zγ yields assume that the photon passes an E_T cut of 10 GeV. [41]

vertex. This process is of particular interest because it involves interaction between bosons due to the non-Abelian nature of the underlying gauge theory and any deviations from the theoretical expectations would imply the presence of new physics, perhaps arising from unexpected internal structure or loop corrections involving propagator of new particles.

The Wγ process in addition has a rather distinctive characteristics that the amplitude of the Wγ process vanishes ("radiation amplitude zero") at $\cos\theta^*_\gamma = 1-2Q_q/Q_W$, where θ^*_γ is the angle between the photon and the incoming quark in the Wγ rest frame; and Q_q and Q_W are the charges of the incoming quark and the W boson. This zero results directly from the complete destructive interference at the tree level of the radiation patterns off the incoming quark/antiquark and outgoing W boson.

1.1 Wγ Physics

The tree-level Feynman diagrams for Wγ processes are shown in Figure 1.1. The s-channel diagram in Figure 1.1(a) contains the tri-linear gauge couplings of the WWγ vertex. The other two diagrams are the u- and t-channel processes associated with initial state radiation off the incoming quark/antiquark lines. Figure 1.1(b) is the radiative W decay, where the on-shell W boson radiates a photon before decaying into leptons. Figure 1.1(c) describes the final state inner Bremsstrahlung radiation off the decay lepton. Because of the finite width of the W boson, all of these diagrams must be included in the calculation of the Wγ cross section to preserve electromagnetic gauge invariance. [39]

These subprocesses however occupy different regions of kinematical space. The initial state radiation is sharply peaked in angle along the incident quark/antiquark direction. The photons from final state radiation tend to be collinear with the decay lepton. The E_T spectra of photons from initial and final state radiation are sharply peaked at low photon energies as in the case of radiative W decay. The photons from the WWγ vertex on the other hand are not strongly correlated with the decay lepton and are not bounded by the mass of the W boson.

The effective Lagrangian is given by [19]

$$\mathcal{L}_{WW\gamma} = -ie\{(W^{\dagger}_{\mu\nu}W^{\mu}A^{\nu} - W^{\dagger}_{\mu}A_{\nu}W^{\mu\nu})$$

$$+\kappa_f W_\mu^\dagger W_\nu F^{\mu\nu} + \frac{\lambda_f}{M_W^2} W_{\lambda\mu}^\dagger W_\nu^\mu F^{\nu\lambda}$$
$$+\tilde{\kappa}_f W_\mu^\dagger W_\nu \tilde{F}^{\mu\nu} + \frac{\tilde{\lambda}_f}{M_W^2} W_{\lambda\mu}^\dagger W_\nu^\mu \tilde{F}^{\nu\lambda}\}, \quad (1.1)$$

where A^μ and W^μ are the photon and W^- fields, and $W_{\mu\nu} = \partial_\mu W_\nu - \partial_\nu W_\mu$, $F_{\mu\nu} = \partial_\mu A_\nu - \partial_\nu A_\mu$, and $\tilde{F}_{\mu\nu} = \frac{1}{2}\,\epsilon_{\mu\nu\rho\sigma}\,F^{\rho\sigma}$; and e is the charge of the proton and M_W is the mass of the W boson.

The first term in Eq. 1.1 arises from minimal coupling of the photon to the $W^\pm$ fields and is completely fixed by the charge of the W boson for on-shell photons. In the static limit ($E_\gamma \to 0$), the κ and λ terms are related to the magnetic dipole moment μ_W and the electric quadrupole moment Q_W of the W while $\tilde{\kappa}$ and $\tilde{\lambda}$ terms are related to the electric dipole moment d_W and the magnetic quadrupole moment $\tilde{Q}_W$ of the W:

$$\mu_W = \frac{e}{2M_W}(1 + \kappa_f + \lambda_f), \quad (1.2)$$
$$Q_W = -\frac{e}{M_W^2}(\kappa_f - \lambda_f), \quad (1.3)$$
$$d_W = \frac{e}{2M_W}(\tilde{\kappa}_f + \tilde{\lambda}_f), \quad (1.4)$$
$$\tilde{Q}_W = -\frac{e}{M_W^2}(\tilde{\kappa}_f - \tilde{\lambda}_f). \quad (1.5)$$

The couplings κ_f and λ_f do not violate any discrete symmetries, but $\tilde{\kappa}_f$ and $\tilde{\lambda}_f$ are P-odd and violate CP.

The cross section of the Wγ process generally increases with $\hat{s}$. To preserve uni-

tarity at asymptotically high energies, the couplings a_f $(= \kappa_f - 1,\ \lambda_f,\ \tilde{\kappa}_f,\ \tilde{\lambda}_f)$ are assumed to be of the form [19]

$$a_f(\hat{s}, q_W^2 = M_W^2, q_\gamma^2 = 0) = \frac{a_0}{(1 + \frac{\hat{s}}{\Lambda^2})^{n_f}}, \tag{1.6}$$

where a_0 is the dimensionless anomalous parameter $\kappa - 1 \equiv \Delta\kappa$, λ, $\tilde{\kappa}$, or $\tilde{\lambda}$. The form factor scale Λ represents the scale at which new physics becomes observable in the weak boson sector due for example to compositeness of the W boson. The value of the exponent n_f is quite arbitrary — it can take any number $> \frac{1}{2}$ for $\Delta\kappa$ and $\tilde{\kappa}$ and > 1 for λ and $\tilde{\lambda}$ — but is usually set to 2 to guarantee the same behaviour for all the terms at high energies.

Within the Standard Model, at tree-level,

$$\Delta\kappa = \lambda = \tilde{\kappa} = \tilde{\lambda} = 0. \tag{1.7}$$

1.2 Radiation Amplitude Zero

Beside the fact that the Wγ process has the largest cross section among the diboson processes in Table 1.1 [41], what makes the Wγ process particularly interesting and important is the presence of (or its lack of) the phenomenon called *radiation ampli-*

tude zero (or RAZ for short).[1] In their September 1979 paper [10], K.O.Mikaelian, M.A.Samuel, and D.Sahdev brought us a big surprise: while calculating the production cross section of photon associated with then undiscovered W bosons they found a pronounced zero in the photon angular distribution for $q\bar{q}' \to \mathrm{W}\gamma$ at

$$\cos\theta^*_\gamma = 1 - \frac{2Q_q}{Q_\mathrm{W}} \tag{1.8}$$

when the gauge theory couplings were assumed (Eq. 1.7). Figure 1.2 is the original W angular distribution in the Wγ rest frame [10], where $\theta_{\mathrm{c.m.}}$ is the angle between the W and the incoming quark and is related to the above θ^*_γ by $\theta_{\mathrm{c.m.}} = \pi - \theta^*_\gamma$, as defined in Figure 1.3. In the abstract the authors stated that "...We can offer no explanation for this behavior." Fortunately it did not need so much time to solve the puzzle for some simple cases and a number of papers followed soon afterwards discussing about the zeros. [11,13–15]

Consider a vertex of three charged particles (Figure 1.4). To get the scattering amplitude for these particles plus a photon, we attach the photon to each leg in turn and sum the diagrams. Ignoring the overall constant factors, the amplitude is given by

$$\mathcal{M} \sim \sum_{i=1}^{3} \frac{A_i B_i}{C_i}, \tag{1.9}$$

where A_i is the charge factor, B_i is the polarisation-dependent factor, and C_i is the

[1] Actually the cross section of the Wγ process would be much larger if the radiation amplitude zero discussed in this section did not exist.

propagator denominator of diagram i. The authors of [13] found that given the conditions

$$\sum_{i=1}^{3} A_i = \sum_{i=1}^{3} B_i = \sum_{i=1}^{3} C_i = 0, \tag{1.10}$$

which follow from charge conservation, energy-momentum conservation, and properties of the photon ($q^2 = 0$ and $q \cdot \epsilon = 0$), Eq. 1.9 can be factored into two terms, one term containing all the dependence on the charge or other internal-symmetry indices, and the other term containing the dependence on the spin or polarisation indices:

$$\begin{aligned}
\sum_{i=1}^{3} \frac{A_i B_i}{C_i} &= \frac{1}{C_3}(A_1 C_2 - A_2 C_1)(\frac{B_2}{C_2} - \frac{B_1}{C_1}) && (1.11)\\
&= \frac{1}{p_3 \cdot q}[Q_1(p_2 \cdot q) - Q_2(p_1 \cdot q)](\frac{B_2}{p_2 \cdot q} - \frac{B_1}{p_1 \cdot q}) && (1.12)\\
&= 0 \text{ when } \frac{Q_1}{p_1 \cdot q} = \frac{Q_2}{p_2 \cdot q} && (1.13)
\end{aligned}$$

using the kinematical variables in Figure 1.4.

For $q\bar{q}' \rightarrow \mathrm{W}\gamma$, we have

$$\begin{aligned}
Q_1 &= Q_q, && (1.14)\\
Q_2 &= Q_{\bar{q}'} = Q_{\mathrm{W}} - Q_q, && (1.15)\\
p_1 &= (|\vec{p}|; +\vec{p}), && (1.16)\\
p_2 &= (|\vec{p}|; -\vec{p}); && (1.17)
\end{aligned}$$

and Eq. 1.8 follows nicely.

The condition in Eq. 1.13 is in fact a special case for a more general theorem [14] for tree-level N particles of spin ≤ 1 and the connection between gauge-boson couplings and Poincaré transformations has since been discovered. [15]

Recently, a similar zero, though only an approximate zero unlike the exact zero in the Wγ production, was also calculated in the WZ production amplitude, as shown in Figure 1.5. [47]

When anomalous couplings are introduced, the radiation amplitude zero disappears because the amplitude can no longer be factored. For example, with arbitrary $\Delta\kappa$,

$$\begin{aligned}\frac{d\sigma}{dt}(q_i\bar{q}_j \to \mathrm{W}^-\gamma) &= \frac{\alpha}{s^2}\frac{\mathrm{M_W^2}G_F}{\sqrt{2}}g_{ij}^2 \ \{ \\ &\quad (Q_i + \frac{1}{1+t/u})^2\frac{t^2+u^2+2s\mathrm{M_W^2}}{tu} \\ &\quad +\Delta\kappa(Q_i + \frac{1}{1+t/u})\frac{t-u}{t+u} \\ &\quad +\frac{\Delta\kappa^2}{2(t+u)^2}[tu + (t^2+u^2)\frac{s}{4\mathrm{M_W^2}}] \ \}. \quad (1.18)\end{aligned}$$

where s, t, and u are Mandelstam variables with

$$t = -\frac{s-\mathrm{M_W^2}}{2}(1+\cos\theta_\gamma^*), \quad (1.19)$$

$$u = -\frac{s-\mathrm{M_W^2}}{2}(1-\cos\theta_\gamma^*), \quad (1.20)$$

G_F is the Fermi coupling constant, $\alpha = e^2/4\pi$, and

$$g_{ij} = \begin{cases} \cos\theta_C & \text{for } q_i\bar{q}_j = d\bar{u} \text{ and } s\bar{c}, \\ \sin\theta_C & \text{for } q_i\bar{q}_j = s\bar{u} \text{ and } d\bar{c}. \end{cases} \tag{1.21}$$

A more complete amplitude with other anomalous couplings may be found in [39].

In $p\bar{p}$ collisions, the colliding partons are not identified so we usually sum over possible partons using the proton structure functions. For the angular distribution of $W^-\gamma$ production: [10]

$$\begin{aligned} \frac{d\sigma}{d\cos\theta_{\text{c.m.}}}(p\bar{p} \;&\rightarrow\; W^-\gamma X) \\ &= \frac{1}{3}\sum_{i=d,s}\iint dx_A dx_B P_i^p(x_A) P_{\bar{u}}^{\bar{p}}(x_B)\left(\frac{s-M_W^2}{2}\right)\frac{d\sigma}{dt}(q_i\bar{q}_u \rightarrow W^-\gamma) \\ &+ \frac{1}{3}\sum_{i=d,s}\iint dx_A dx_B P_{\bar{u}}^p(x_A) P_i^{\bar{p}}(x_B)\left(\frac{s-M_W^2}{2}\right)\frac{d\sigma}{dt}(q_i\bar{q}_u \rightarrow W^-\gamma)_{u\leftrightarrow t}. \end{aligned} \tag{1.22}$$

The zero condition is independent of s so the radiation amplitude zero is not affected by the integration over x_A or x_B but since the sea quark in the second term in Eq. 1.22 moves in the opposite direction (*i.e.*, $\theta = \pi - \theta_{\text{c.m.}}$), the zero is partially filled in. Fortunately the sea contributions are not very large at the Tevatron energy, so the radiation amplitude zero remains observable not only at the parton level but also in $p\bar{p}$ collisions.

Order α_s QCD corrections to the tree-level $W\gamma$ production is modest at the Teva-

tron centre of mass energy and the Born terms are as good an approximation in measuring anomalous couplings. [44]

1.3 Previous Measurements

There is no previous measurements of the photon angular distribution in the Wγ production. There are however some measurements of anomalous gauge boson self couplings, whose Standard Model values would imply the presence of the radiation amplitude zero.

The first direct measurement of the anomalous couplings came from the UA2 Collaboration in 1992 via $\bar{p}p \rightarrow e\nu\gamma + X$ at $\sqrt{s} = 630$ GeV: [42]

$$\begin{aligned} -3.5 &< \kappa < 5.9 \\ -3.6 &< \lambda < 3.5 \end{aligned} \qquad \text{UA2 1992 (95\% CL).} \tag{1.23}$$

The limits from the CDF Collaboration have not been updated and we still have rather loose limits from Run IA data: [51]

$$\begin{aligned} -2.3 &< \Delta\kappa < 2.2 \\ -0.7 &< \lambda < 0.7 \end{aligned} \qquad \text{CDF 1995 (95\% CL).} \tag{1.24}$$

The DØ Collaboration has just released their new limits: [56]

$$\begin{array}{rcl} -0.98 < \Delta\kappa < 1.01 \\ -0.33 < \lambda < 0.31 \end{array} \qquad \text{DØ 1996 (95\% CL).} \tag{1.25}$$

Figure 1.6 compares the expected sensitivities of the present and future accelerators to the anomalous couplings $\Delta\kappa$ and λ. [57]

1.4 Outline of the Thesis

The CDF group has been in a unique position in the analysis of the Wγ radiation amplitude zero in hadron collider experiments. The UA2 detector at S$\bar{\text{p}}$pS had never recorded enough Wγ candidates to look at a distribution and the DØ detector is not yet equipped with a central magnet so they cannot determine the charge of the electron[2], which determination is crucial in this analysis as will be discussed in Chapter 5. The LHC pp collider does not even exist yet and once built the Wγ events may suffer from severe higher-order corrections. In addition, the direction of the quark/antiquark is not known a priori in pp collisions so the zero would be even more difficult to observe.

This thesis describes the first measurement of the photon angular distribution, in $\text{p}\bar{\text{p}}$ collisions at $\sqrt{s} = 1.8$ TeV. Chapter 2 describes the Collider Detector at Fermilab

[2]They however do measure muon momenta.

(CDF), the apparatus we used to obtain the physics results. In Chapter 3 we describe our event selection, how each of the final state particles is identified in the analysis; We reduced the data sample from over a million of events recorded on tape down to 202 $W\gamma$ candidate events, which are compared with the Standard Model predictions in Chapter 4. Chapter 5 is devoted to the description of the measurement of the photon angular distribution. We show how various background processes are removed. The $W\gamma$ rest frame is reconstructed and the $\cos\theta^*_\gamma$ is defined in this chapter. The thesis concludes with the results presented in Chapter 6.

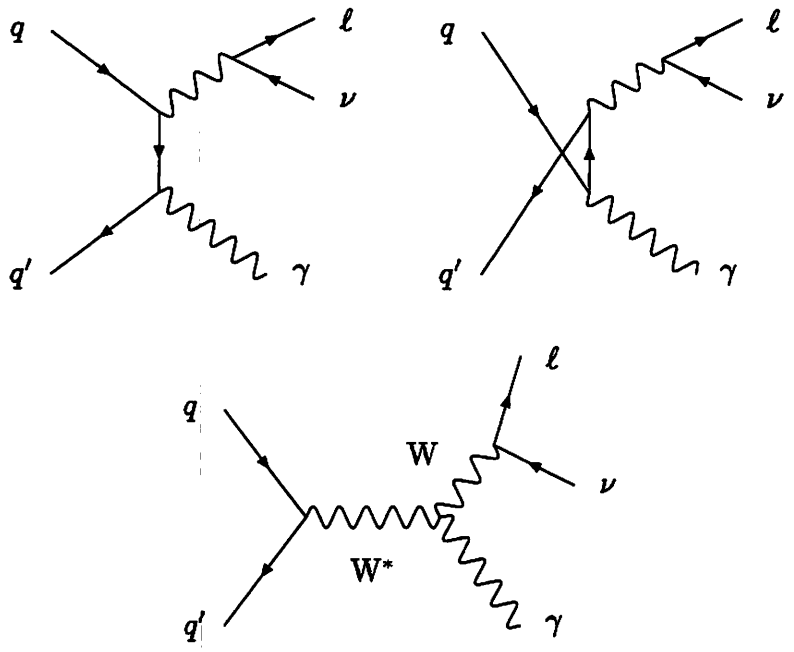

(a) Wγ production followed by W $\rightarrow$ $l\nu$ (t-,u-, and s-channels)

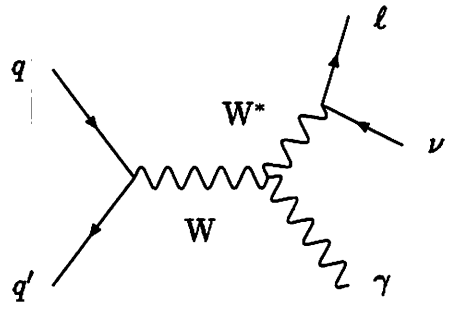

(b) radiative W decay followed by W* $\rightarrow$ $l\nu$

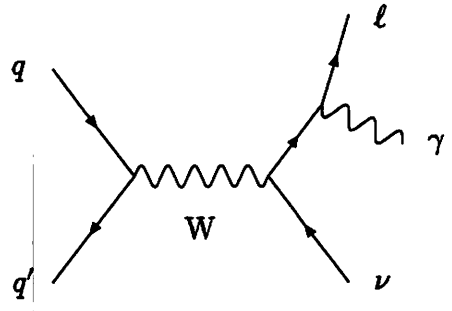

(c) W $\rightarrow$ $l\nu$ decay associated with radiation off the charged lepton.

Figure 1.1: Tree-level Wγ Feynman diagrams

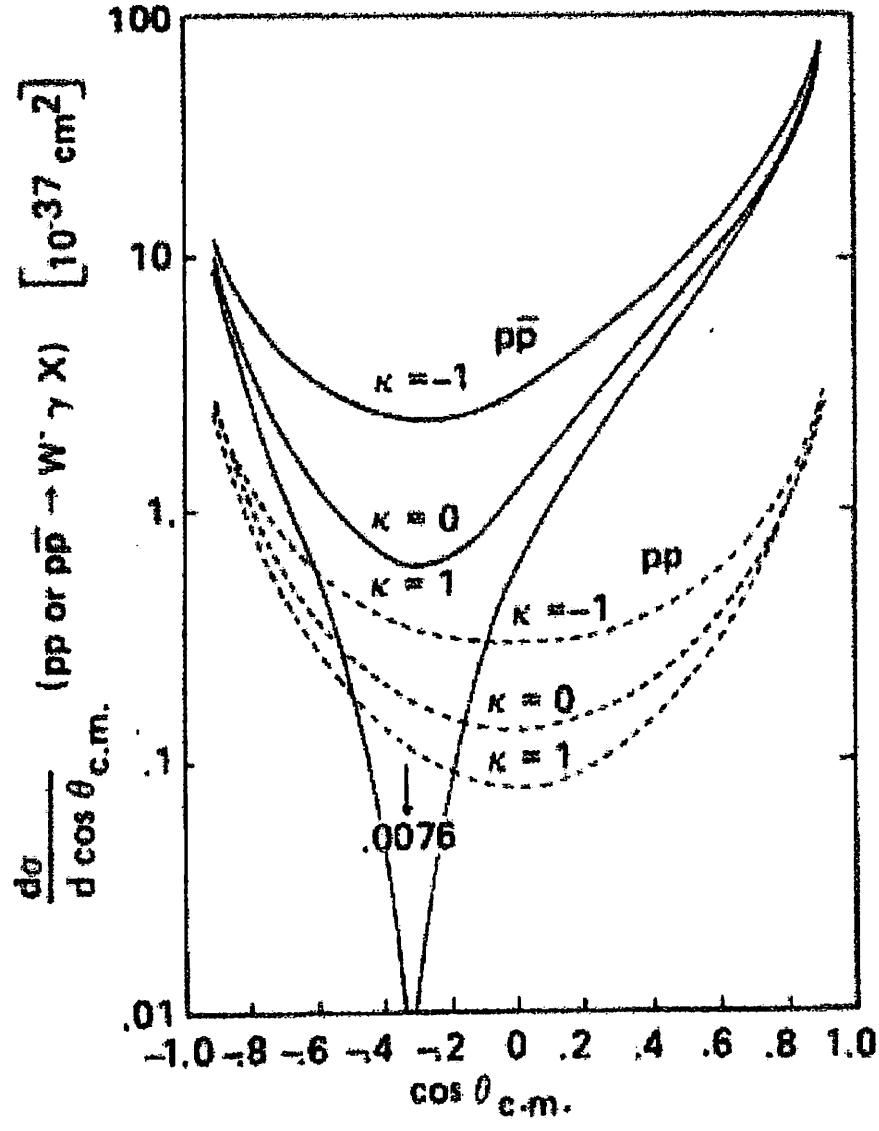

Figure 1.2: The differential cross sections for $pp \to W^-\gamma X$ and $p\bar{p} \to W^-\gamma X$, with a photon energy cut $E_\gamma > 30$ GeV calculated at $\sqrt{s} = 540$ GeV for $M_W = 85$ GeV. $\theta_{c.m.}$ is the angle between the W^- and the proton direction in the $W^-\gamma$ c.m. frame. [10]

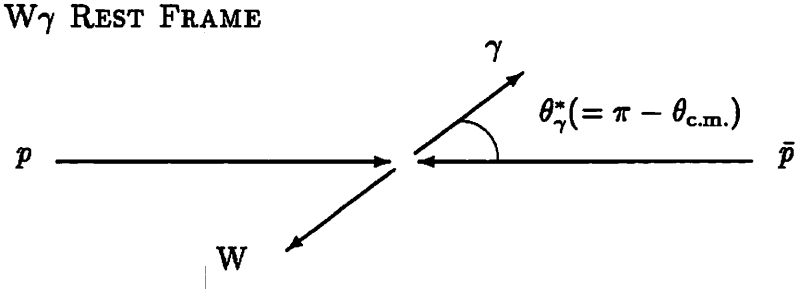

Figure 1.3: Definition of θ^*_γ assuming $\mathrm{P_T}(\mathrm{W}\gamma) = 0$. For θ^*_γ with finite $\mathrm{P_T}(\mathrm{W}\gamma)$ we use the Collins-Soper reference frame (cf. Eq. 5.4 and Figure 5.4).

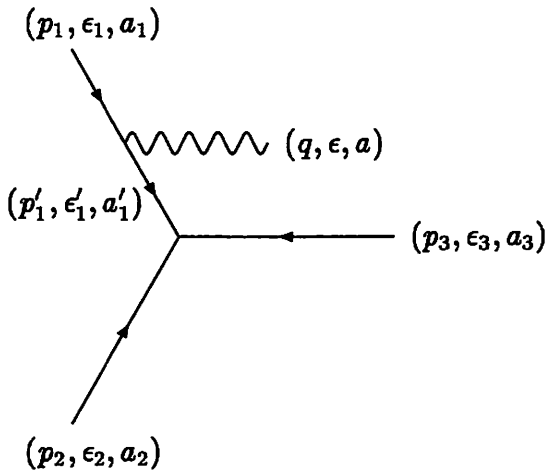

Figure 1.4: A tree-diagram: the p_i are incoming four momenta, the ϵ_i are polarisation vectors, and a_i are internal symmetry charges. Here the photon (p,ϵ,a) is attached to particle 1. There are two similar diagrams corresponding to cases where the photon is attached to particle 2 or 3.

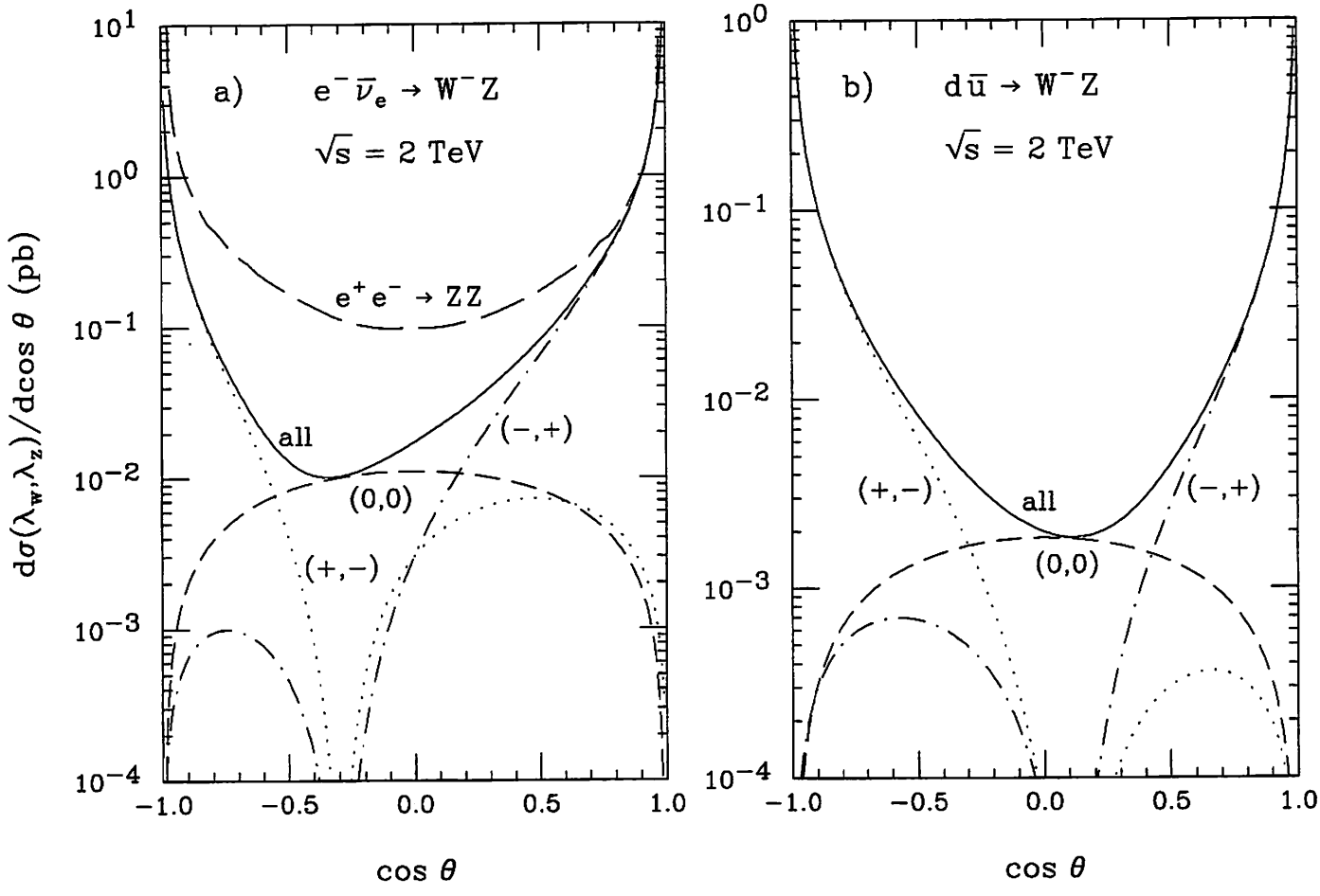

Figure 1.5: Approximate zeros in (a) $e^-\nu \to W^-Z$ and (b) $d\bar{u} \to W^-Z$ calculated at $\sqrt{s} = 2$ TeV. [47]

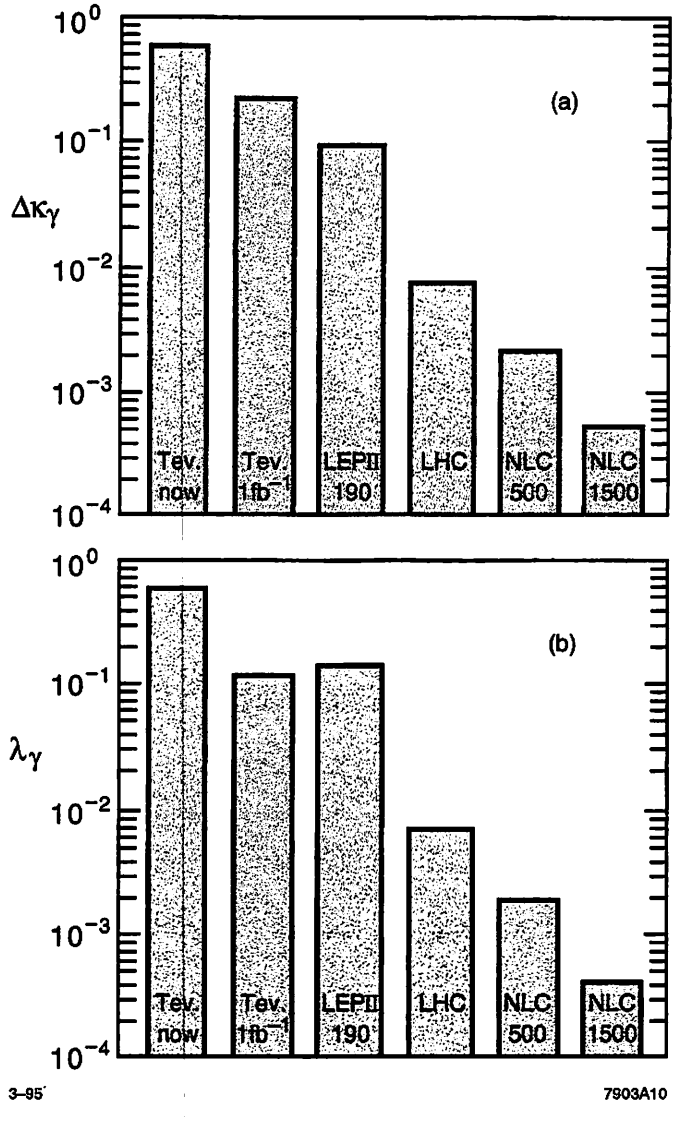

Figure 1.6: Comparison of representative 95% CL upper limits on $\Delta\kappa$ and λ for present and future accelerators. [57]

Chapter 2

The CDF Detector

The CDF (Collider Detector at Fermilab, Figures 2.1 and 2.2) [37] is a versatile 4π detector built to study $p\bar{p}$ collisions at the Fermilab Tevatron. The detector consists of a central, a pair of plug, and two identical forward/backward detectors. The central detector is a 2000 ton moveable[1] detector covering the region $30° < \theta < 90°$ (where the detector polar angle θ is defined in Eq. 2.4) and is made up of the 1.4 Tesla superconducting solenoidal magnet, steel yoke, tracking chambers, electromagnetic (EM) shower counters, hadron calorimeters, and muon chambers. The endplug detectors ($10° < \theta < 30°$) are equipped with electromagnetic and hadron calorimenters, and the forward/backward detectors ($2° < \theta < 10°$) include segmented time-of-flight counters, electromagnetic and hadron calorimeters, and muon toroidal spectrometers.

[1]To watch this massive detector move from the Assembly Hall to the Collision Hall was one of the breath-taking experiences during the installation of the CMUP chambers back in 1992; I still remember vividly — while it was moving we had to make sure all the gas/HV tubings did not get caught in the caterpillars less than an inch away!

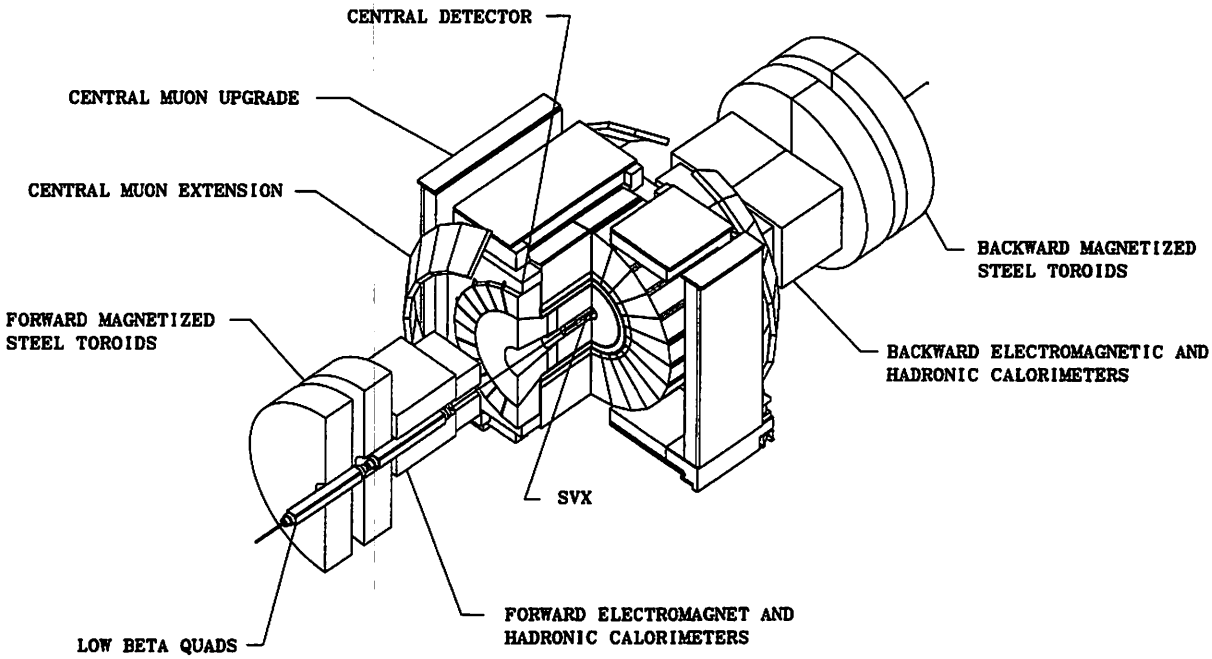

Figure 2.1: Perspective view of the CDF detector.

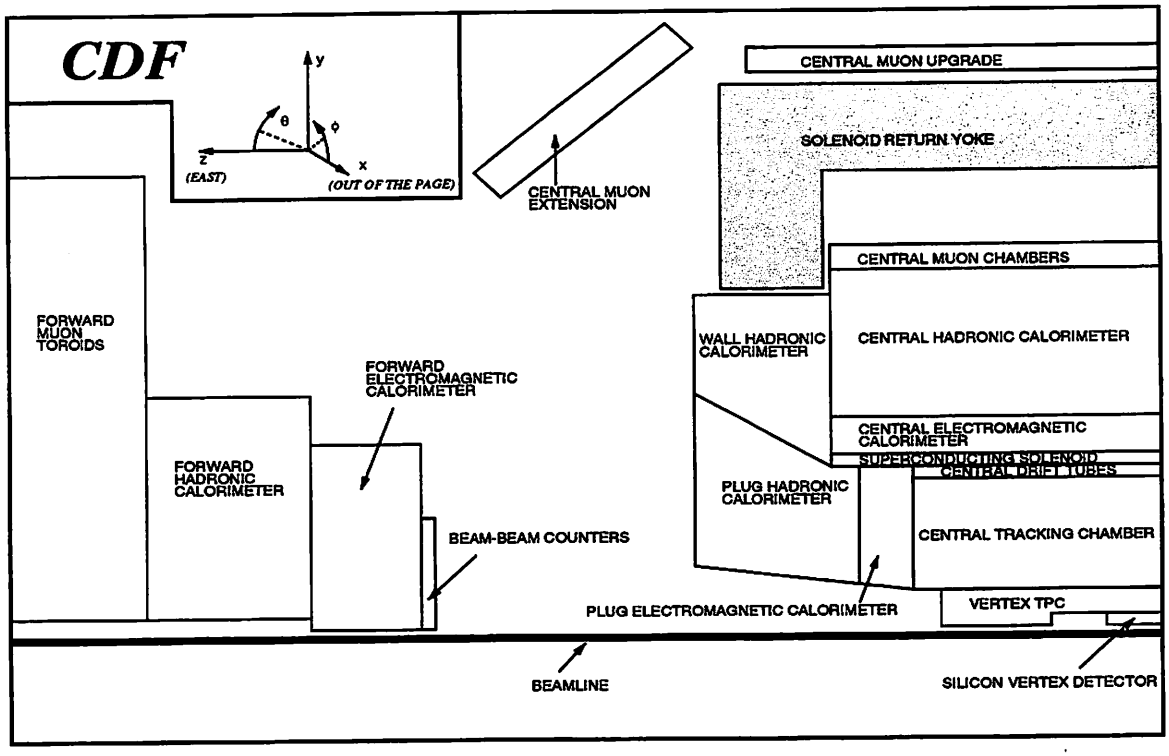

Figure 2.2: An elevation view of the CDF detector. Only a quarter of the detector is shown.

In this chapter we will describe each component of the CDF detector that is relevant to the analysis.

2.1 CDF Coordinate Systems

The CDF detector geometry is expressed in Cartesian coordinates (x,y,z) with the origin at the centre of the detector. The z-axis is along the proton direction and the y-axis points upwards; the x-axis is chosen to point radially out of the Tevatron ring to make the system right handed.

We employ other coordinate systems whenever convenient. For example, we often use the cylindrical coordinates with z, r, and ϕ in the central region, where the detector components are symmetrical about z. Here r is the radius in x-y plane and ϕ is the azimuthal angle which is 0 along the positive x-axis and increases with increasing y:

$$r = \sqrt{x^2 + y^2}, \tag{2.1}$$

$$\phi = \pi - \arctan \frac{y}{-x}. \tag{2.2}$$

The CDF calorimeters, which are arranged in projective towers, are mapped into 2 dimensional η-ϕ space, as shown in Figure 2.4. The size of the tower is typically

15° in azimuth and 0.1 in pseudorapidiy η, defined by

$$\eta = -\log \tan \frac{\theta}{2} \tag{2.3}$$

where θ is the polar angle with respect to the proton beam direction

$$\theta = \arctan \frac{r}{z}, \tag{2.4}$$

though we normally correct for event vertex z_0 when dealing with physical quantities:

$$\theta = \arctan \frac{r}{z - z_0}. \tag{2.5}$$

We use η rather than θ itself because energy flow in hadron colliders is roughly flat in η. The angle θ defined in Eq. 2.4 is used in Eq. 2.3 to obtain a *detector* η; and the angle θ defined in Eq. 2.5 is used for an *event* η.

We frequently view the detector in the plane transverse to the beam axis and find it useful to project energy and momentum in that plane:

$$\mathrm{P_T} = \sqrt{\mathrm{P_X}^2 + \mathrm{P_Y}^2}, \tag{2.6}$$

$$\mathrm{E_T} = \mathrm{E} \sin \theta. \tag{2.7}$$

The angular separation between two objects (tracks, energy deposits, etc.) is

measured in ΔR:

$$\Delta R = \sqrt{\Delta\eta^2 + \Delta\phi^2}, \tag{2.8}$$

which is invariant under Lorentz boost along the beam axis.

Some detectors have their own local coordinates. The CES strip chamber is an example.

2.2 Tracking System

Tracking chambers reside inside the superconducting solenoid in the central region. Together with the solenoid they allow precise momentum measurements of charged particles. We use two tracking chambers in this analysis.

2.2.1 Solenoid

The magnetic field is created with a NbTi/Cu superconducting solenoid [16], which is 3 m in diameter and is 5 m long. The nominal field is 1.4 Tesla at 4650 A, with the field pointing in the $-z$ direction. The flux is returned through a steel yoke outside the calorimeters.

The field was measured on the surface of the cylindrical volume when the solenoid was installed and is described precisely by a mapping function of 50 coefficients. In the middle of the tracking volume, B_Z varies $< 1\%$ from the centre to the maximum radius; it is 3–4% less at the ends of the volume but most of this fall off occurs very

close to the ends.

2.2.2 VTX

The vertex chamber (VTX) is our new event vertex finder. It replaces the old VTPC vertex time projection chamber [31] to cope with higher luminosities ($\mathcal{L} \sim 3 \times 10^{30}\text{cm}^{-2}\text{sec}^{-1}$). The VTX provides tracking information up to a radius of 22 cm and down to $\theta = 3.5°$ ($|\eta| < 3.5$). The resolution is about 1 mm along the z-axis.

The new VTX also provides room for the Silicon Vertex Detector (SVX), another new detector primarily used for secondary vertex detection, which proved very important in identifying the top quark events [46,52].

2.2.3 CTC

The central tracking chamber (CTC) [30] is a large cylindrical drift chamber that fits between the VTX and the solenoid, covering the region $40° < \theta < 140°$ ($|\eta| < 1.1$). It consists of 84 layers of sense wires of which 24 are tilted by $\pm 3°$ with respect to the beam direction for tracking in r-z plane. All wire cells are inclined at 45° relative to the radial direction from the z-axis to compensate for the drifting of electric charges in the magnetic field.

The resolution of a single hit point is about 200 μm. The CTC on the whole gives

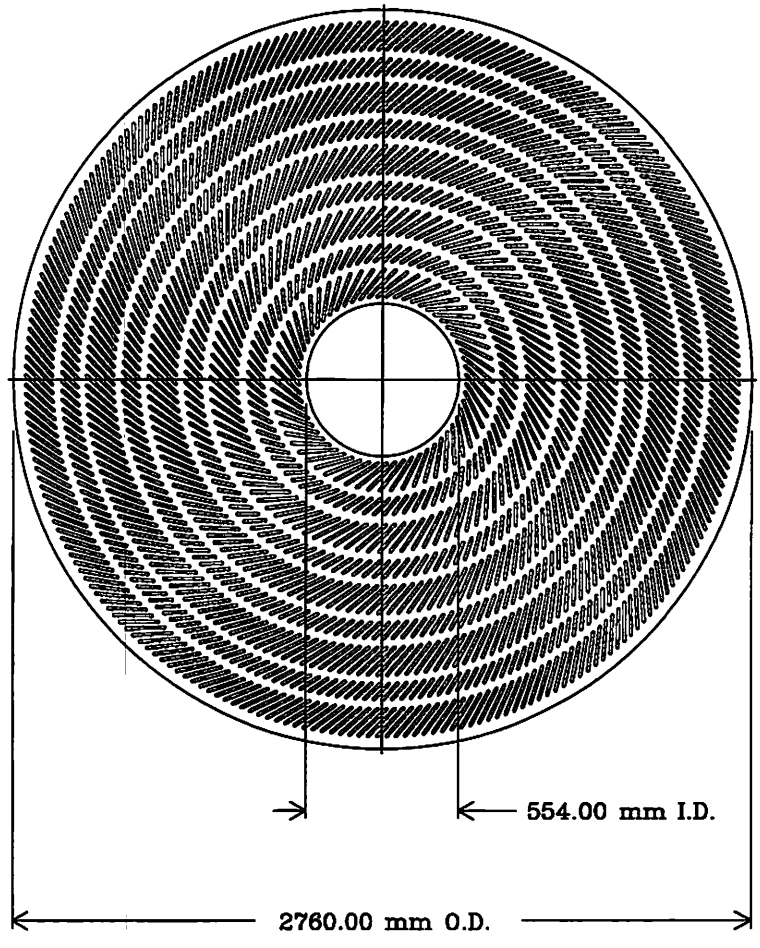

Figure 2.3: Cross sectional view of the CTC end-plate showing both the axial and stereo wire locations.

a momentum resolution of

$$\frac{\Delta P_T}{P_T} \simeq 0.0020 \times P_T \ [\mathrm{GeV}/c] \tag{2.9}$$

for isolated tracks. When the tracks are constrained to the event vertex ("beam constrained") the resolution improves to

$$\frac{\Delta P_T}{P_T} \simeq 0.0008 \times P_T \ [\mathrm{GeV}/c]. \tag{2.10}$$

The absolute momentum scale is calibrated using J/ψ samples and is found to be better than 0.1%.

2.3 Calorimeters

Calorimeters play an important role in high energy physics experiments because it can measure the energy of neutral particles as well as charged particles. It is also possible to identify particles to some extent by measuring their lateral and longitudinal shower profiles.

The CDF calorimeters are installed on central, plug, and forward/backward detectors and cover almost full solid angle. Each calorimeter is divided into two longitudinal components, the electromagnetic in front and the hadronic behind it. They are all sampling calorimeters consisting of passive absorbers to develop particle showers and

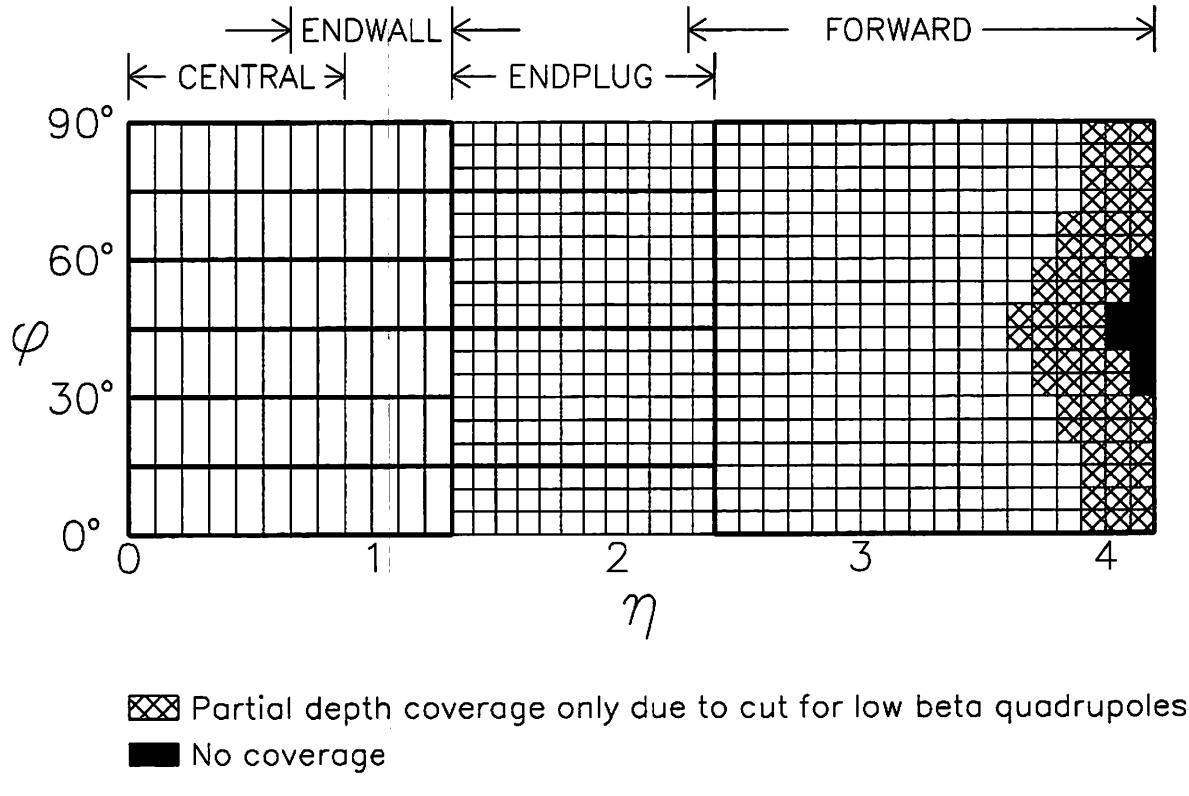

Figure 2.4: Calorimeters (one of eight identical quadrants) mapped in η-ϕ space. The heavy lines indicate module/chamber boundaries of hadron calorimeters. The EM calorimeters have complete ϕ coverage out to $\eta = 4.2$.

Component	Coverage	Thickness
CEM	$0.0 < \|\eta\| < 1.1$	$18X_0$
PEM	$1.1 < \|\eta\| < 2.4$	$18 - 21X_0$
FEM	$2.2 < \|\eta\| < 4.2$	$18X_0$
CHA	$0.0 < \|\eta\| < 0.9$	$4.7\lambda_{abs}$
WHA	$0.7 < \|\eta\| < 1.3$	$4.5\lambda_{abs}$
PHA	$1.3 < \|\eta\| < 2.4$	$5.7\lambda_{abs}$
FHA	$2.3 < \|\eta\| < 4.2$	$7.7\lambda_{abs}$

Table 2.1: Geometrical coverage in η and thickness in X_0 or λ_{abs} of calorimeter components.

active media to detect and measure the energy of secondary particles in the showers. Table 2.1 summarises the geometrical coverage in η and the thickness in radiation length (X_0) or absorption length (λ_{abs}) of each calorimeter component at CDF.

As mentioned before, the CDF calorimeters are arranged in projective towers and are often viewed in LEGO view (Figure 2.4), where energies mapped to the same tower *address* are summed, so that we can examine the energy flow simply by the η-ϕ address, without the complications arising from different detector components. The electromagnetic and hadronic energies are treated separately, so we have two energy quantities per tower address.

2.3.1 CEM

The CDF central electromagnetic calorimeter (CEM) [21] consists of alternating layers of lead sheets (absorber) and plastic SCSN-38 scintillators (sampling medium) with Y7 wavelength shifter; a total of 30 lead layers and 31 scintillator layers correspond

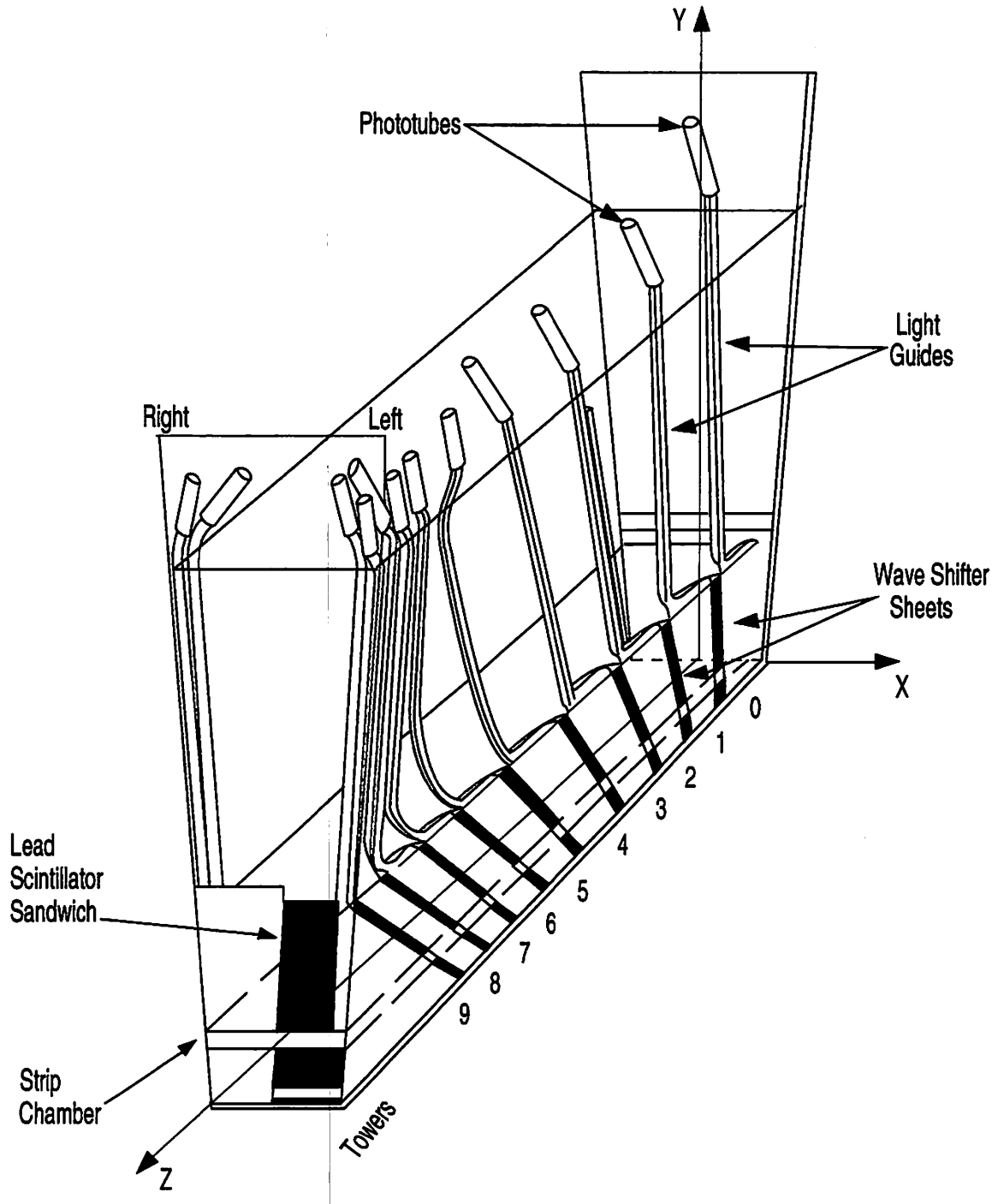

Figure 2.5: Schematic of a wedge module of the CDF central calorimeter, with the CES local coordinate system.

to $18X_0$ of material. The calorimeter is segmented into 24 *wedge* modules in azimuth and 2 along the beam direction. A wedge is further divided into 10 projective *towers* as shown in Figure 2.5. Each tower covers 15° in azimuth and 0.11 in η, which is large enough to entirely contain the electromagnetic shower.

Scintillation light is collected in photomultiplier tubes with a high photoelectron yield of

$$\mathrm{N_{p.e.}} \sim 100/\mathrm{GeV/PMT}. \tag{2.11}$$

Each CEM tower is calibrated using the 50 GeV electron beam. The calibration is maintained using ^{137}Cs radioactive sources for the overall calorimeter response and the LED and Xenon flasher system for the photomultiplier tubes. [26]

The energy resolution of the CEM, measured using the test beam electrons, is

$$\frac{\Delta \mathrm{E}}{\mathrm{E}} = \frac{0.135}{\sqrt{\mathrm{E_T[GeV]}}}. \tag{2.12}$$

The dependence on the polar angle θ is due to the increase in the absorber thickness in lower angle towers.

The response of CEM varies with position within a tower because of the difference in light collection and attenuation in the scintillator plates and is expressed as a response map after detailed studies using test beam electrons [24] and cosmic ray muons [25].

2.3.2 CES

The CES strip chambers [21] are a layer of central proportional chambers with both strip and wire readouts, embedded near shower maximum of the CEM, at nominal depth of $6X_0$. The anode wire measures the r-ϕ view of the shower (the CES local coordinate x) and the cathode strip measures the z position (the CES local coordinate z, which coincides with the CDF global coordinate z). Figure 2.6 shows a schematic view of a CES chamber with the CES local coordinates x and z. The wire signals are read out at 1.45 cm spacing and strip channels have a width of 1.67–2.01 cm. The finer segmentation of the CES chambers enables us to measure more precise profiles of showers than with CEM towers. The position resolutions of ~1.4 mm in x and ~2.2 mm in z are achieved for 50 GeV electrons.

2.3.3 CHA and WHA

Behind the CEM are the central (CHA) and the wall (WHA) hadron calorimeters. [23] They both consist of plastic scintillators and steel absorbers, with the same tower segmentation as the CEM. The resolutions of the CHA and WHA are measured using 10-150 GeV pion test beam to be

$$\frac{\Delta E}{E} = \frac{0.75}{\sqrt{E[GeV]}} \quad \text{(CHA)}, \tag{2.13}$$

$$\frac{\Delta E}{E} = \frac{0.80}{\sqrt{E[GeV]}} \quad \text{(WHA)}. \tag{2.14}$$

2.3.4 Calorimeters in the Plug and Forward Regions

Calorimeters in the plug ($1.1 < |\eta| < 2.4$) and forward/backward ($2.2 < |\eta| < 4.2$) regions are gas proportional chambers with cathode pad readouts sandwiched with lead (for EM) and steel (for HAD) absorbers. A tower size is $0.1 \times 5°$ in $\Delta\eta \times \Delta\phi$. These calorimeters were used in this analysis for $\not\!\!E_T$ measurement.

2.4 Muon Chambers

The central muon detector at CDF consists of central muon chambers (CMU), central muon upgrade chambers (CMP), and central muon extension chambers (CMX+CSX).

2.4.1 CMU

The central muon chambers [28] are located within the central wedges just inside the return yoke, so, like the calorimeters in front of it, the CMU consists of 48 wedge modules. Each CMU wedge module contains 3 chambers, each consisting of 4 layers of drift chambers glued together. Only 12.6° of each central wedge is actually covered by these chambers, leaving a 2.4° gap between adjacent wedges. Figures 2.8 and 2.9 show one of the CMU cell and a tower; Figure 2.10 shows the schematic of the CMU chambers in a central wedge.

The calorimeters provide about $5\lambda_{abs}$ of material from the interaction point to the CMU. Muons with $P_T > 1.5$ GeV can come out of the calorimeter and reach the

CMU.

2.4.2 CMP

The CDF central muon upgrade (CMP) [49] consists of a second set of muon chambers behind an additional 60 cm of steel in the region $55° \leq \theta \leq 125°$. The chambers are of fixed length in z and form a box around the central detector, therefore the actual pseudo-rapidity coverage varies with azitmuth, as shown in Figure 2.7.

The CMP chambers are standard, rectangular, single-wire drift tubes configured in four layers with alternate half-cell staggering. The tubes are made of 0.26 cm thick aluminium extrusions with a single wire in the centre and field shaping cathode strips on the top and bottom, as shown in Figure 2.11. They are typically 640 cm long, with some shorter lengths on the bottom of the detector to avoid obstructions. The single hit tracking resolution of the CMP chambers is approximately 250 μm.

2.4.3 CMX and CSX

The central extension consists of conical sections of drift tubes (CMX) and scintillation counters (CSX) located at each end of the central detector, extending the central muon coverage in $|\eta|$ from 0.65 to 1.0.

The CMX drift tubes are arrayed as a logical extension of the central system. There are four logical layers of twelve tubes for each 15° ϕ sector, and successive layers are half-cell offset to eliminate left-right ambiguities, as shown in Figure 2.12.

Each logical layer consists of two physical layers of drift tubes which partially overlap each other, creating a stereo angle of 3.6 mrad between adjacent cells, which not only provides redundancy but also permits the measurement of the polar angle of the track with moderate accuracy. The drift tubes for the CMX conical sections are identical to the CMP drift tubes except that they are only 180 cm long.

A layer of four CSX scintillation counters is installed on both the inside and the outside surfaces of each 15° CMX sector. The counters are slightly trapezoidal in shape with the same length (180 cm) as the drift tubes. The counters on the inside and outside layers are half-cell staggered with respect to each other thereby doubling the effective granularity of the system.

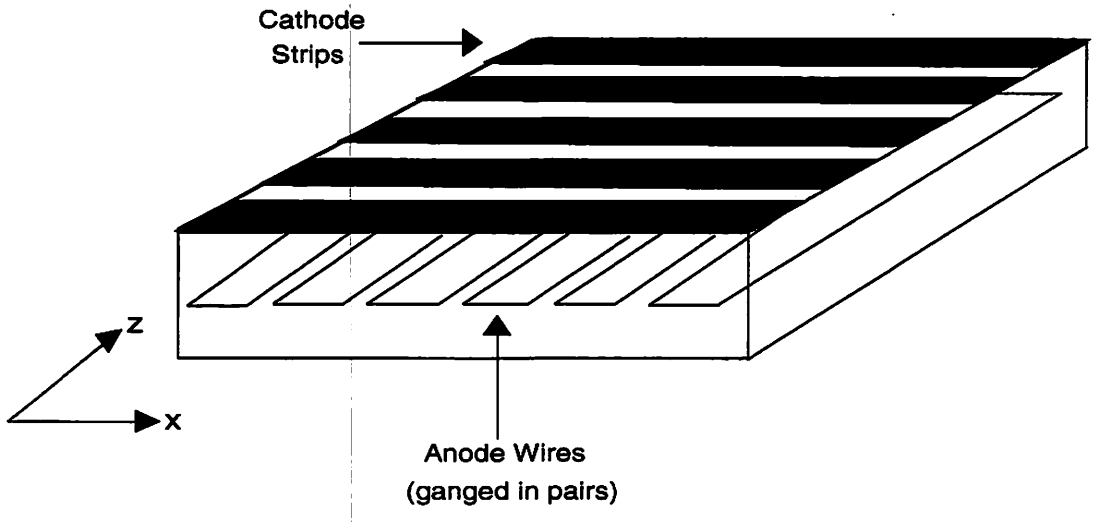

Figure 2.6: Schematic of CES wires and strips. Also shown is the CES local coordinates x and z.

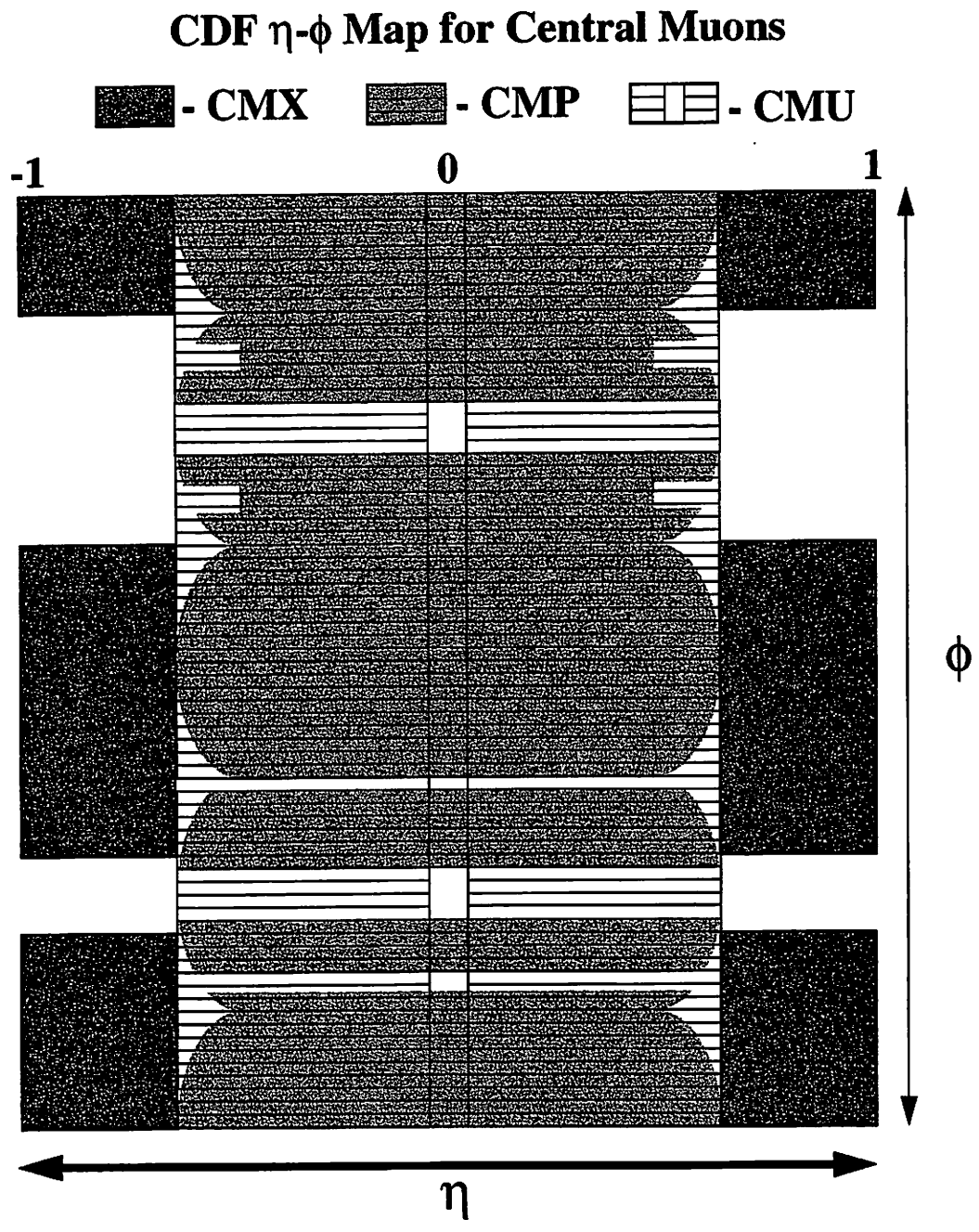

Figure 2.7: Map of central muon detector coverage in η-ϕ.

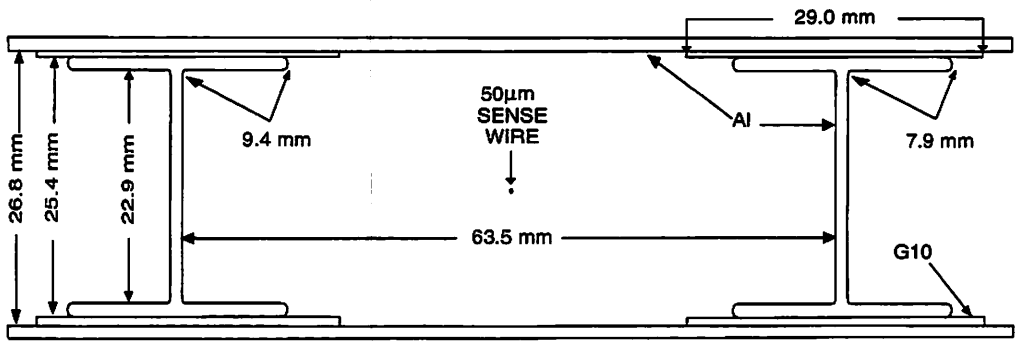

Figure 2.8: A CMU cell.

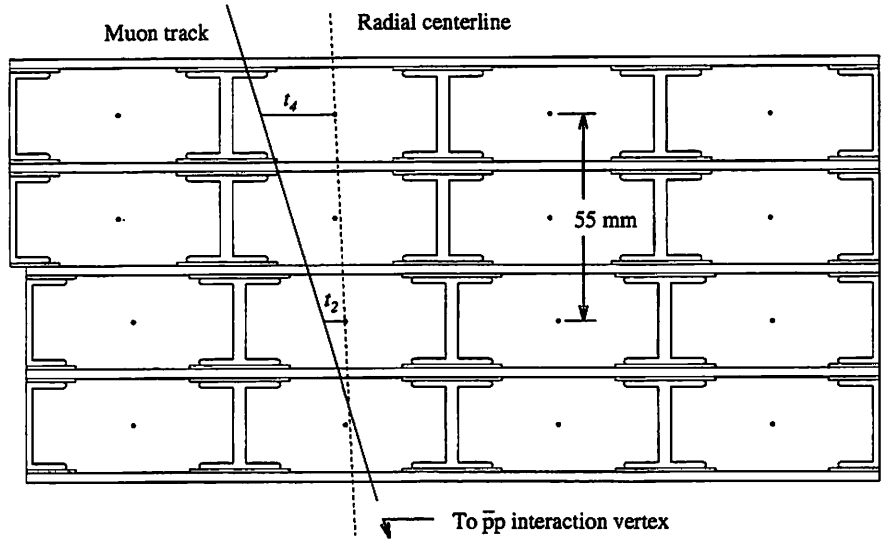

Figure 2.9: The arrangement of the four planes of CMU chambers in a view along the beam direction. The drift times t_2 and t_4 are used at the trigger level to determine a muon momentum cutoff.

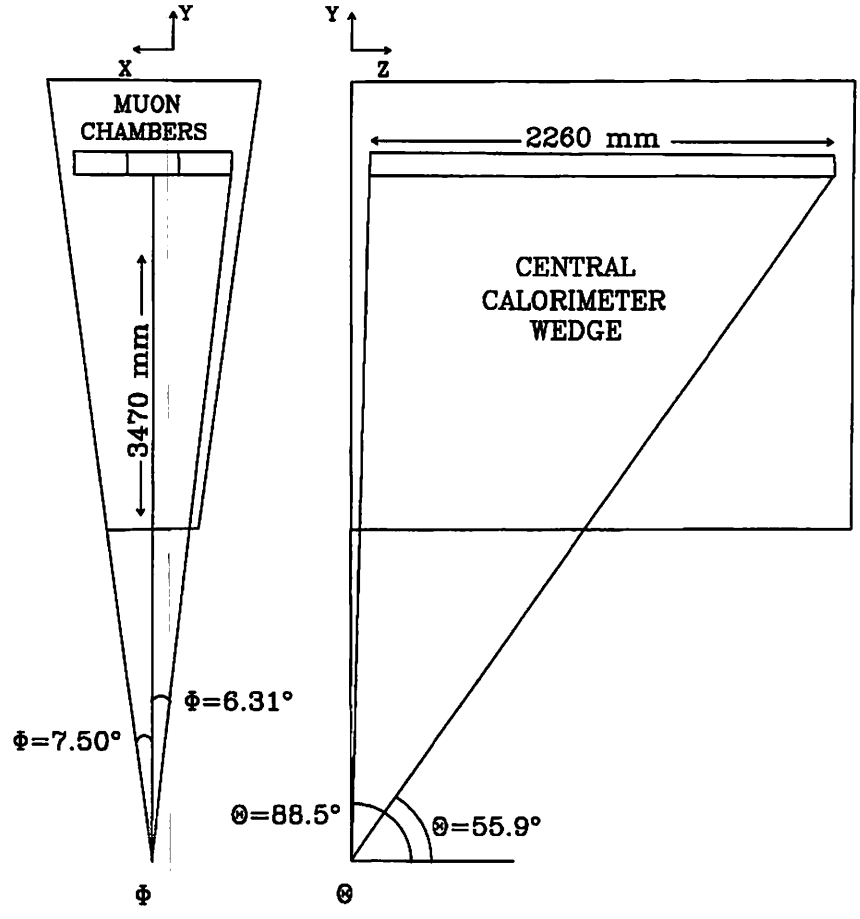

Figure 2.10: The layout of the CMU chambers in one of the central wedges.

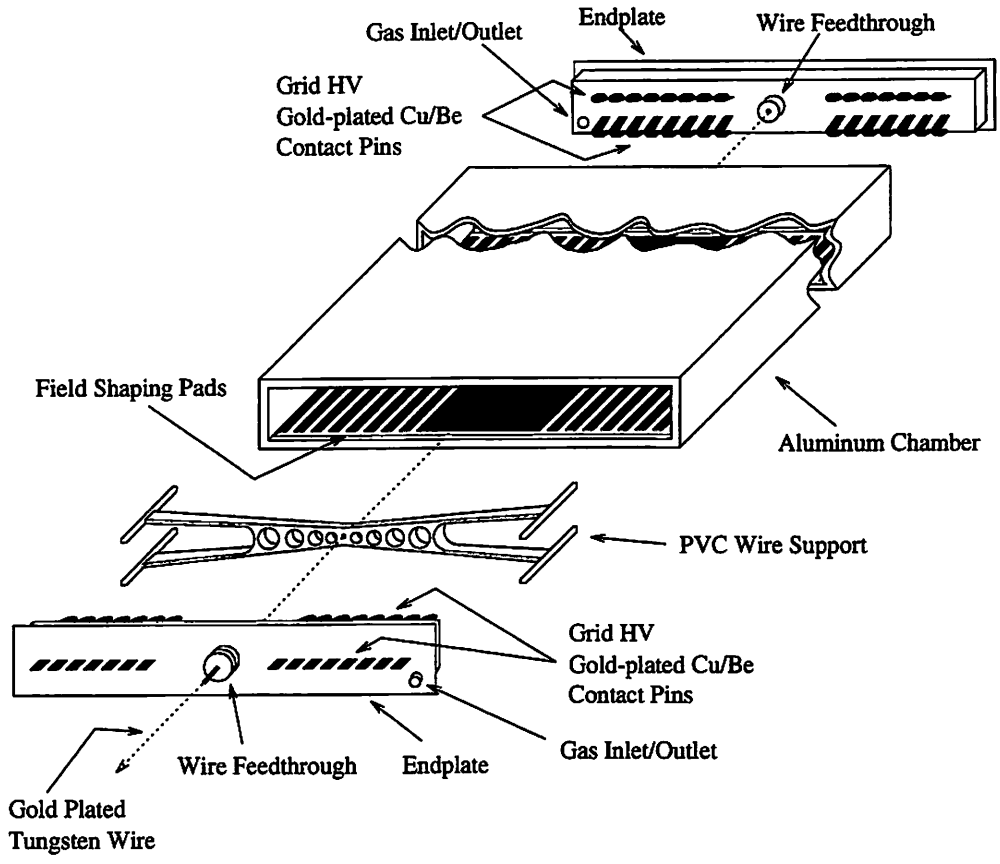

Figure 2.11: Schematic view of a CMP tube. The CMX uses identical but shorter tubes without wire supports.

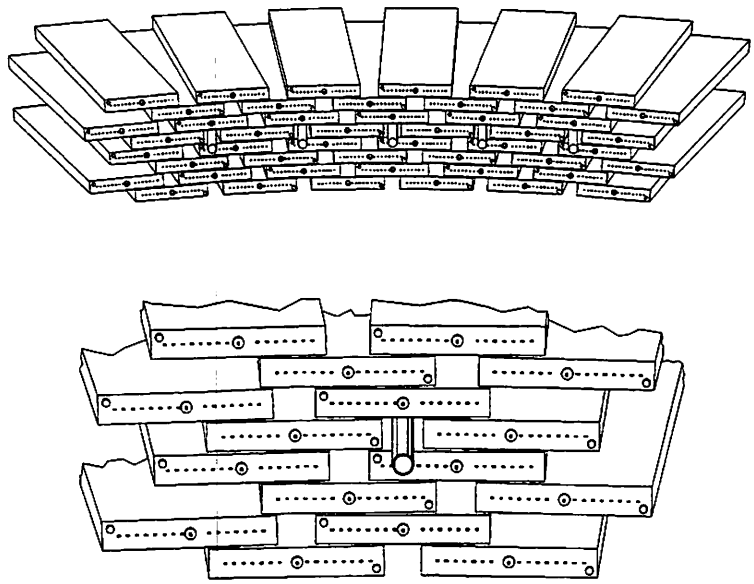

Figure 2.12: Schematic view of a 15° CMX module.

Chapter 3

Wγ Event Selection

The Wγ candidate events are extracted from the high P_T lepton data samples that passed the CDF three-level high P_T electron and muon triggers. A well isolated high P_T lepton (electron or muon) is identified by requiring a series of quality selection criteria. The neutrino from the W decay is not detected so we measure everything else and deduce its momentum. A Wγ candidate event additionally requires a photon associated with the W. We assume both the neutrino and the photon originate from the vertex determined by the charged lepton. The event signature of the Wγ events is therefore a high P_T isolated electron or muon, an isolated EM cluster with no associated track, and a large missing transverse energy ($\not\!\!E_T$). This chapter describes the selection criteria of the Wγ candidate events used in this analysis.

3.1 Electron Identification

Electrons in the central region are identified by a large energy deposit in the CEM electromagnetic calorimeter with a small leakage in the CHA hadron calorimeter and an associated high P_T track in the CTC tracking chamber.

The first indication of a high P_T electron in the event is the presence of a large energy deposit in a central EM calorimeter tower. A level-1 trigger for a high P_T electron typically requires an energy deposit E_T of more than 8 GeV in a tower. At level-2 a track of transverse momentum $P_T > 7.5$ GeV is associated with the calorimeter cluster. The level-3 high P_T electron trigger increases these thresholds to 18 GeV in the calorimeter and 13 GeV in the central tracking chamber.

Offline analysis begins with correcting the raw energies of the electron-like objects. Difference in response within a tower and for tower-to-tower variations are corrected. The global energy scale is also corrected to give good E/P ratio for real electrons as a whole. Tracks are constrained to the beam to give better momentum resolution.

A set of quality cuts are then applied to the electron candidates.

- **Longitudinal shower shape: HAD/EM**

  The longitudinal shower profile (Figure 3.1) of an electron is different from that of a hadron; an electron showers faster with smaller amount of material and most of its energy is contained in the CEM while a hadron develops its shower more slowly, depositing large energy in the CHA as well as in the CEM.

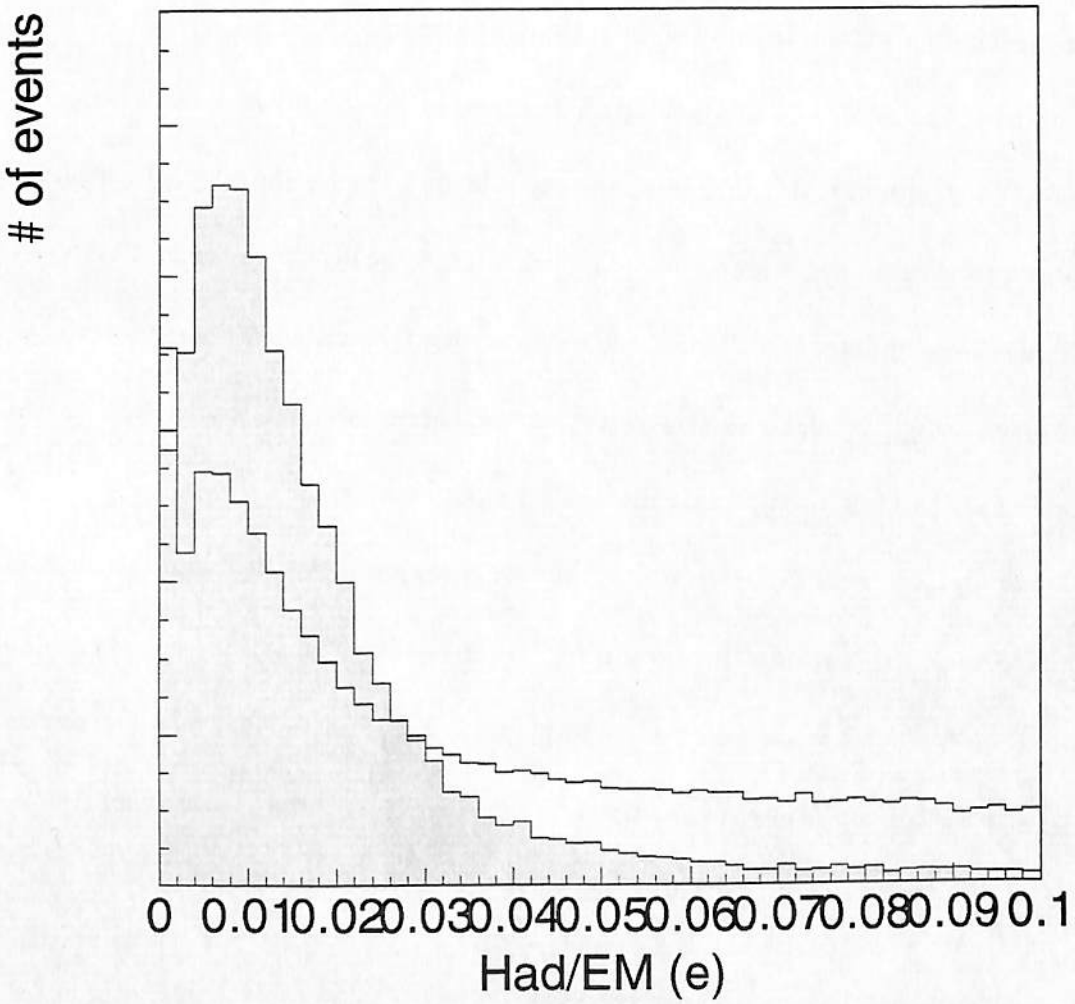

Figure 3.1: Hadronic energy distributions for W electrons (shaded) and backgrounds (clear). Here "electrons" are the candidates that pass all the selection cuts described in this section except HAD/EM cut, and "backgrounds" consist of those candidates that fail at least another selection cut. Distributions are normalised to the same area. A similar convention applies to the following histograms in this section.

A cluster is accepted as electromagnetic if the ratio E_{HAD}/E_{EM} of the energy deposit in the CHA to that in the CEM is below a certain value, for which we use

$$\frac{E_{HAD}}{E_{EM}} < 0.055 + 0.00045 \times E_{cl}[\text{GeV}], \tag{3.1}$$

where E_{cl} is the total energy deposit of the cluster in GeV.

- **Lateral shower shape: L_{SHR}**

The variable L_{SHR} describes a lateral sharing of the EM shower energy in the CEM towers in an energy cluster (Figure 3.2) and is defined by

$$L_{SHR} = 0.14 \sum_i \frac{E_i^{meas} - E_i^{pred}}{\sqrt{(\Delta E_{cl})^2 + (\Delta E_i^{pred})^2}}, \tag{3.2}$$

where the sum is over towers adjacent to the seed tower in η[1]; E_i^{meas} is the measured energy on tower i; E_i^{pred} is the energy predicted for tower i using the impact point in z on the strip chamber, the event vertex, and the shower profile obtained from the test beam measurement, with error ΔE_i^{pred}; and ΔE_{cl} is the uncertainty in the electromagnetic cluster energy given by

$$\Delta E_{cl} = 0.14\sqrt{E_{cl}}. \tag{3.3}$$

[1]The boundaries between wedges prevent EM showers from spreading over multiple towers in ϕ, so EM clusters always consist of (two or three) towers in the same wedge.

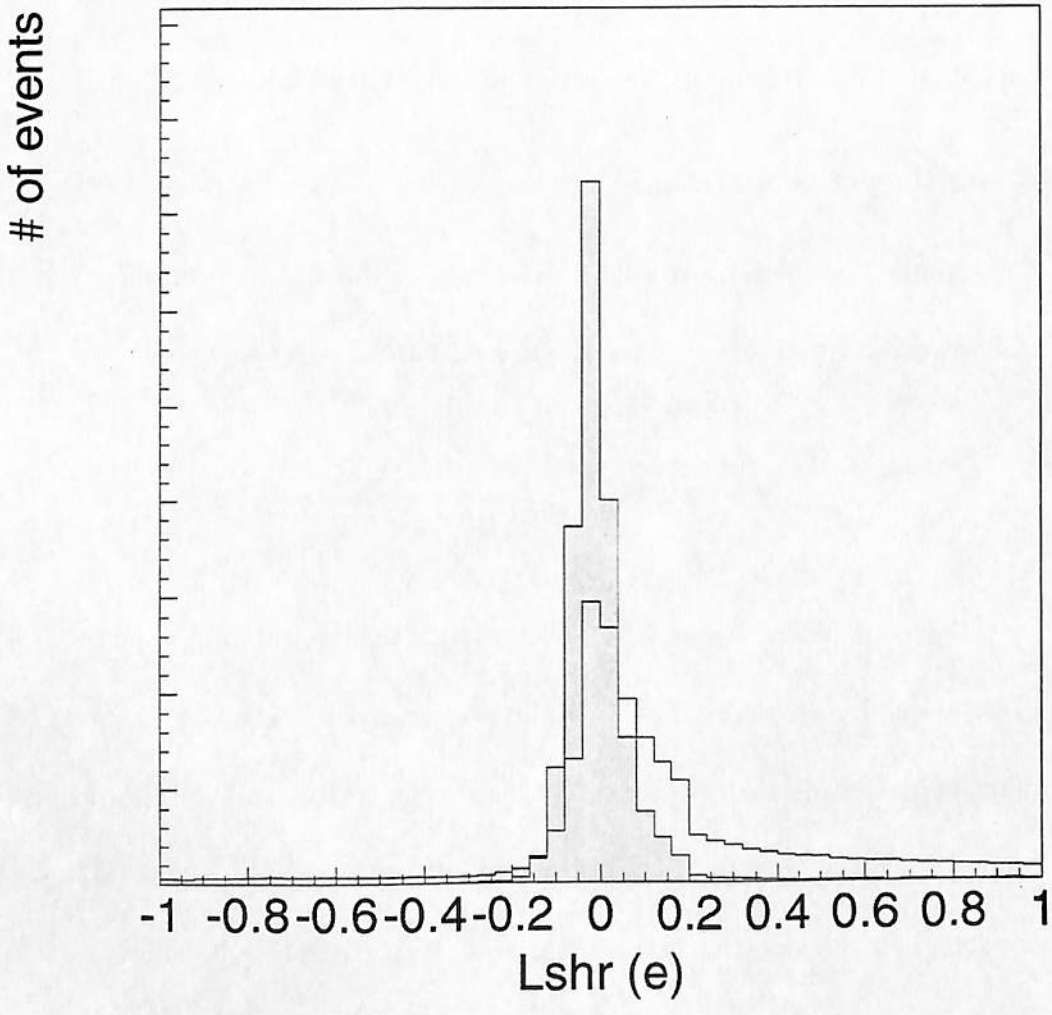

Figure 3.2: Lateral profile distributions for W electrons (shaded) and backgrounds (clear). Trigger electrons already pass some loose electron cuts by the time they get written to tape. For the L_{SHR} variable, they are required to satisfy $L_{SHR} < 0.2$.

We require

$$L_{SHR} < 0.2. \tag{3.4}$$

- **Lateral shower shape: CES χ^2**

While L_{SHR} is useful in rejecting showers extending over multiple CEM towers, a single tower itself is still large enough for a few collimated particles such as two decay photons from π^0s. The CES provides information about the shape of shower within a CEM tower. The minimum distance d beween two photons from a π^0decay at the depth of CES (184.15 cm from the beam line) is expressed as

$$d \approx \frac{50}{P_T[\mathrm{GeV}/c]}[\mathrm{cm}], \tag{3.5}$$

where P_T is the transverse momentum of the π^0 in GeV/c, so the distance d is about 7 cm (2 cm) for 7 (25) GeV/c π^0s. For the strip view[2], we minimise the following function to obtain the z-coordinate of the shower center, Z_{CES}, and the strip cluster energy, E_S:

$$\chi^2(z,E) = \sum_{i=1}^{11} \frac{(E_i^{meas} - E\, q_i^{pred}(z))^2}{\sigma_i^2(z)}, \tag{3.6}$$

where E_i^{meas} represents the measured energy for channel i, $q_i^{pred}(z)$ is the predicted energy distribution (normalised to 1) centred at given z; and $\sigma_i^2(z)$ is the

[2]We also have analogous expressions for wire view, which are used for identifying photons, as discussed in Section 3.4.

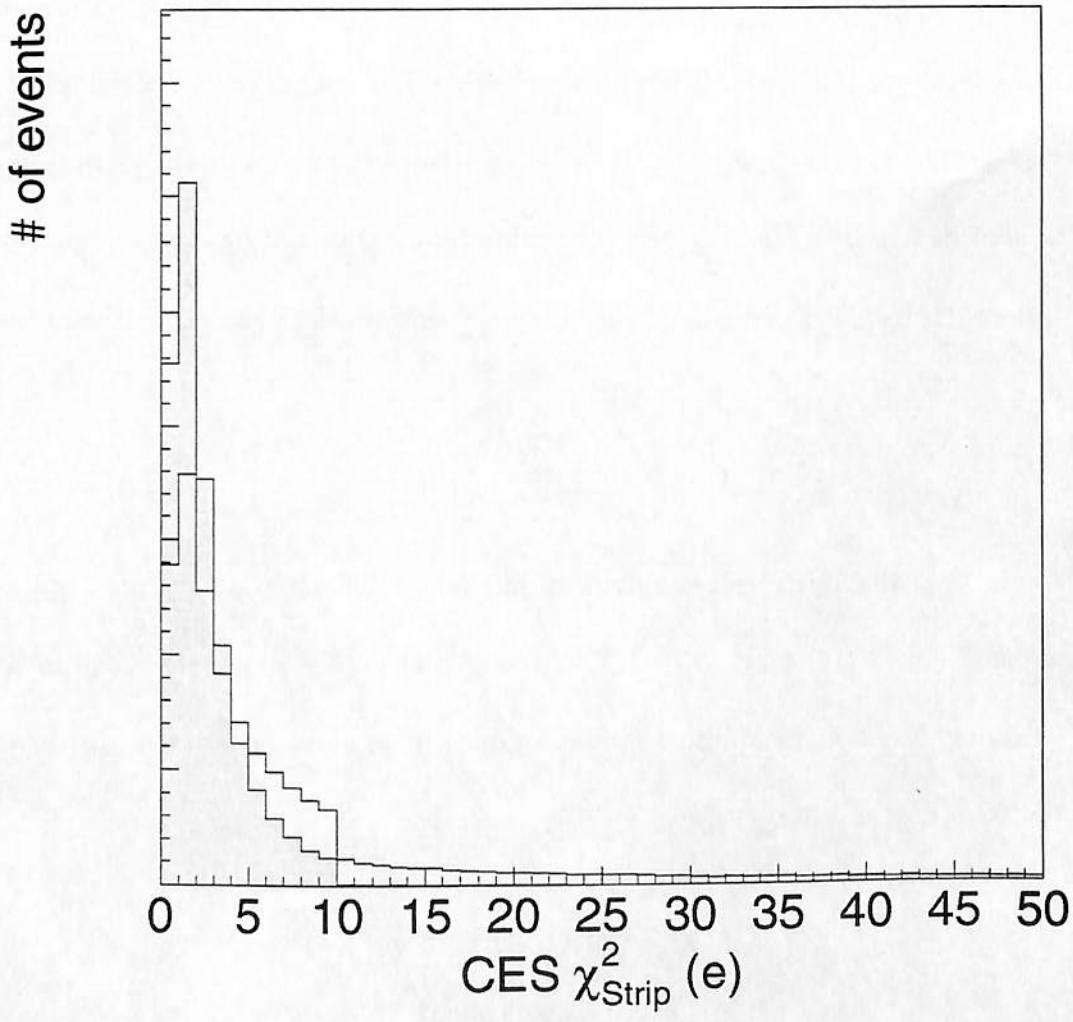

Figure 3.3: CES χ^2 distributions in strip view for W electrons (shaded) and backgrounds (clear).

fluctuation in a single channel response given by

$$\sigma_i^2(z) = 0.026^2 + 0.096^2\, q_i^{pred}(z), \tag{3.7}$$

which is derived from 10 GeV/c test beam electron data. To test a single electron/photon hypothesis, we introduce the variable:

$$\chi^2_{Strip} = \frac{1}{4}\left(\frac{\mathrm{E}_{cl}}{10}\right)^{0.747} \sum_{i=1}^{11} \frac{(q_i^{meas} - q_i^{pred}(Z_{CES}))^2}{\sigma_i^2(Z_{CES})}, \tag{3.8}$$

where q_i^{meas} ($i = 1 \ldots 11$) are the measured strip profiles normalized to 1. We use E_{cl} rather than E_S, since the CEM has better resolution than the CES. We require (Figure 3.3)

$$\chi^2_{Strip} < 10. \tag{3.9}$$

- **Fiducial region**

  In order to measure the electron energy properly, we require the electron to be well within the fiducial region defined in the CES local coordinates below:

$$|x| < 21.0 \text{ cm}, \tag{3.10}$$

$$9.0 < |z| < 230.0 \text{ cm}. \tag{3.11}$$

- **Number of associated charged tracks**

The number of tracks reconstructed in 3 dimension that point to the EM cluster is required to be one:

$$N_{3D} = 1. \tag{3.12}$$

We reject events with multiple tracks pointing to the same cluster, where accuracy of the energy measurement is poor. This requirement also imposes an implicit isolation to the electron.

- **Position matching**

Requiring a geometrical matching between calorimeter cluster and track is useful in rejecting backgrounds arising from overlap of photons and a charged hadron. The track found in the CTC is extrapolated to the CES and compared with the position of the cluster determined by the CES strip information in both views. (Figure 3.4) We require

$$|\Delta x| < 1.5 \text{ cm}, \tag{3.13}$$

$$|\Delta z| < 3.0 \text{ cm}. \tag{3.14}$$

- **Energy and momentum comparison**

To further suppress overlap backgrounds we compare the momentum measured from the track with the energy in the calorimeter. (Figure 3.5) If they are from

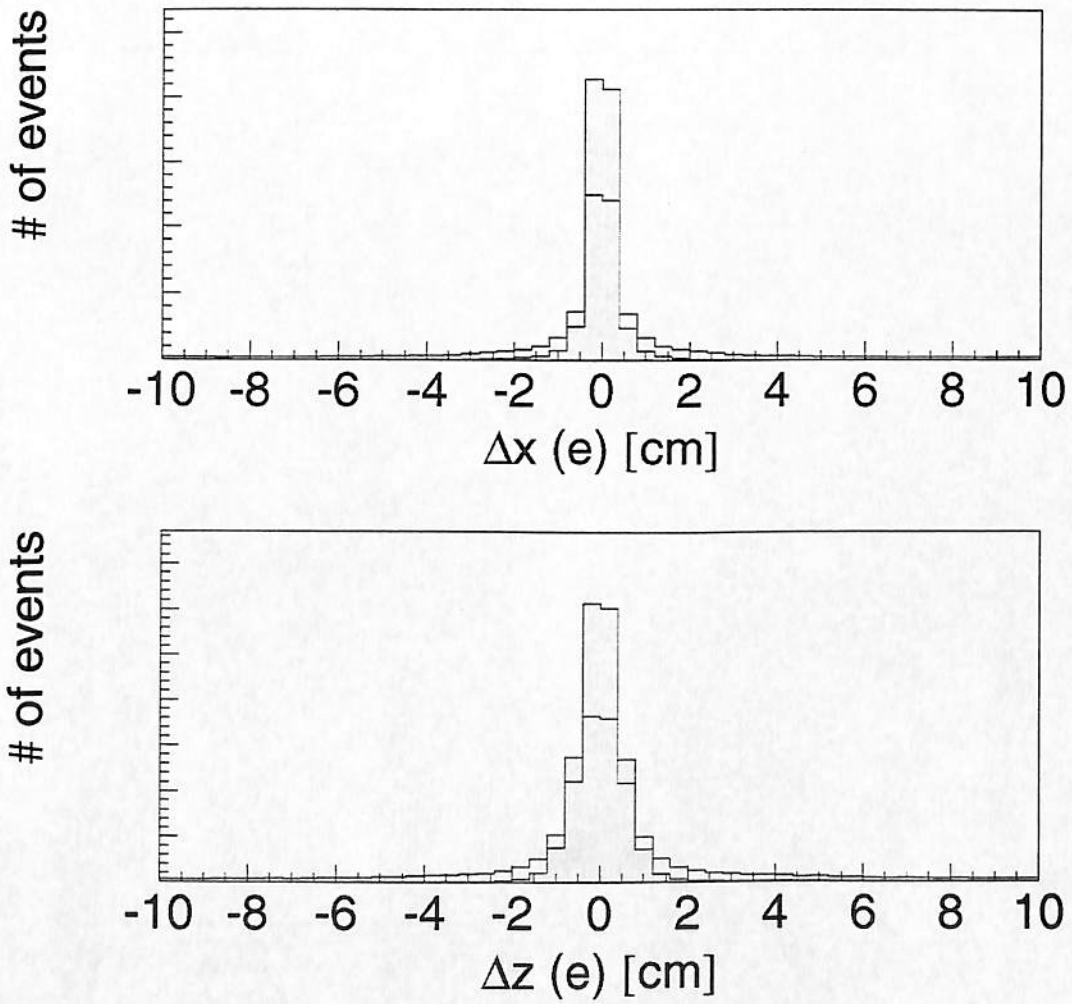

Figure 3.4: Distributions of difference in wire and strip views between CES strip chamber cluster and CTC track positions for W electrons (shaded) and backgrounds (clear).

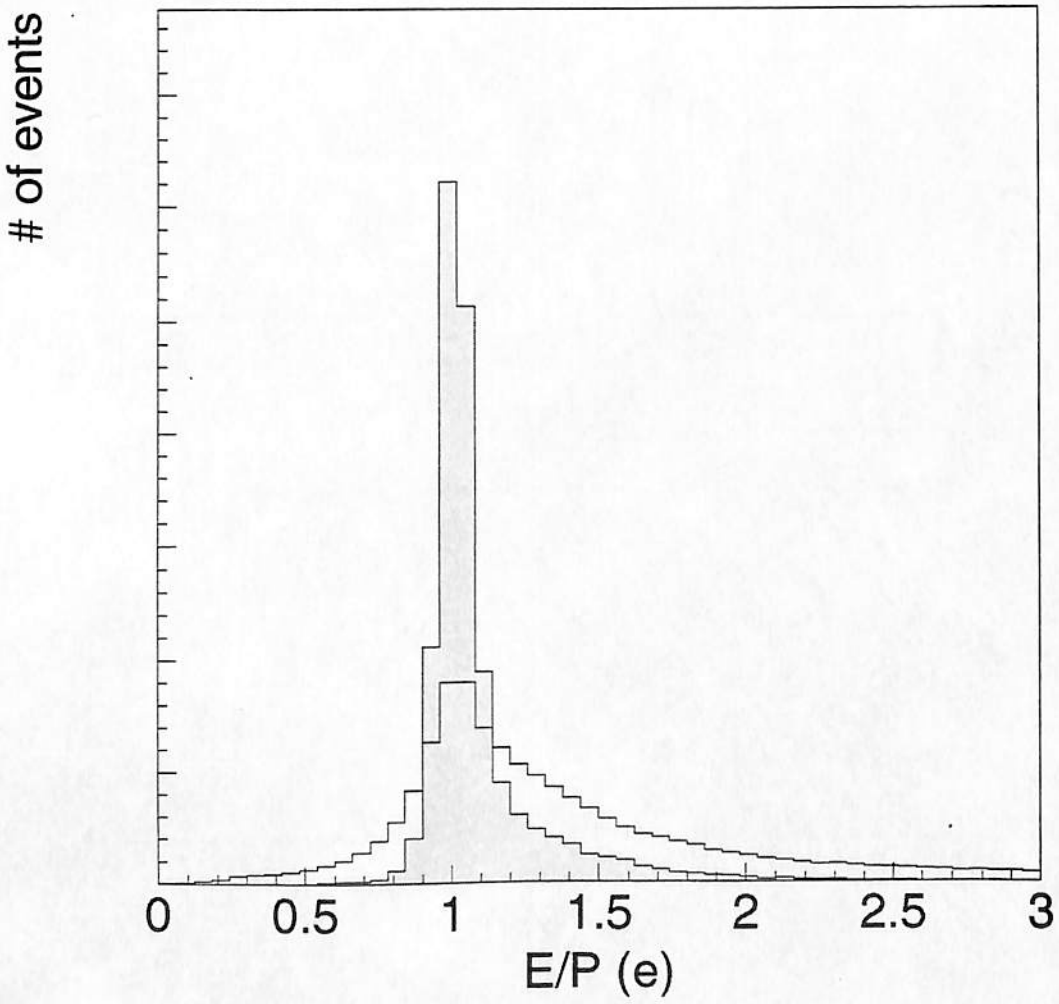

Figure 3.5: E/P distributions for W electrons (shaded) and backgrounds (clear).

the same particle, the ratio is close to unity. We require

$$0.5 < \frac{\mathrm{E}}{\mathrm{P}} < 2.0. \tag{3.15}$$

Removing Electrons from Photon Conversions

Another important quality cut for electrons is the removal of electrons from photon conversions. Since they are real electrons, tightening the quality cut thresholds will do more harm than good; We remove them by identifying the conversion partner. In the presence of axial magnetic field, the pair separates in r-ϕ view but remains collinear in r-z view, so we find the conversion partners that satisfy:

$$Q_e \times Q_{trk} = -1, \tag{3.16}$$

$$|S| < 0.26 \text{ cm}, \tag{3.17}$$

$$|\Delta \cot\theta| < 0.046, \tag{3.18}$$

$$|\Delta z| < 3.0 \text{ cm}, \tag{3.19}$$

where Q_e and Q_{trk} are the charges of the electron candidate and the partner; and $\Delta \cot\theta$ and S are the separation of the two tracks in r-z and r-ϕ planes at conversion point. In case we find more than one track that satisfy the above criteria, we choose the one that is closest to the electron candidate. To avoid accidentals, we also check to see if the candidate is chosen as the partner of that track and remove only those

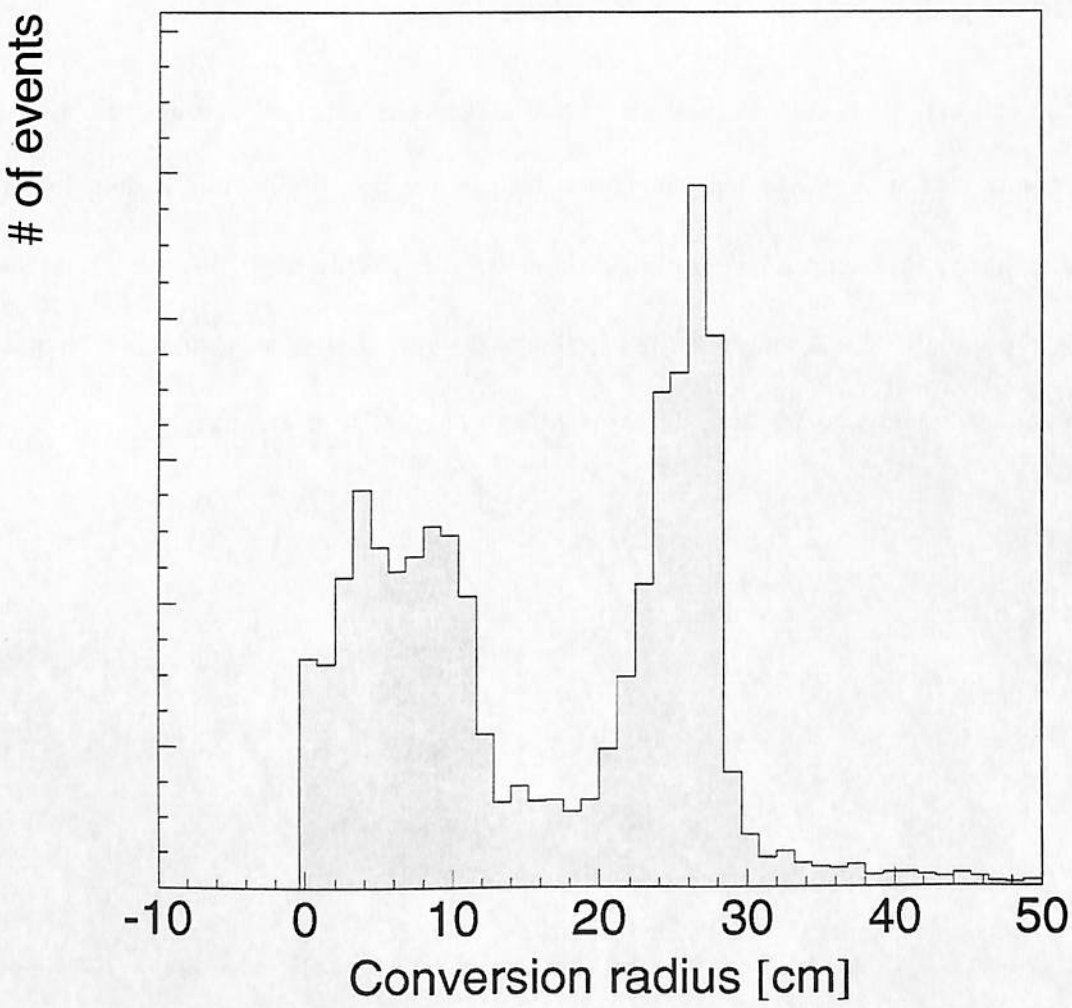

Figure 3.6: The radial distributions of photon conversion points.

candidates which can be identified as conversion pairs either way. This takes care of cases where a pair of tracks from a real photon conversion happen to be found near a real electron; even if one of the pair tracks satisfy the cuts above, it is unlikely that the electron would be chosen as the partner of that track. Figure 3.6 shows the radial distribution of the photon conversions so obtained, revealing the detector structure.

3.2 Muon Identification

Muon identification takes advantage of the properties of the muon that it leaves a charged track stub in the CTC and CMU/CMP/CMX muon chambers and deposits only a small portion of its energy corresponding to minimum ionisation in the calorimeters, which makes them highly penetrating as compared to other particles. Unlike the electron identification described above, the muon identification is therefore somewhat simpler; most of the particles are absorbed in the calorimeter and do not reach the muon chambers behind it.

Muon candidates are required to pass the following quality cuts:

- **Minimum ionisation cuts**

  The energy deposits in the calorimeters interpolated from the CTC beam-constrained track and the hits in the muon chambers are required to be consis-

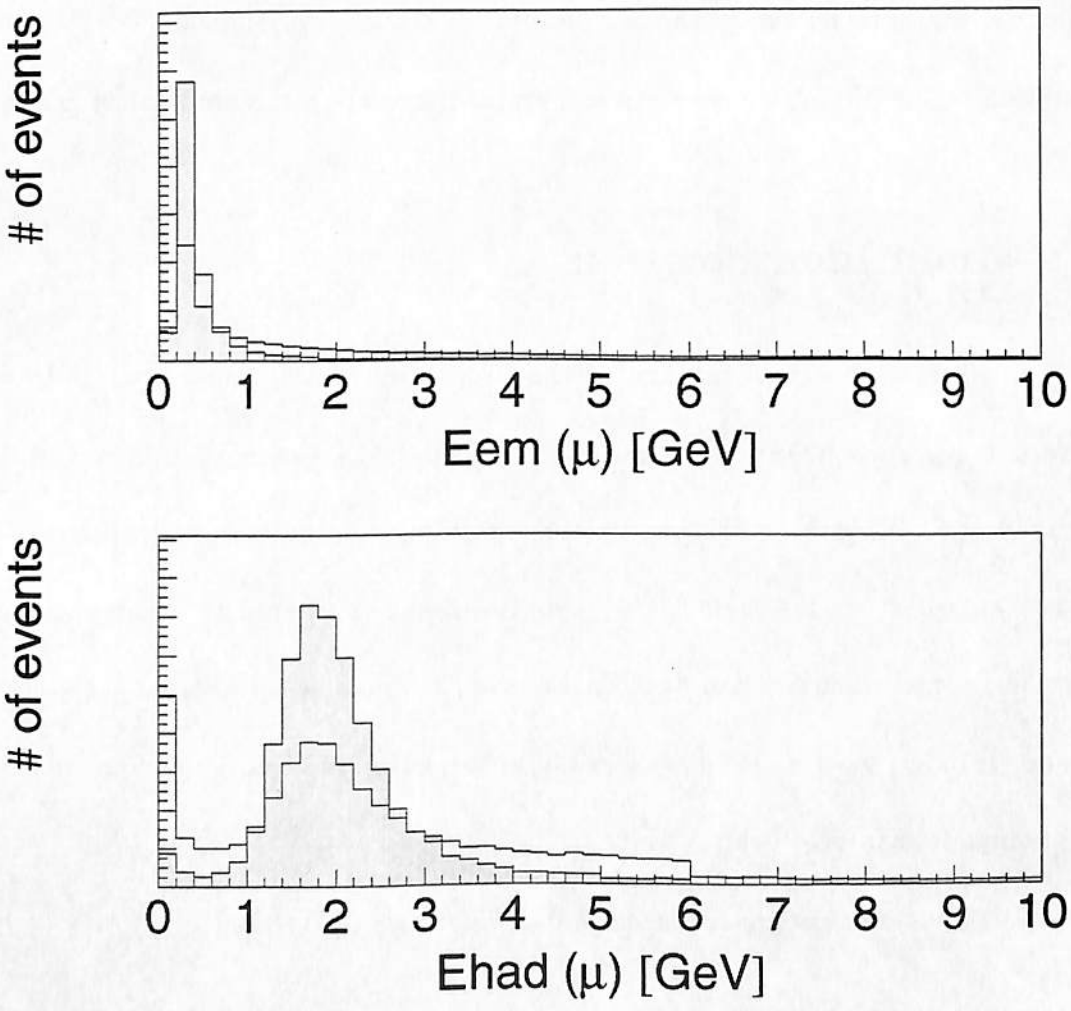

Figure 3.7: Distributions of energy deposits in the calorimeters for W muons (shaded) and backgrounds (clear). Again, "muons" here are the candidates that pass all the selection cuts described in this section except MIP cut, and "backgrounds" consist of those candidates that fail at least another selection cut. Distributions are normalised to the same area. A similar convention applies to the following histograms in this section.

tent with those of a minimum ionising particle (Figure 3.7):

$$E_{EM} < 2.0 \text{ GeV}, \tag{3.20}$$

$$E_{HAD} < 6.0 \text{ GeV}. \tag{3.21}$$

- **Position matching**

  As in the electron identification, we compare the hit position in the muon chambers with a track in the CTC extrapolated to each muon chamber. We require (Figure 3.8)

$$|\Delta X_{CMU}| < 3.0 \text{ cm}, \tag{3.22}$$

$$|\Delta X_{CMP}| < 5.0 \text{ cm}, \tag{3.23}$$

$$|\Delta X_{CMX}| < 5.0 \text{ cm}. \tag{3.24}$$

The above cut thresholds take into account the expected deflections due to multiple Coulomb scattering in the calorimeter and steel.

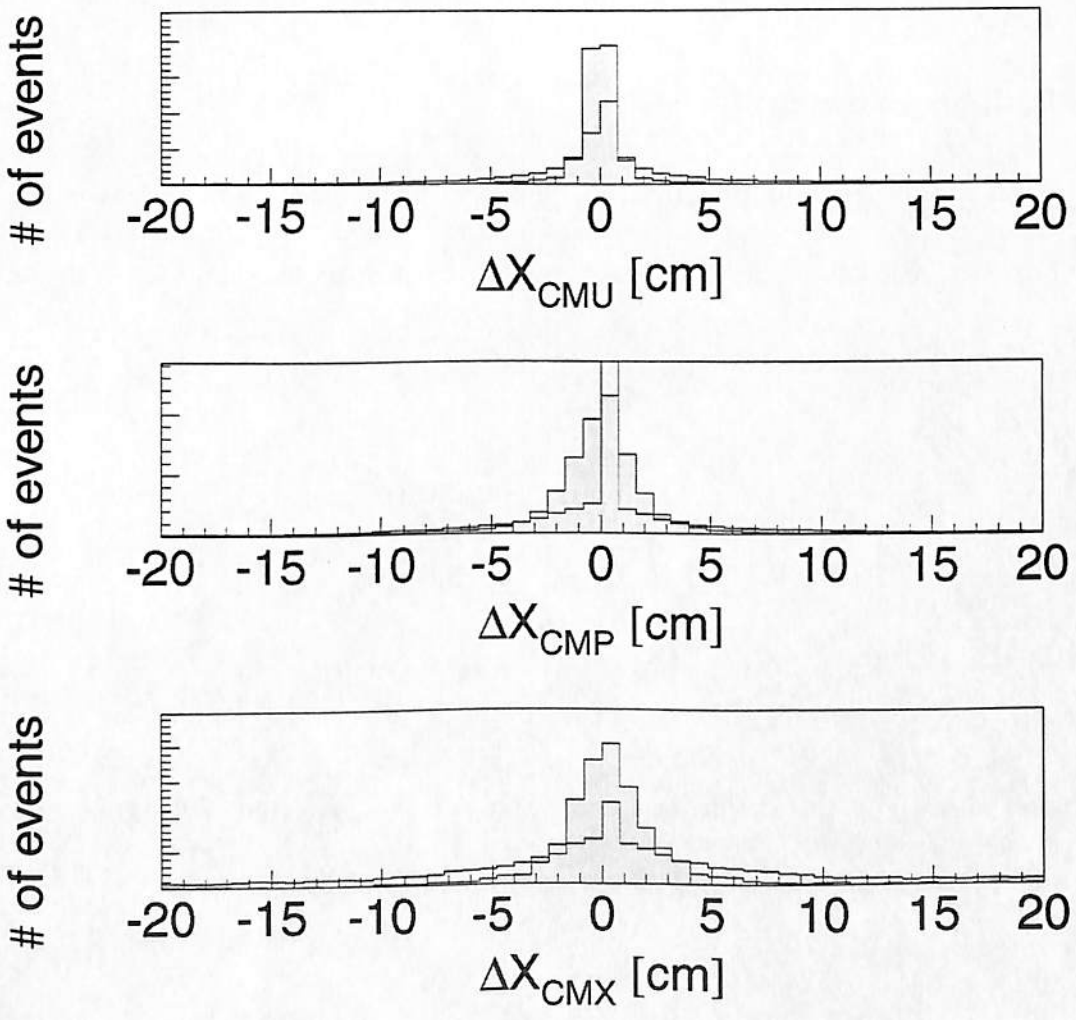

Figure 3.8: Distributions of differences between muon chamber hits and CTC track position for W muons (shaded) and backgrounds (clear).

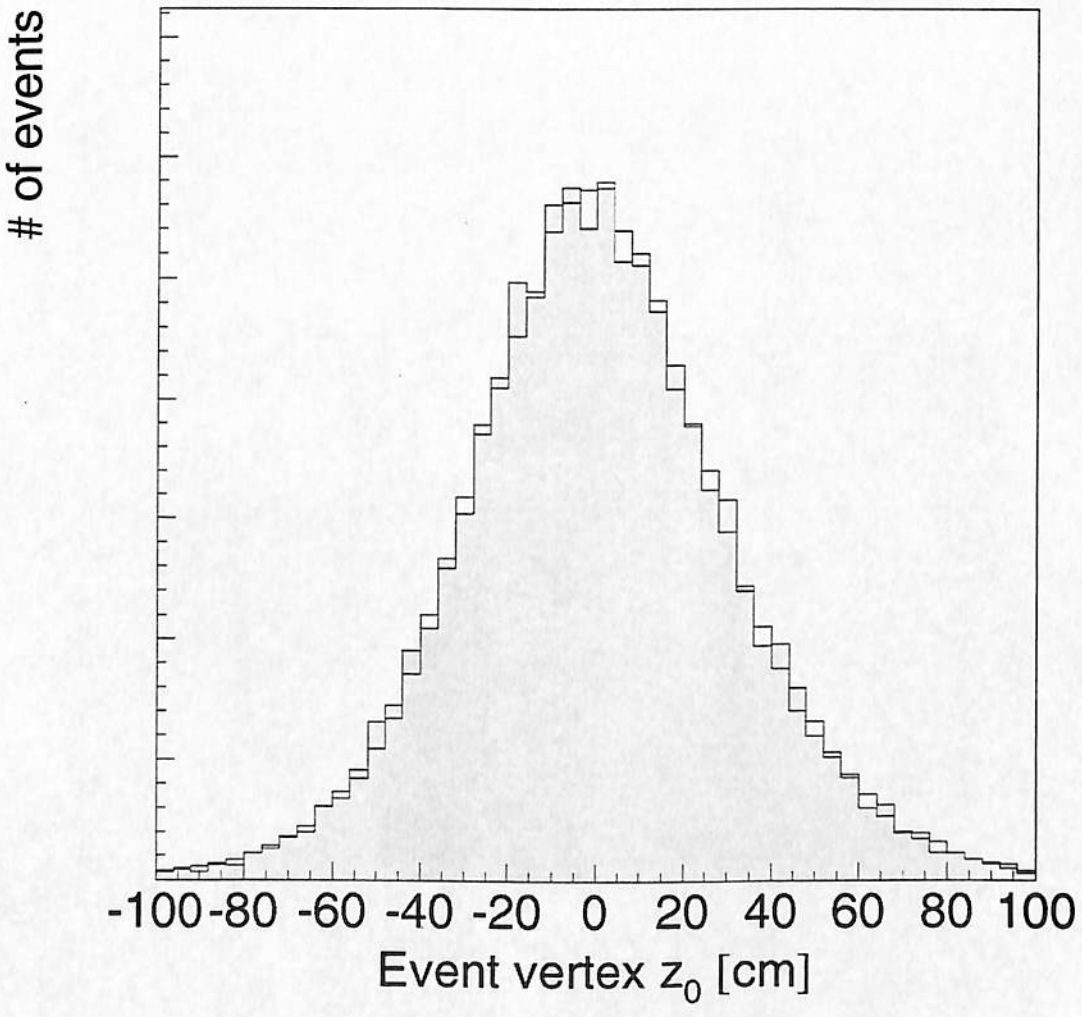

Figure 3.9: Distributions of event z vertex positions for W leptons (shaded) and backgrounds (clear).

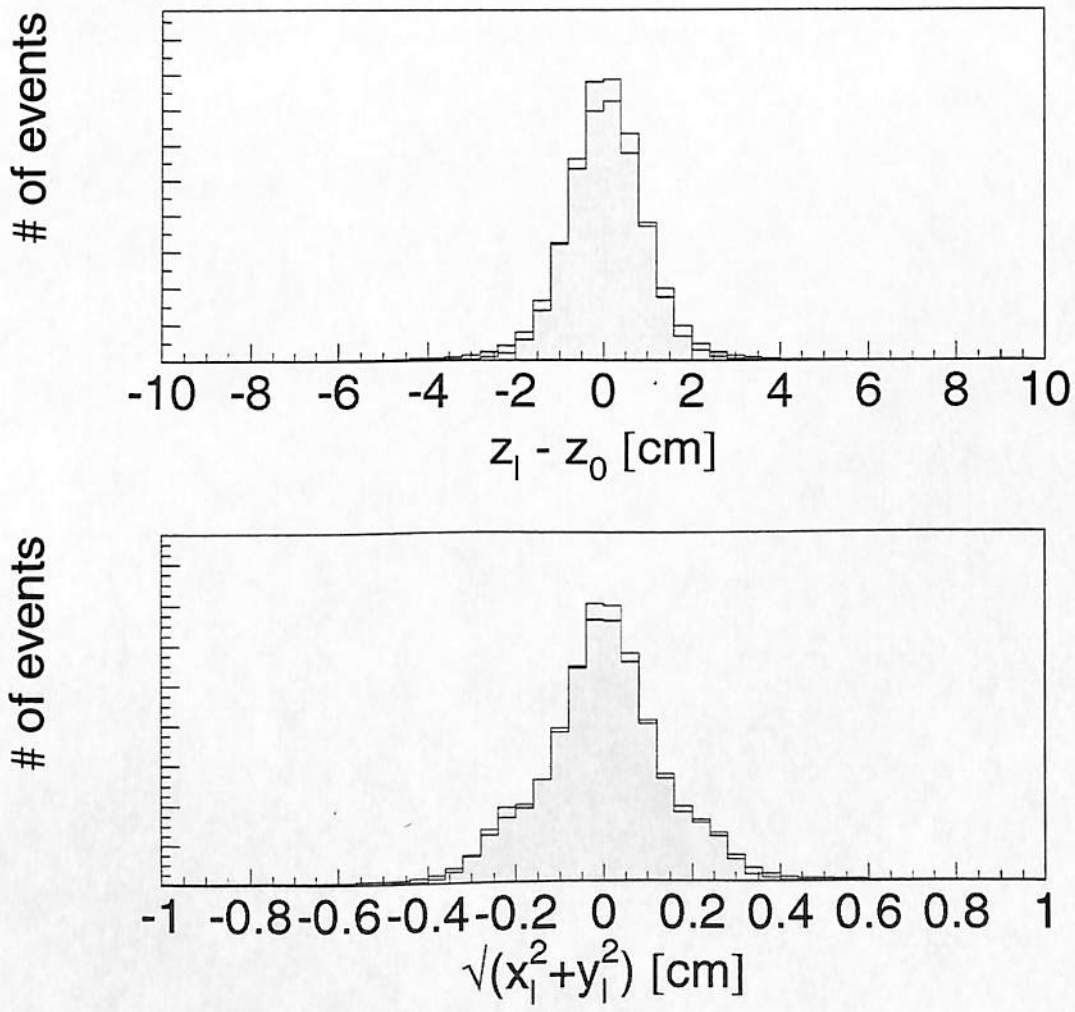

Figure 3.10: Distributions of differences between the the event vertices z_0 and impact points in z (top) and $x-y$ plane (bottom) for W leptons (shaded) and backgrounds (clear).

3.3 Event Vertex

The event must have a well defined vertex. We require electrons and muons that satisfy the quality cuts defined above to come from a primary vertex:

$$|z_\ell - z_0| < 5.0\,\text{cm}, \tag{3.25}$$

$$\sqrt{x_\ell^2 + y_\ell^2} < 0.5\,\text{cm}, \tag{3.26}$$

$$|z_0| < 60.0\,\text{cm}. \tag{3.27}$$

where z_0 is the z-coordinates of the primary vertex and (x_ℓ, y_ℓ, z_ℓ) is the coordinates of the lepton's impact point. Figures 3.9 and 3.10 show the distributions of z vertices and impact points with respect to the closest vertices.

3.4 Photon Identification

A photon looks like an electron without an associated track, so many of the quality cuts are identical[3] though we have slightly different thresholds mainly because we are interested in photons of lower energy. Position matching and E/P cuts are not applicable because we do not have a track. The four-momentum of a photon is recalculated using the event vertex and the CES cluster.

- **Longitudinal shower shape: HAD/EM**

[3]In particular, we apply the identical CEM energy corrections to photons as well as electrons

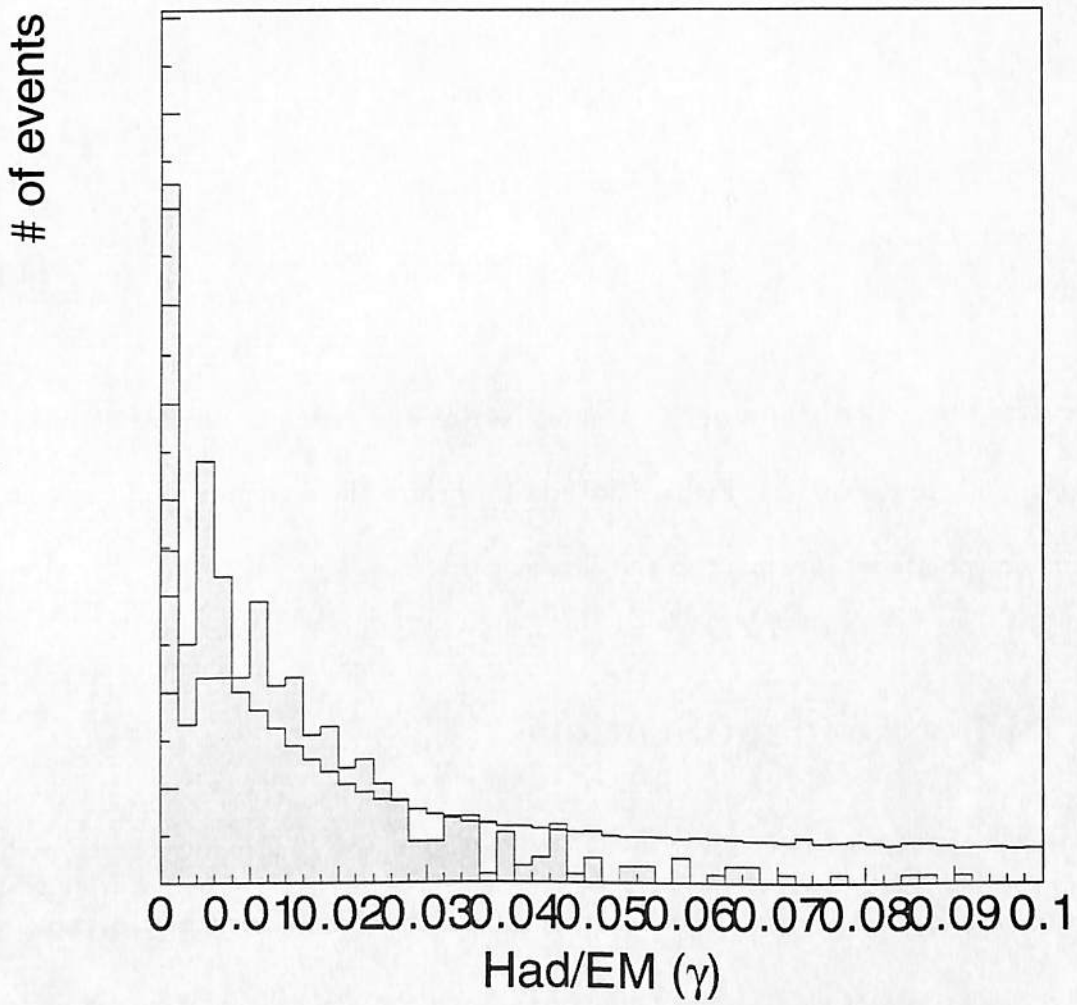

Figure 3.11: Hadronic energy distributions for photon candidates (shaded) and backgrounds (clear). Here "photons" are the candidates that pass all the selection cuts described in this section except HAD/EM cut, and "backgrounds" consist of those candidates that fail at least another selection cut. Distributions are normalised to the same area. A similar convention applies to the following histograms in this section.

The HAD/EM cut (Figure 3.11) is identical:

$$\frac{E_{HAD}}{E_{EM}} < 0.055 + 0.00045 \times E_{cl}[\text{GeV}]. \tag{3.28}$$

- **Lateral shower shape: L_{SHR}**

  Since we do not know the response of low energy photons so well, we loosen the threshold for L_{SHR} (Figure 3.12):

$$L_{SHR} < 0.5. \tag{3.29}$$

- **Lateral shower shape: CES χ^2**

  For CES χ^2 cut, Figure 3.13, we use information on both views:

$$\frac{\chi^2_{Strip} + \chi^2_{Wire}}{2} < 20. \tag{3.30}$$

- **Fiducial region**

  Fiducial cuts are identical:

$$|x| < 21.0 \text{ cm}, \tag{3.31}$$

$$9.0 < |z| < 230.0 \text{ cm}. \tag{3.32}$$

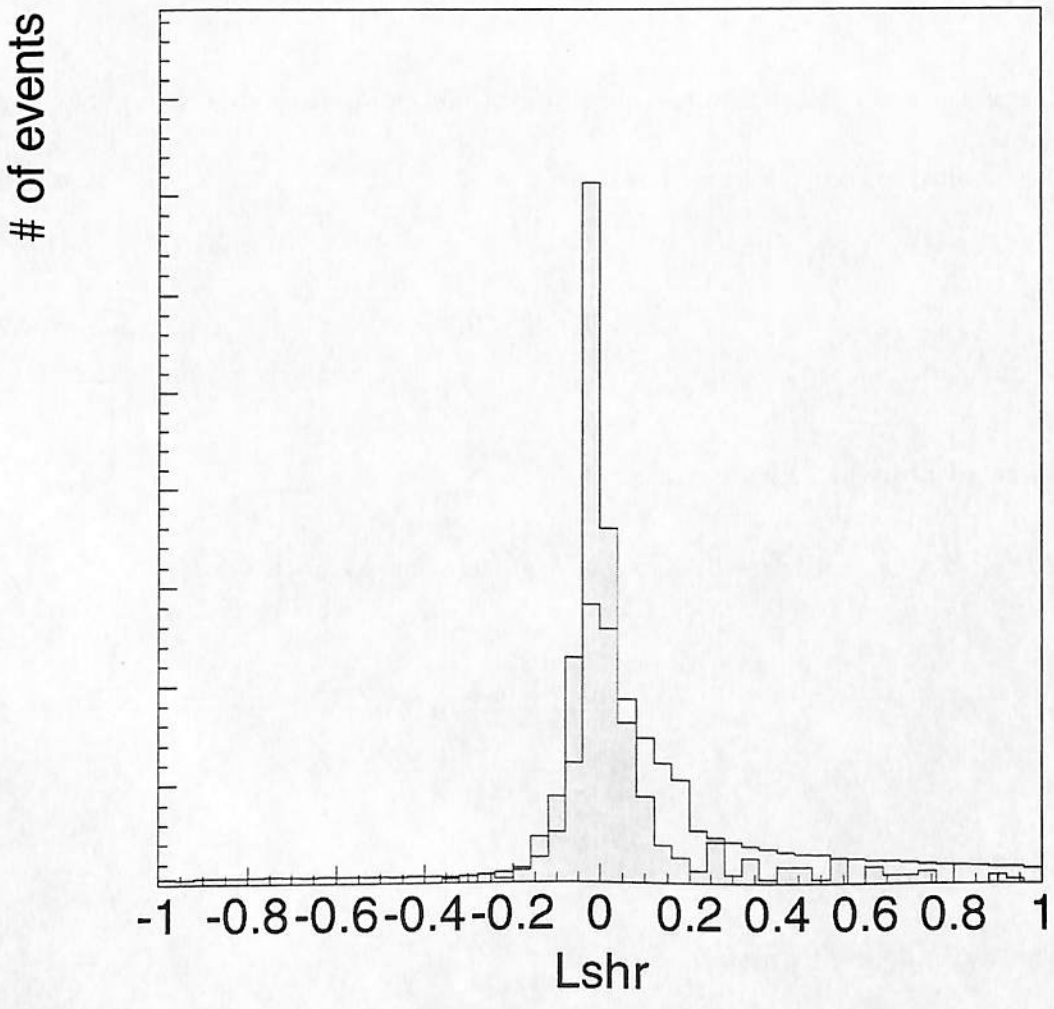

Figure 3.12: Lateral profile distributions for photon candidates (shaded) and backgrounds (clear).

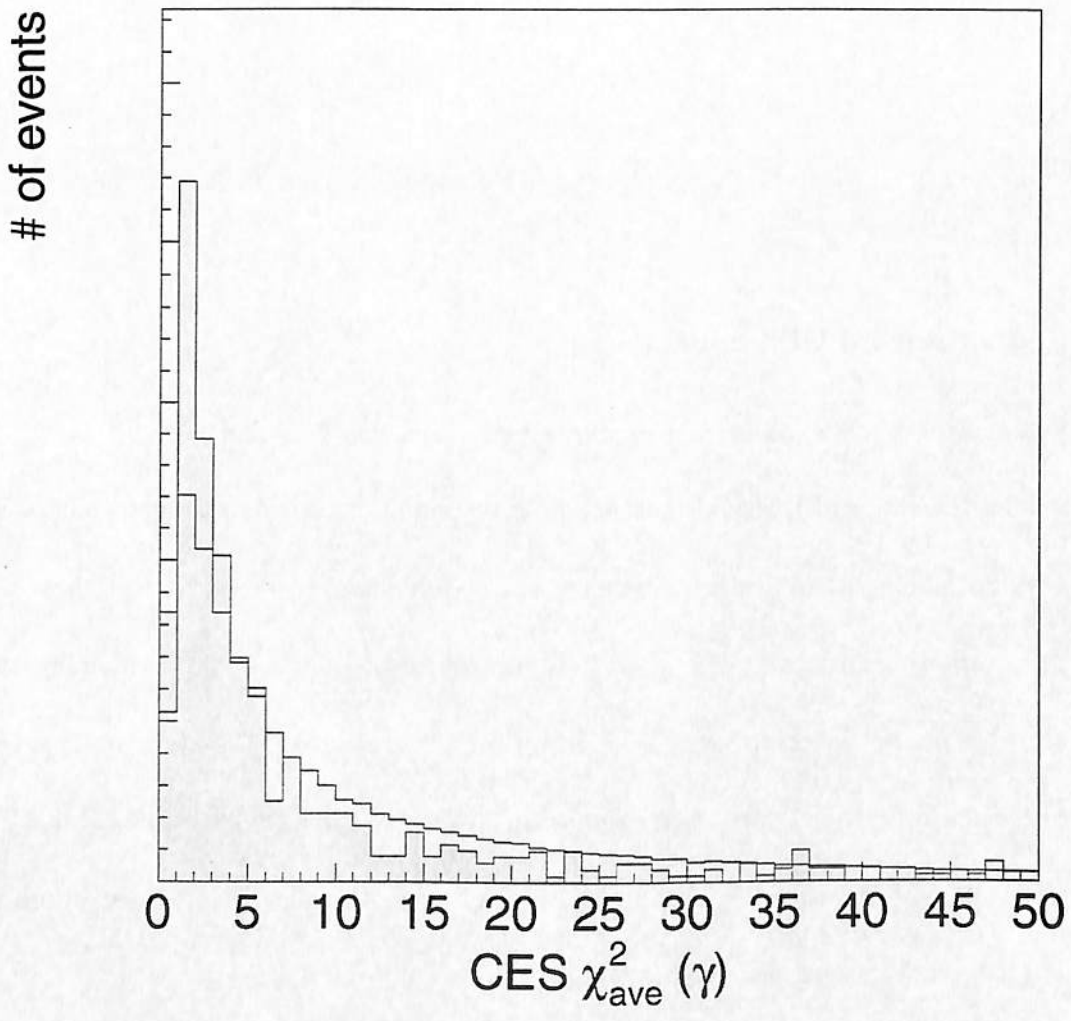

Figure 3.13: The average CES χ^2 distributions for photon candidates (shaded) and backgrounds (clear).

- **Number of associated charged tracks**

  For photons, we require at most 1 track (originating from any vertex) pointing to the cluster and the track if present must have considerably low PT as compared with the energy measured in the calorimeters (Figure 3.14):

$$N_{3D} = 0, \text{ or} \tag{3.33}$$

$$\mathrm{P_{T}}_{trk} < 0.1 \times \mathrm{E_{T}}_{cl} \text{ if } N_{3D} = 1. \tag{3.34}$$

- **Sliding second CES cluster cut**

  The major backgrounds to low energy photons are π^0s and η^0s, all of which would develop multiple EM clusters close to one another. When the two clusters overlap in CES, the lateral shower shape would deviate largely from that of a single photon and the CES χ^2 cut eliminates most of them, but when the two clusters do not overlap, it would result in a reasonable χ^2 value for a single photon. To further suppress these backgrounds, we look for an extra hit in CES near the EM cluster. Figures 3.15 and 3.16 show the distributions of numbers of CES clusters and those of the energy of the second CES cluster in the same wedge as the EM cluster of the photon candidates. We remove events with multiple CES clusters if the energy of the second cluster is larger than a certain

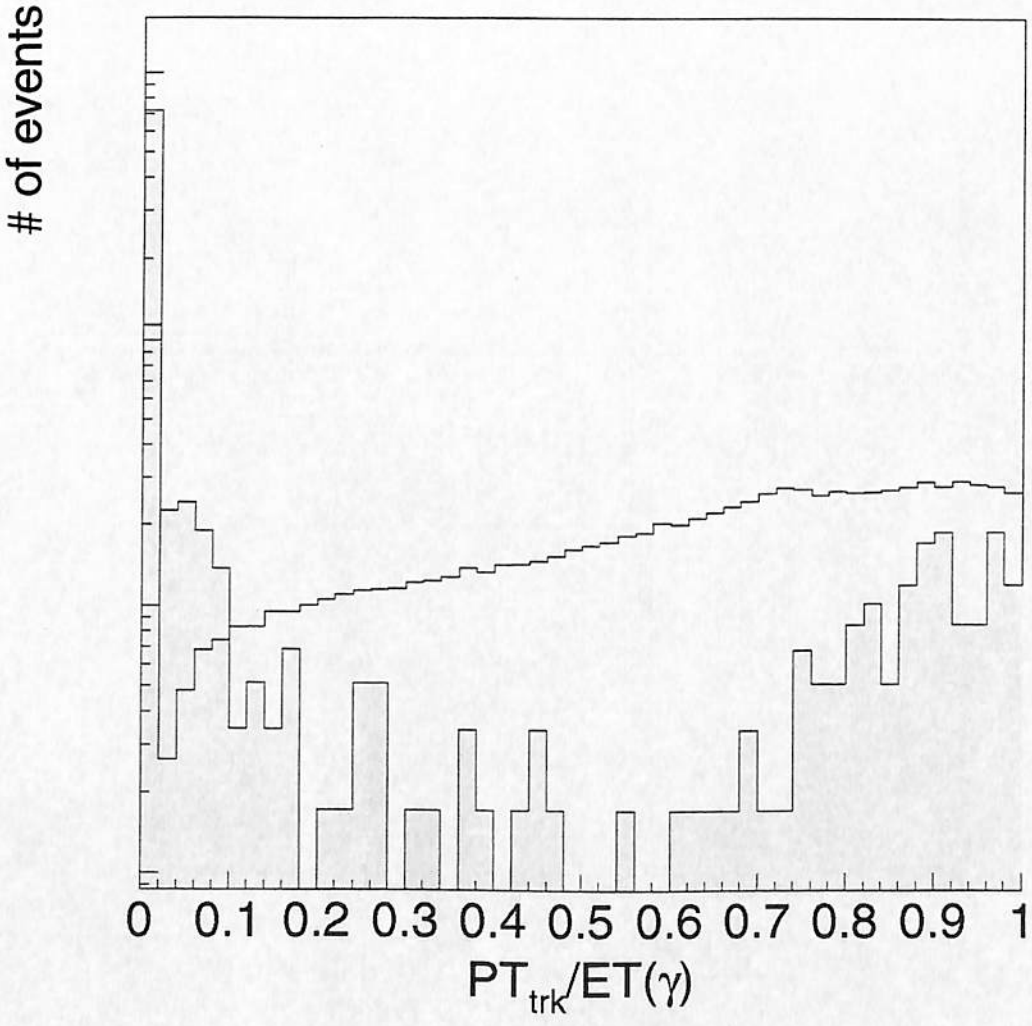

Figure 3.14: Distributions of the highest P_T tracks pointing to the EM cluster for photon candidates (shaded) and backgrounds (clear).

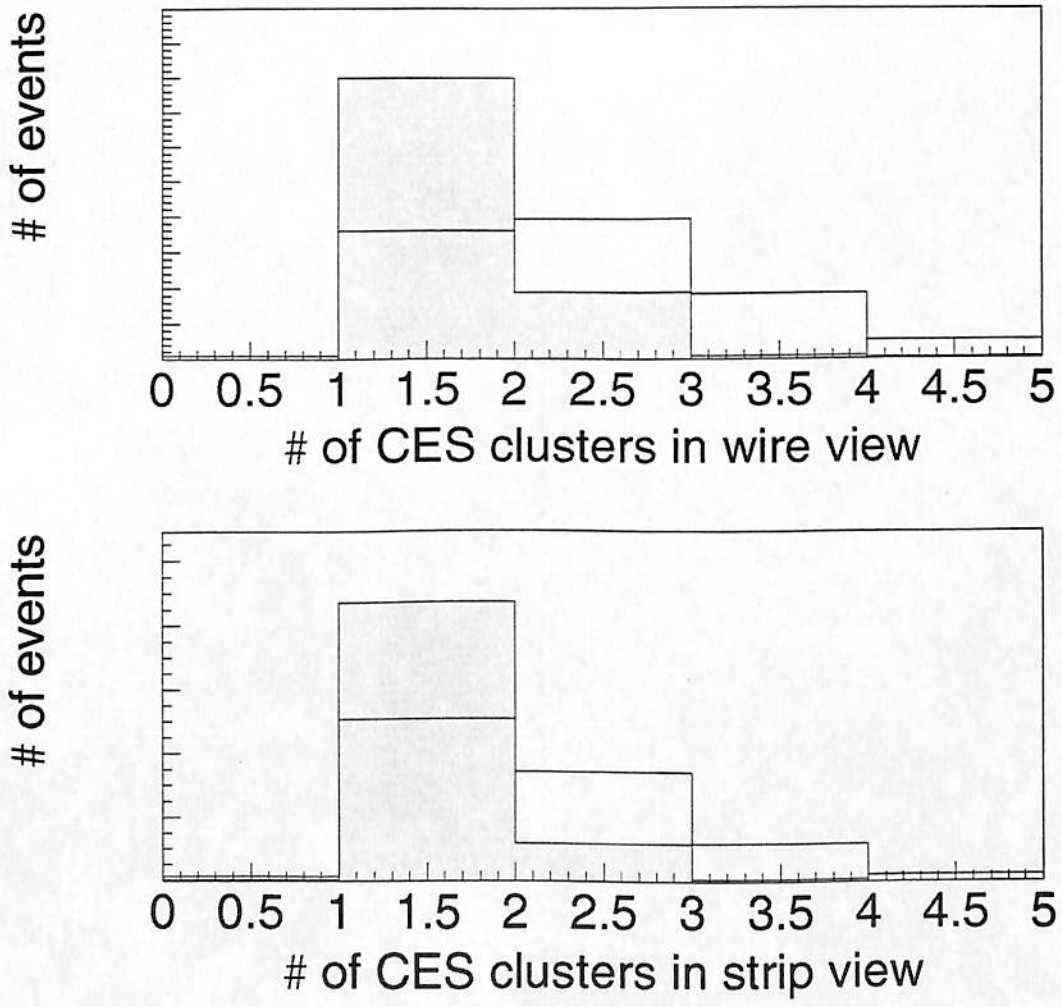

Figure 3.15: Distributions of numbers of CES clusters for photon candidates (shaded) and backgrounds (clear).

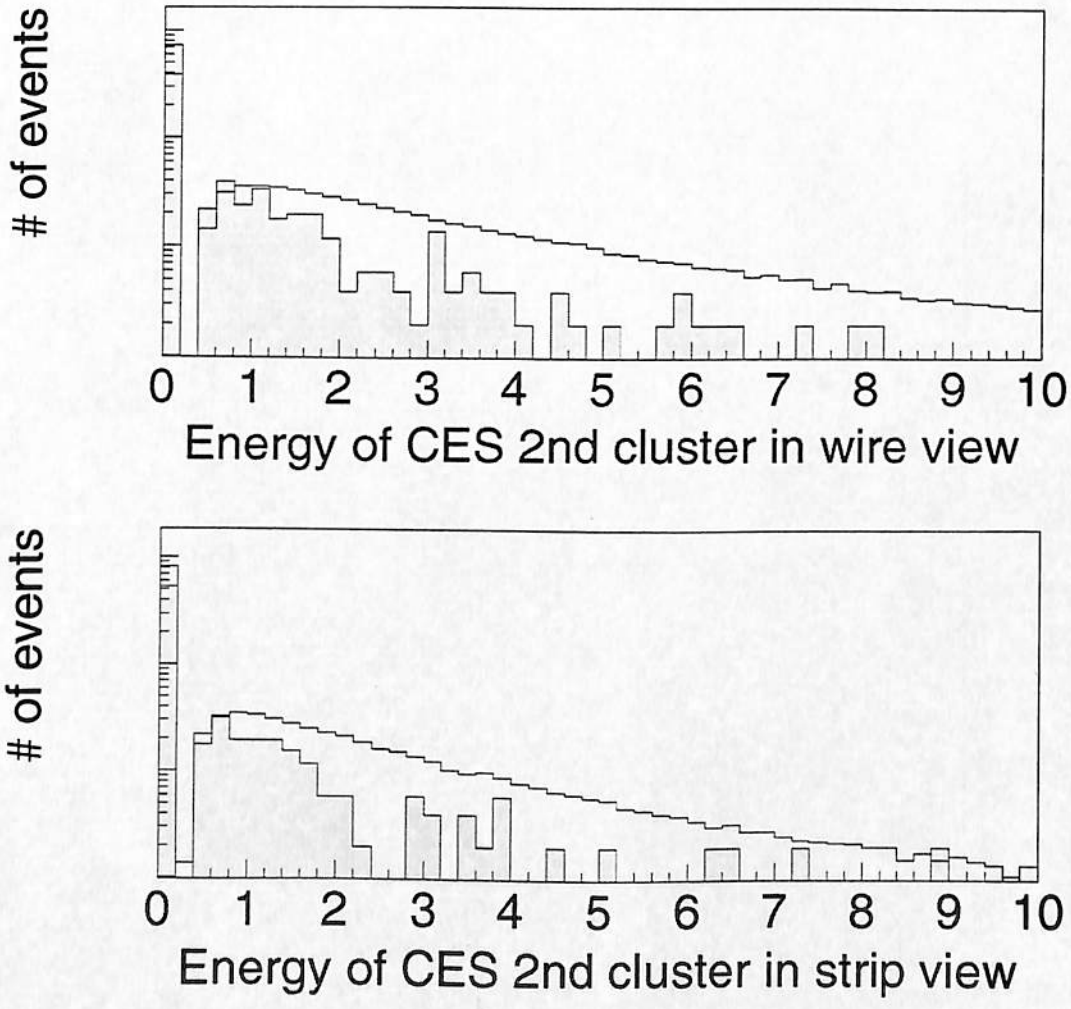

Figure 3.16: Distributions of 2nd clusters in the CES for photon candidates (shaded) and backgrounds (clear).

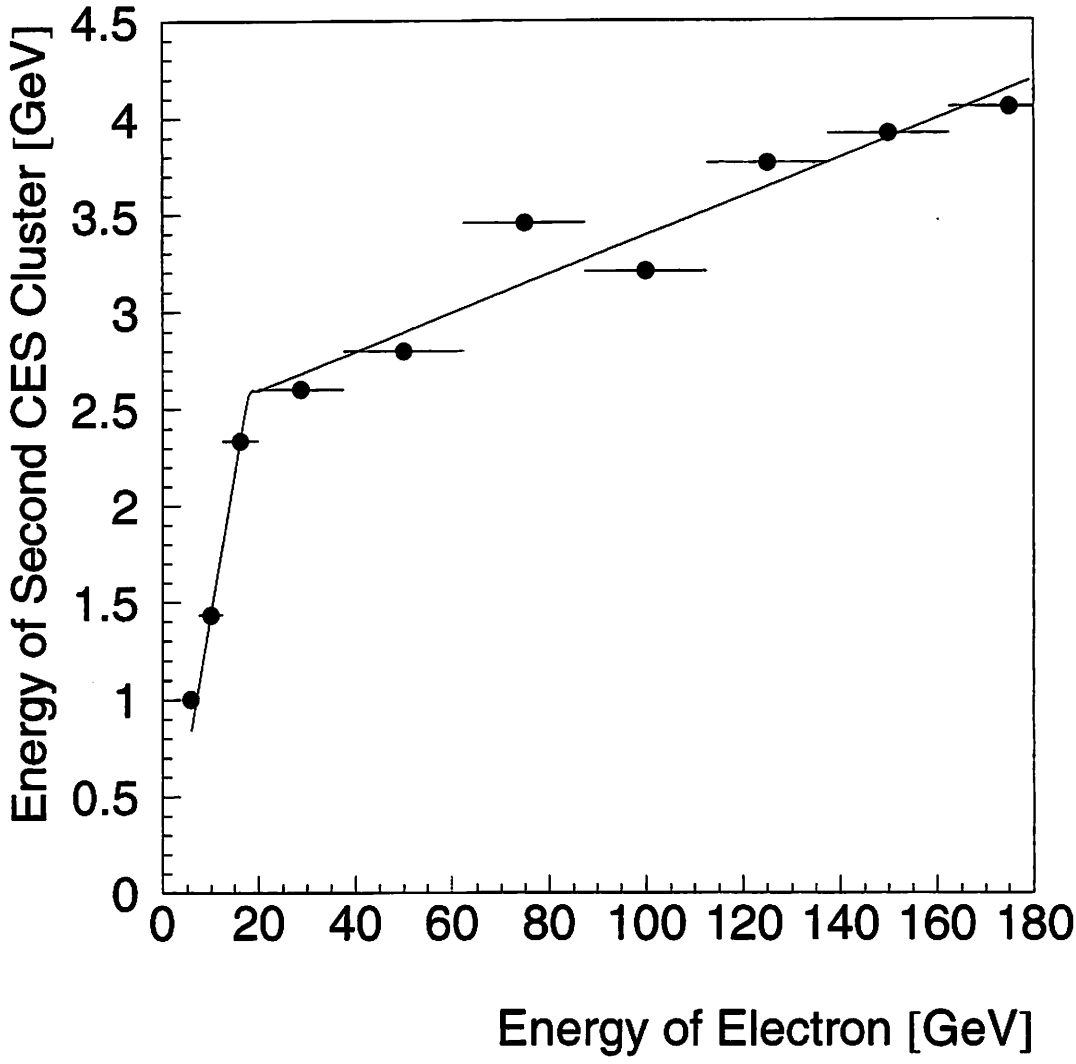

Figure 3.17: The 98% threshold lines of the second CES cluster energy in testbeam electron. 98% of the time the energy of the second CES cluster is below the line.

threshold in either strip or wire view:

$$E^{2nd}_{Strip} < E_{max}, \tag{3.35}$$

$$E^{2nd}_{Wire} < E_{max}, \tag{3.36}$$

where E^{2nd}_{Strip} and E^{2nd}_{Wire} are the energies of the second CES clusters, if any, in strip and wire views, and

$$E_{max} = \begin{cases} -0.0095 + 0.14 \times E_\gamma, & \text{if } E_\gamma < 17.9 \text{ GeV}, \\ 2.4 + 0.010 \times E_\gamma, & \text{otherwise.} \end{cases} \tag{3.37}$$

The threshold E_{max} was determined by fitting the test beam electron data to make the cut 98% efficient for real EM clusters, as shown in Figure 3.17.

3.5 Suppressing Z candidate events

We remove Z candidate events by looking for the other decay lepton ℓ_2, which is required to satisfy somewhat looser quality cuts. We look for an oppositely charged track originating from the same vertex as the first lepton ℓ_1.

For second electrons, we require:

$$\frac{E_{HAD}}{E_{EM}} < 0.1, \tag{3.38}$$

$$\frac{E}{P} < 2.0. \tag{3.39}$$

(3.40)

We accept electrons in the plug region as well as in the central region if they are associated with a track.

For second muons we only look at their response in the calorimeters:

$$E_{EM} < 2.0 \text{ GeV}, \tag{3.41}$$

$$E_{HAD} < 6.0 \text{ GeV}. \tag{3.42}$$

If the event contains a candidate for the second lepton and satisfies the following Z selection criteria, it is tagged as a Z candidate event and will not be used in this analysis:

$$P_{T\ell_1} > 20.0 \text{ GeV}, \tag{3.43}$$

$$P_{T\ell_2} > 10.0 \text{ GeV}, \tag{3.44}$$

$$I^{cal}_{\Delta R<0.4}(\ell_1) < 0.1 \times P_{T\ell_1}, \tag{3.45}$$

$$I^{cal}_{\Delta R<0.4}(\ell_2) < 0.1 \times P_{T\ell_2}, \tag{3.46}$$

$$M_{\ell_1\ell_2} > 65.0 \text{ GeV}. \tag{3.47}$$

where $I^{cal}_{\Delta R<0.4}(\ell)$ is the scalar sum of all the transverse energies E_T^{cal} inside a cone of radius 0.4 in ΔR from the calorimeter cluster for the lepton ℓ, excluding the energy

of the lepton cluster ($E_{T\,cl}$) itself:

$$I^{cal}_{\Delta R<0.4}(\ell) = (\sum_{\Delta R<0.4} E^{cal}_T) - E_{T\,cl}, \tag{3.48}$$

and $M_{\ell_1\ell_2}$ is the invariant mass of the two leptons:

$$M_{\ell_1\ell_2} = \sqrt{E_{\ell_1} E_{\ell_2} - \vec{P}_{\ell_1} \cdot \vec{P}_{\ell_2}}. \tag{3.49}$$

Second track cut to further remove possible Zs

The W sample so obtained possibly contains some more Z events where one of the decay leptons moves out of the fiducial region[4] (in high-$|\eta|$ regions or into cracks for example) and is misidentified as $\not\!\!E_T$. The CTC coverage is larger than the muon chambers and is more crack-free than the central calorimeters, so we could remove some of these events by searching for isolated tracks originating from the same vertex that could form a large invariant mass $M_{\ell trk}$ with the charged lepton from the W candidates. Figure 3.18 shows the invariant mass distributions between the lepton and a second isolated track in the high P_T lepton samples. The remnants of the Zs and the Drell-Yan processes are clearly seen with unlike-sign pairs while like-sign pairs distribute randomly. We remove the event if it is associated with a track that

[4]These Z events are called "one-legged" Zs.

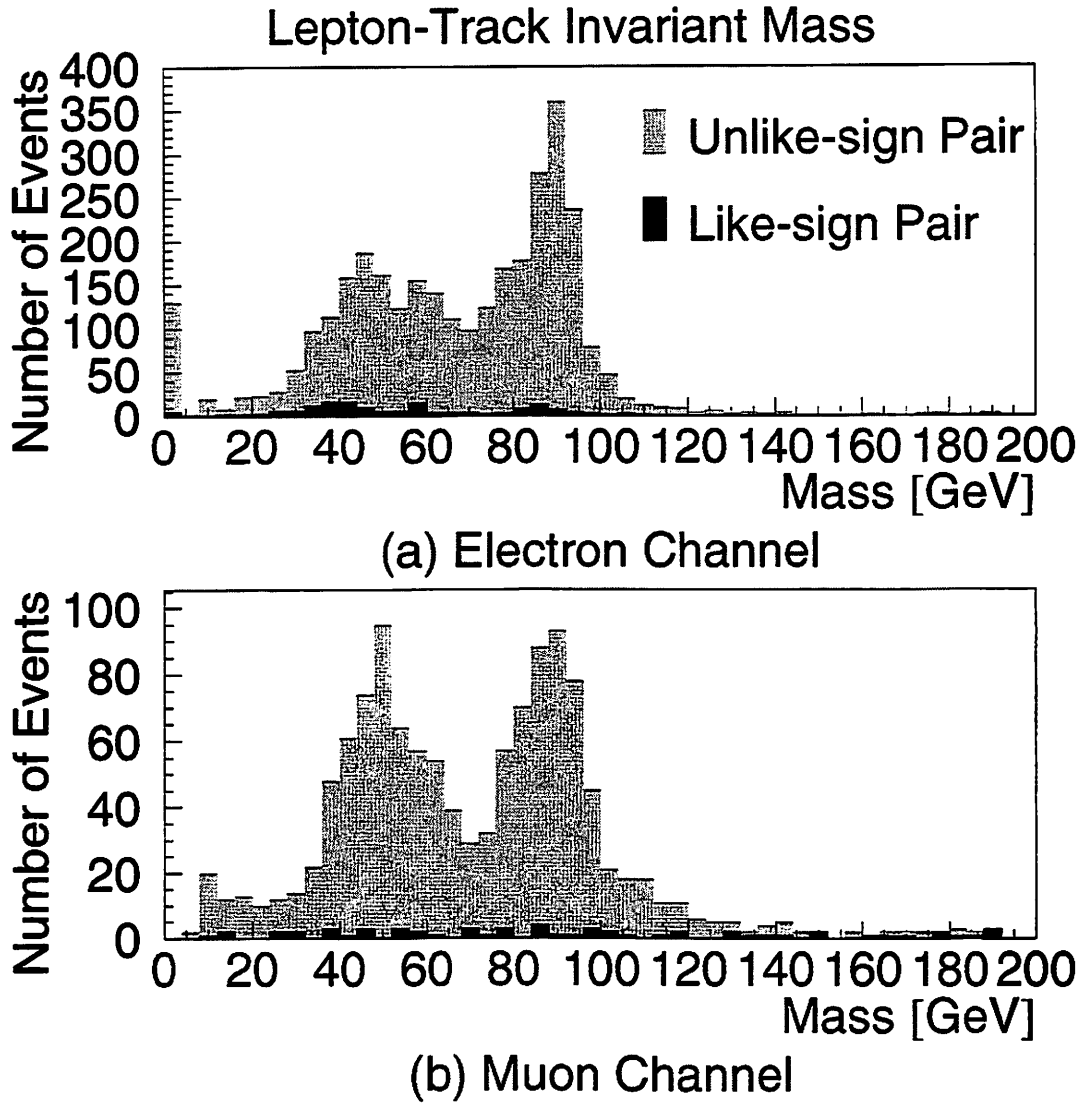

Figure 3.18: Invariant mass distributions between the charged lepton and a second, isolated, track in high P_T lepton samples.

satisfies the following condition:

$$M_{ltrk} \times Q_l \times Q_{trk} > -40.0\,\text{GeV}. \tag{3.50}$$

3.6 $\not\!\!E_T$ Measurement and Corrections

The neutrinos interact with matter even less (and much less) than the muons and we assume they all escape totally undetected. When only one neutrino is involved in the event, we can measure the transverse components of its momentum by measuring *everything else*:

$$\vec{\not\!\!E}_{T_{raw}} = -\sum_i \vec{E}_{T_i}, \tag{3.51}$$

where $\vec{E}_{T_i}$ is the energy deposit (both EM and hadronic) in tower address i projected to the transverse plane.

The vector $\vec{\not\!\!E}_{T_{raw}}$ needs some corrections before it can be used as the transverse energy of the neutrino:

- $\vec{\not\!\!E}_{T_{raw}}$ contains uncorrected energies for electrons and photons. We correct for these, and we want to reflect the changes in the $\not\!\!E_T$ measurement as well.
- Muons do not deposit most of their energy in calorimeter so we need to take that into account if we have muons in the event.
- The energy correction for jets is at the 40% level. This results in undercounting

energy from jets and "unclustered energy"; we see apparent $\not\!\!E_T$ when there is no true missing energy. We do not explicitly look at jet activities in this analysis, but we need them to correct for this effect to get the $\not\!\!E_T$ right.

The corrections begin by getting the unclustered energy E_{Tu} of the event, which is the remaining energies after all the clustered energies (including the small deposit from the muons) are removed:

$$\vec{E}_{Tu} = -1.5\left(\vec{\not\!\!E}_{T\,raw} + \sum \vec{E}_{Te}^{\,raw} + \sum \vec{E}_{T\mu}^{\,raw} + \sum \vec{E}_{T\gamma}^{\,raw} + \sum \vec{E}_{Tjet}^{\,raw}\right). \qquad (3.52)$$

where the factor 1.5 corrects for detector nonlinearity for low energy particles.

The corrected $\not\!\!E_T$ is obtained by putting back the (appropriately corrected) clustered energies:

$$\vec{\not\!\!E}_{T\,corr} = -\vec{E}_{Tu} - \sum \vec{E}_{Te}^{\,corr} - \sum \vec{E}_{T\mu}^{\,corr} - \sum \vec{E}_{T\gamma}^{\,corr} - \sum \vec{E}_{Tjet}^{\,corr}. \qquad (3.53)$$

3.7 W Identification

The W inclusive samples are extracted from high P_T lepton samples by requiring an isolated high P_T electron or muon that satisfies the quality cuts specified in the previous sections and a large $\not\!\!E_T$ in the event:

$$P_{T\ell}^{corr} > 20 \text{ GeV}, \qquad (3.54)$$

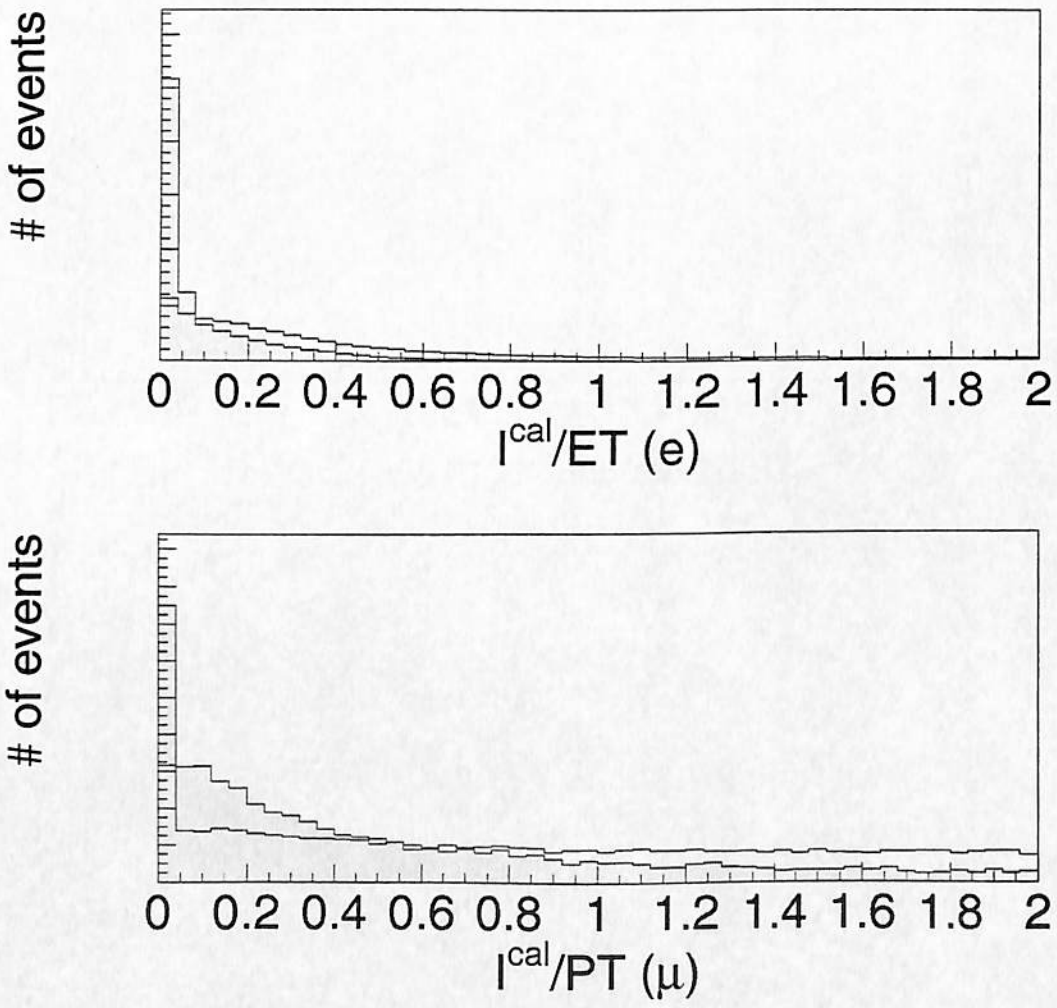

Figure 3.19: Distributions of calorimeter energies around W electrons (shaded) and backgrounds (clear).

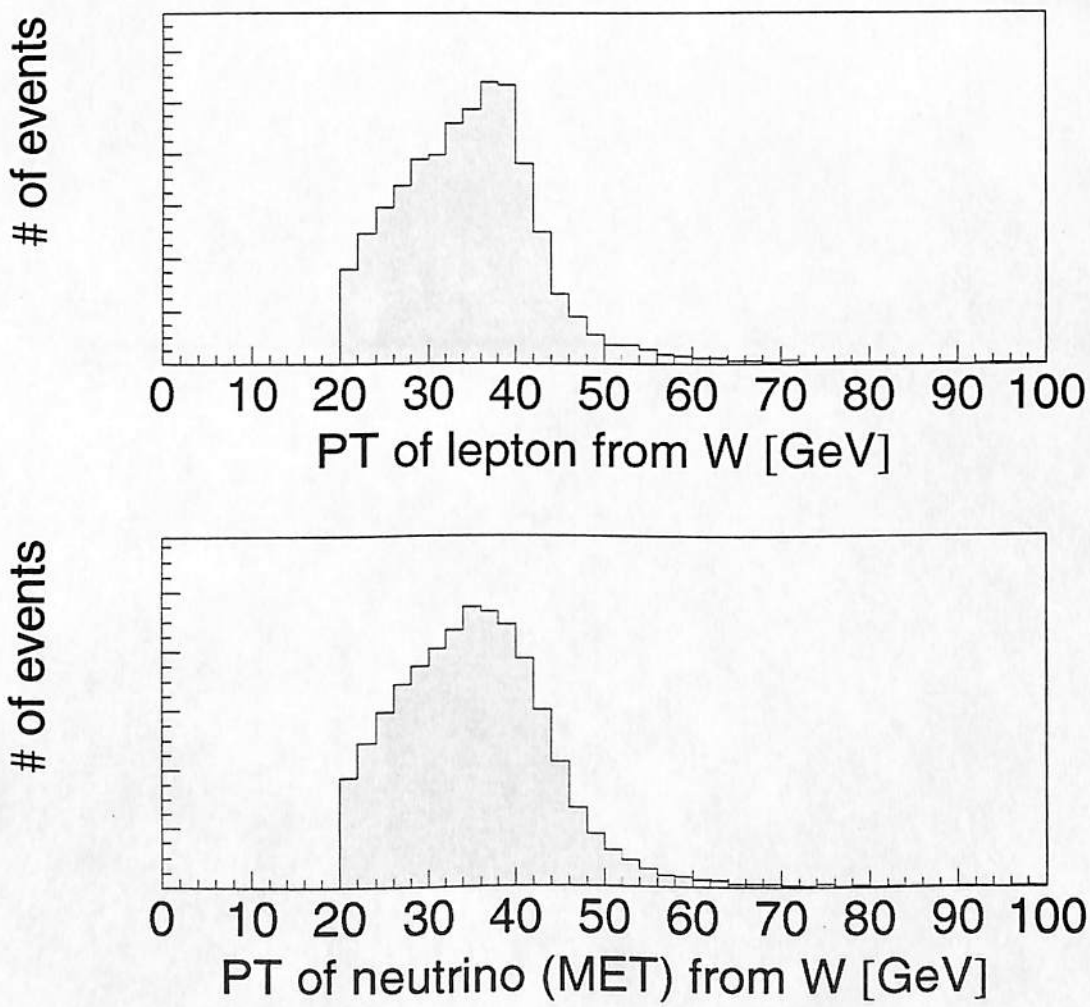

Figure 3.20: P_T distributions of W leptons.

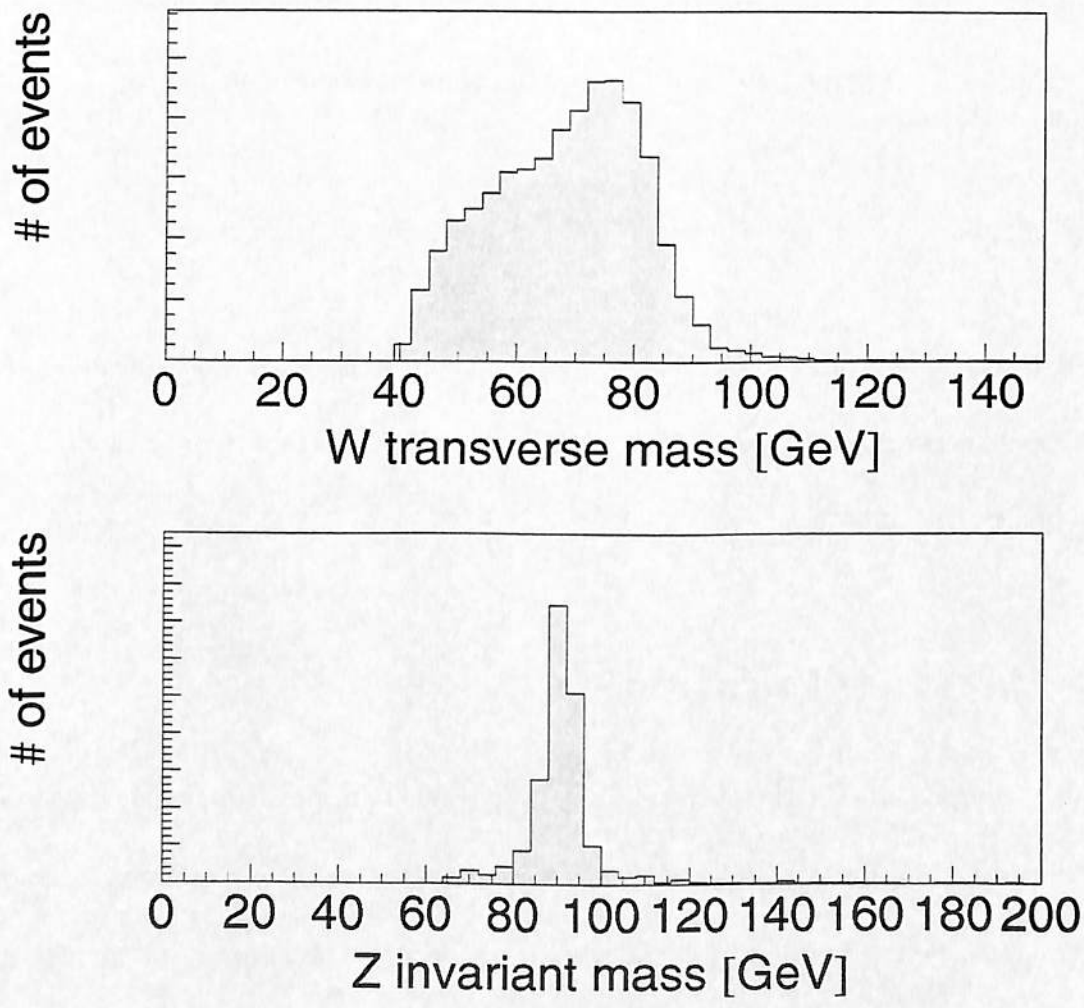

Figure 3.21: Distributions of W transverse mass and Z mass.

$$I^{cal}_{\Delta R<0.4}(\ell) \;<\; 0.1 \times \mathrm{P_{T\ell}}, \tag{3.55}$$

$$\not\!\!\mathrm{E_T}^{corr} \;>\; 20\ \mathrm{GeV}, \tag{3.56}$$

$$\mathrm{M_{T\ell\nu}} \;>\; 40\ \mathrm{GeV}. \tag{3.57}$$

where $I^{cal}_{\Delta R<0.4}(\ell)$ is the calorimeter energies around the lepton candidates normalised to the lepton $\mathrm{E_T}$ (Figure 3.19) and $\mathrm{M_{T\ell\nu}}$ is the transverse mass defined by

$$\mathrm{M_{T\ell\nu}} = \sqrt{2\mathrm{E_{T\ell}}\not\!\!\mathrm{E_T}(1-\cos\Delta\phi_{\ell\nu})}. \tag{3.58}$$

Figures 3.20 and 3.21 show the $\mathrm{P_T}$ distributions of the W decay leptons as well as the transverse mass of the W and the mass of the Z selected by the quality cuts described in this chapter.

3.8 Wγ Identification

The Wγ samples are extracted from the W inclusive samples by requiring an additional isolated photon associated with the W boson. To remove inner Bremsstrahlung events to some extent, we require the photon to be well separated from the charged lepton.

$$\mathrm{P_{T\gamma}} \;>\; 7.0\ \mathrm{GeV}, \tag{3.59}$$

$$I^{cal}_{\Delta R<0.4}(\gamma) \;<\; 0.15 \times \mathrm{P_{T\gamma}}, \tag{3.60}$$

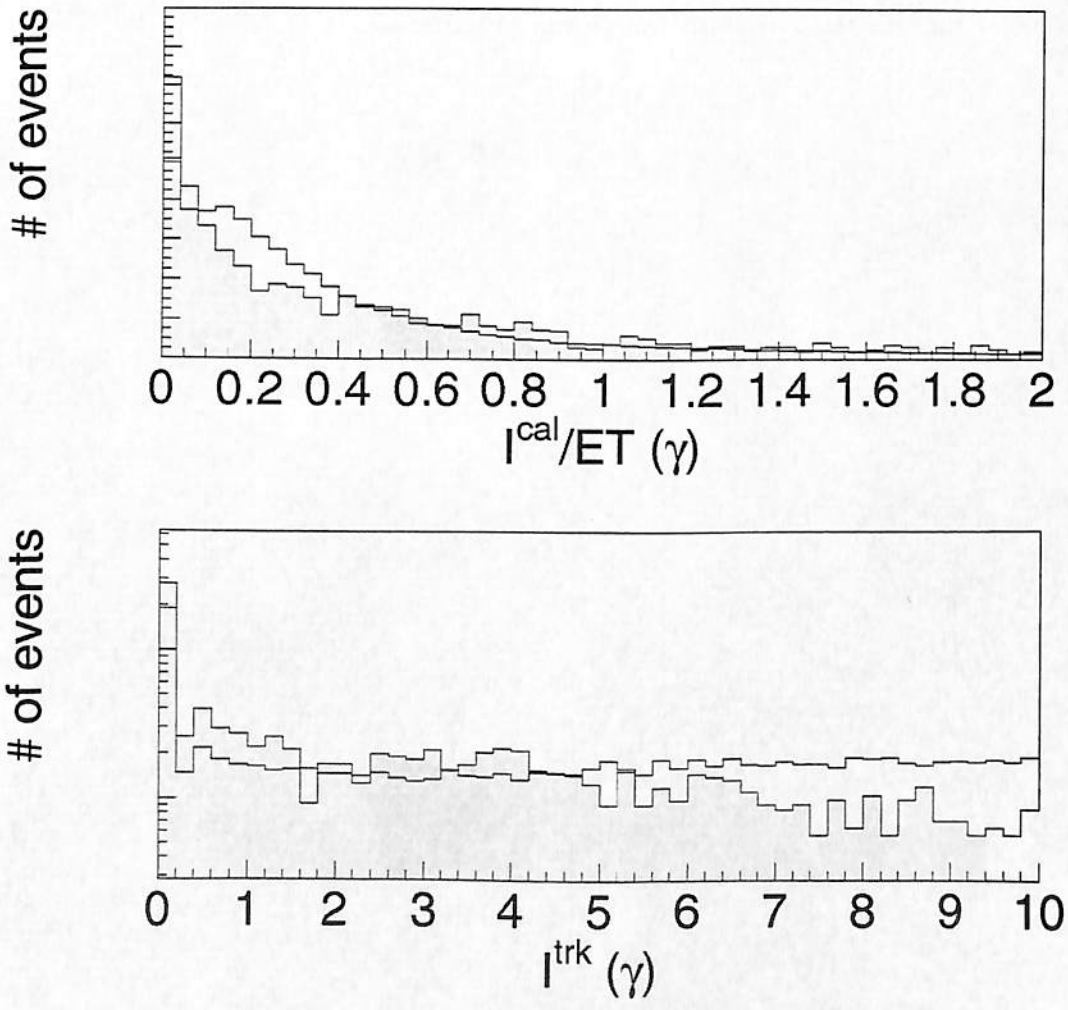

Figure 3.22: Distributions of calorimeter energies around photon candidates (shaded) and backgrounds (clear).

$$I^{trk}_{\Delta R<0.4}(\gamma) \;<\; 2.0\,\mathrm{GeV}, \tag{3.61}$$

$$\Delta R_{\ell\gamma} \;>\; 0.7. \tag{3.62}$$

where $I^{trk}_{\Delta R<0.4}(\gamma)$ is the scalar sum of all the transverse momenta $\mathrm{P}_\mathrm{T}^{trk}$ of tracks inside a cone of radius 0.4 in ΔR from the photon (Figure 3.22):

$$I^{trk}_{\Delta R<0.4}(\gamma) = \sum_{\Delta R<0.4} \mathrm{P}_\mathrm{T}^{trk}. \tag{3.63}$$

Chapter 4

Data vs. Standard Model Predictions

After applying all the cuts described in the previous chapter, we are left with a total of 202 Wγ candidate events. In this section, these candidate events are compared with the Standard Model predictions.

4.1 The Baur Event Generator

The Standard Model predictions for the Wγ production are determined using Monte Carlo data samples generated by the Baur Monte Carlo event generator followed by the FMC detector simulation.

The Baur Wγ Monte Carlo event generator [39] performs complete helicity calculations of all the tree-level Feynman diagrams shown in Figure 1.1 with arbitrary $\Delta\kappa$,

λ, $\tilde{\kappa}$, and $\tilde{\lambda}$. The kinematical phase space is calculated with the VEGAS adaptive multidimensional integration program [9,12]. The generator includes parton-parton luminosities as well as Cabibbo-Kobayashi-Maskawa quark-mixing matrix elements. [2,6] Higher-order QCD contributions such as $q + \bar{q} \rightarrow \mathrm{W} + \gamma + g$ and $q + g \rightarrow \mathrm{W} + \gamma + q$ are approximated by a K-factor [40]

$$K = 1 + \frac{8\pi}{9}\alpha_s(Q^2 = \mathrm{M}_\mathrm{W}^2) \approx 1.33. \tag{4.1}$$

The MRS D'_ structure function [45] is used in this analysis, as it best describes the CDF W charge asymmetry results. [50]

The Baur event generator outputs the four-momenta of the decay leptons and the photon, with event weight that is proportional to the probability that an event with the kinematical features of that event will occur. To avoid singularities the following minimum set of loose cuts are applied:

- $\mathrm{P_T}(\gamma) > 5$ GeV
- $\mathrm{P_T}(\ell) > 1$ GeV
- $\mathrm{P_T}(\nu) > 1$ GeV
- $\Delta\mathrm{R}_{\ell\gamma} > 0.6$
- $|\eta| < 6.0$ for ℓ, ν, and γ

4.2 The CDF Detector Simulation

The four-momenta associated with the final state particles are then processed by a fast CDF detector simulation program called FMC. It also simulates the underlying activities to mimic a real CDF event.

After reading each event generated by the Baur event generator it picks up a z vertex with a Gaussian distribution of $\sigma = 30$ cm and adds a P_T-boost to the Wγ system according to the P_T distributions of the W/Z inclusive events measured with CDF. The charged lepton and the photon four-momenta are then smeared using the detector resolutions and the $\not\!\!E_T$ of the event is recalculated. Although all the four components of the neutrino momentum are available, the FMC does not use them directly. In particular, the z-component is simply ignored. The lepton and the photon are required to be within the fiducial regions defined in Chapter 3. The event weight is multiplied by the efficiencies.

4.3 Background Estimations

The largest background to the Wγ process is by far the W + *jets* events where a jet is misidentified as an isolated photon. For instance, a jet may have fragmented into a leading π^0 or η^0, which subsequently decays into two photons; If one of these photons happens to be lost in a crack between the calorimeter wedges or develop a shower too close to the other photon, we would only see a response consistent with

that of a single photon in the calorimeter and the event would pass the Wγ selection cuts. We estimate the probability $\mathcal{P}(jet \rightarrow \text{“}\gamma\text{”})$ of jets being misidentified as single isolated photons by examining an independent sample of CDF inclusive jet events.

The data sample used in this study is triggered by an isolated EM-rich cluster with $E_T > 16$ GeV. We look for an *extra* photon-like object in the central region in much the same way we look for an extra photon in W inclusive samples. The trigger jets are excluded from the analysis as they have already passed the trigger requirements and would introduce a large bias into the results otherwise. To avoid the complication caused by overlapping jets we require the candidate jets to be well separated from the trigger jets. Since we use a cone size of 0.7 in the jet clustering algorithm, we require the separation $\Delta R_{jj} > 1.4$.

To each of the jets that pass these requirements, we apply the photon cuts described in Chapter 3 and count how many of them pass the cuts. The number of real prompt photons in the sample are estimated statistically by an independent method using the averaged CES χ^2 values and the number is subtracted from the count.

The probability of misidentifying a jet as a photon is defined by the fraction of the jets that pass the photon selection criteria:

$$\mathcal{P}(jet \rightarrow \text{“}\gamma\text{”}) = \frac{N_{passed} - N_{prompt}}{N_{tested}}, \tag{4.2}$$

where N_{tested} is the number of jets tested, N_{passed} is the number of jets that satisfied

the photon selection criteria, and N_{prompt} is the number of prompt photons estimated. Figure 4.1 shows the probability as a function of E_T ("γ"). [48]

The number of QCD background events in the following distributions is estimated by applying this probability function $\mathcal{P}(jet \rightarrow \text{"}\gamma\text{"})$ as the event weight when filling histograms for each jet in the W inclusive sample.

Other background processes considered in this analysis include

- "One-legged Z"s where one of the decay leptons moves out of the fiducial area and is misidentified as $\not\!\!E_T$. The leptons from Zs look very similar to the decay lepton from the W bosons, so these events would be very good W candidates. If a photon is also present ($Z\gamma$ events!) they will sneak into our $W\gamma$ candidate sample.[1] The second isolated track cut described in Chapter 3 will remove many of the one-legged Z events but some will remain.

- $W \rightarrow \tau\ \nu$ events where τ decays leptonically. The charged leptons from τ decays are softer than those directly from the W bosons and since multiple neutrinos are present in each event the net $\not\!\!E_T$ will become softer as well; but some fraction will survive our selection cuts.

These background events are estimated by running Baur MC+FMC. For one-legged Z events, $Z\gamma$ events are generated and fed into the FMC detector simulator treating one of the decay leptons as neutrino. For τ events, we generate $W\gamma$ events

[1]The ratio of $Z\gamma$ events to $W\gamma$ events is expected to be larger than that of Z to W due to a cancellation (RAZ) in the $W\gamma$.

in the τ channel with subsequent decay $\tau \rightarrow \ell\nu_\ell\nu_\tau$ (ℓ being either e or μ). The vector sum ν' of the three neutrinos are computed and ℓ and ν' are fed into the FMC detector simulator.

We apply the same Wγ selection cuts to these simulated events and make the same set of histograms using the events that survive the cuts. Contributions from these backgrounds are negligibly small as compared with the QCD background contribution from W + *jet* events, as shown in the next section.

4.4 Data vs. MC

In Figures 4.2–4.6 we show some of the distributions using the 202 Wγ candidate events. Overlaid are the Wγ Standard Model predictions, contributions from the W + *jets* events, and contributions from other backgrounds discussed in the previous section.

The 3-body transverse mass ($M_{T\ell\nu\gamma}$) and the 3-body minimum invariant mass ($M_{min\ell\nu\gamma}$) are defined below:

$$M^2_{T\ell\nu\gamma} = M^2_{T\ell\nu} + M^2_{T\nu\gamma} + M^2_{T\gamma\ell}, \tag{4.3}$$

$$M^2_{min\ell\nu\gamma} = 2E\!\!\!/_T\sqrt{E^2_{T\ell+\gamma} + m^2_{\ell+\gamma}} - 2\vec{P}_{T\ell+\gamma}\cdot\vec{E\!\!\!/}_T + m^2_{\ell+\gamma}. \tag{4.4}$$

The 2-body transverse mass M_{Tij} (i, j = ℓ, ν, or γ) is defined in Eq. 3.58. See Appendix A for the relationship between the 3-body minimum invariant mass and

the mass constrain cut used in Chapter 5.

They all agree reasonally well with the Standard Model predictions.

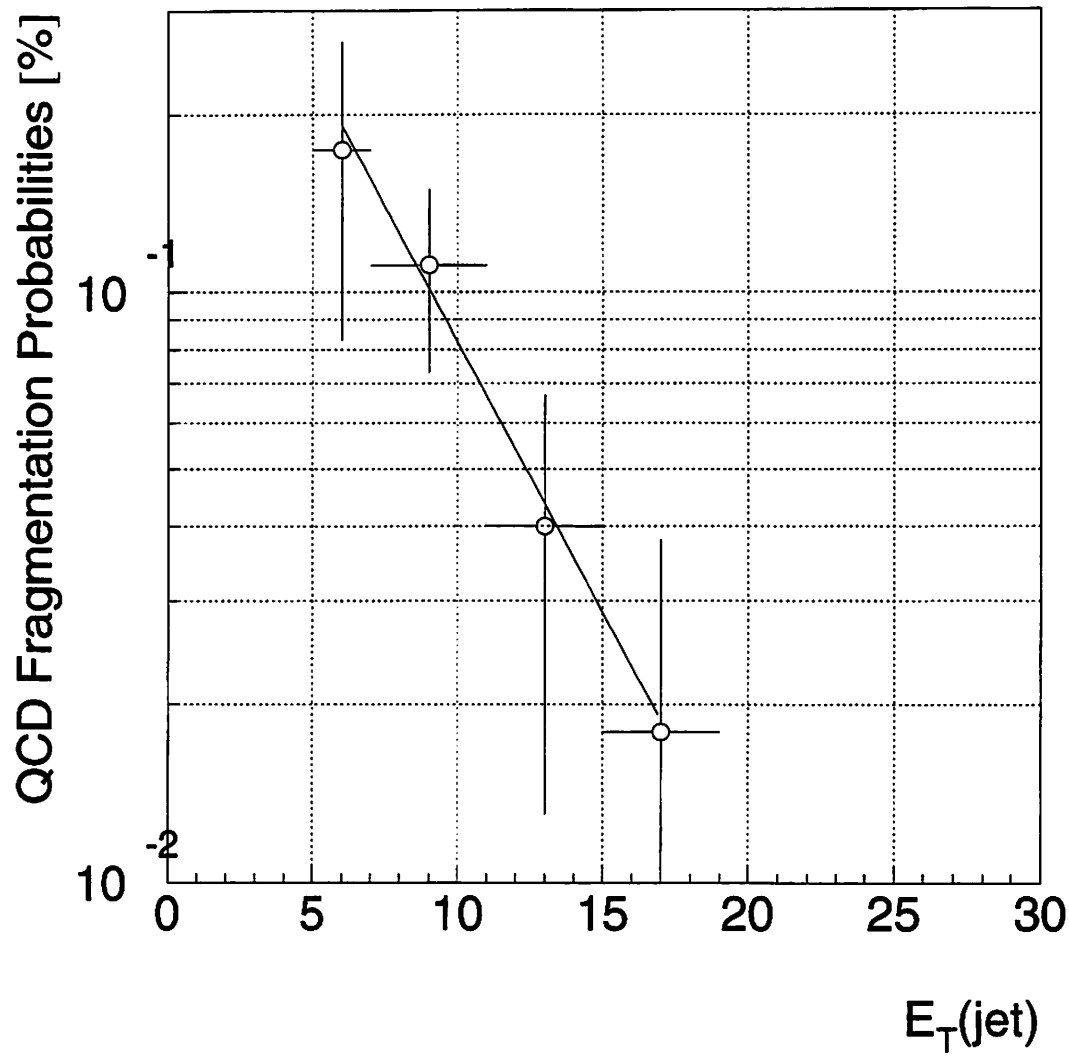

Figure 4.1: The *jet* → "γ" misidentification probability $\mathcal{P}$ as a function of E_T ("γ").

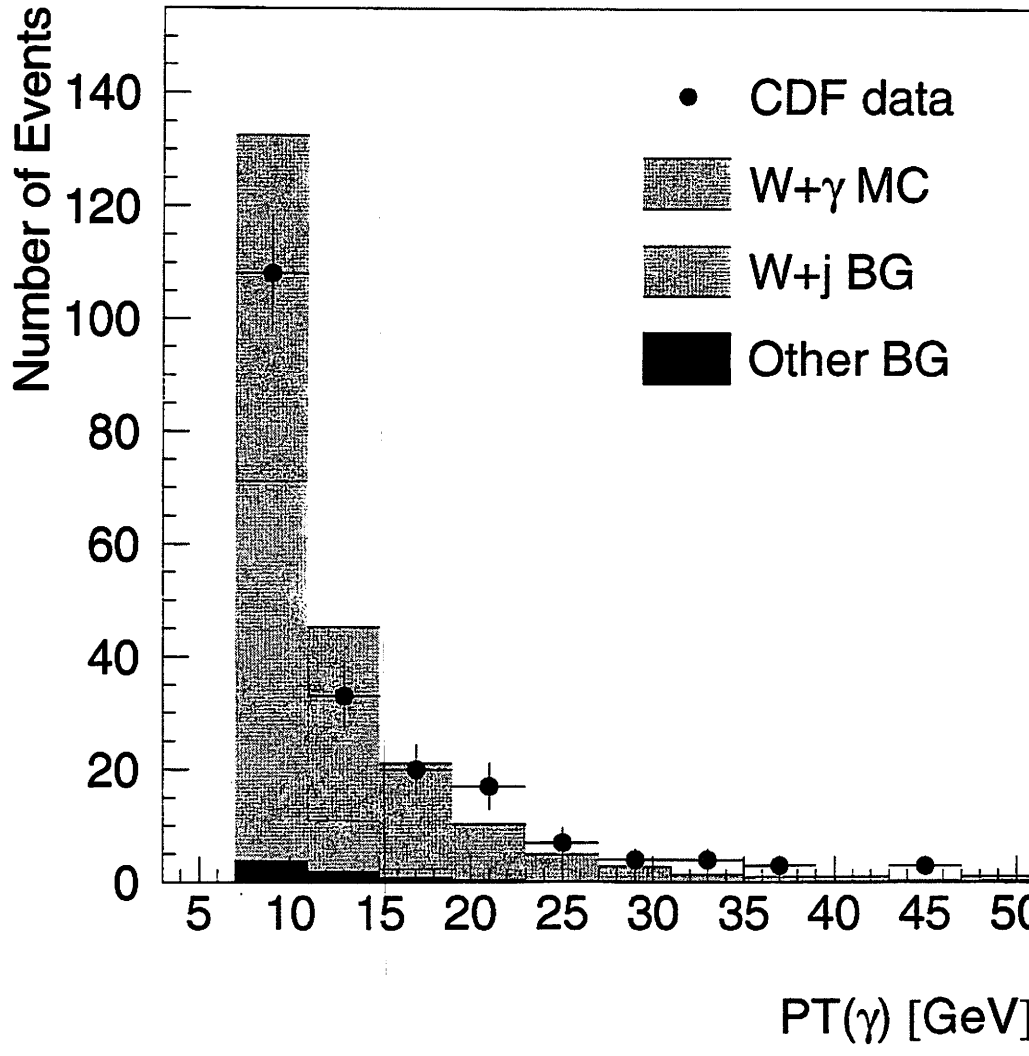

Figure 4.2: Photon P_T distribution. The CDF results are compared with the Standard Model predictions plus W + *jet* background where a jet fakes a photon and "Other BG" which include the contributions from $Z\gamma \rightarrow \ell$"ν"γ and $W\gamma \rightarrow \tau\nu\gamma \rightarrow \ell\nu'\gamma$.

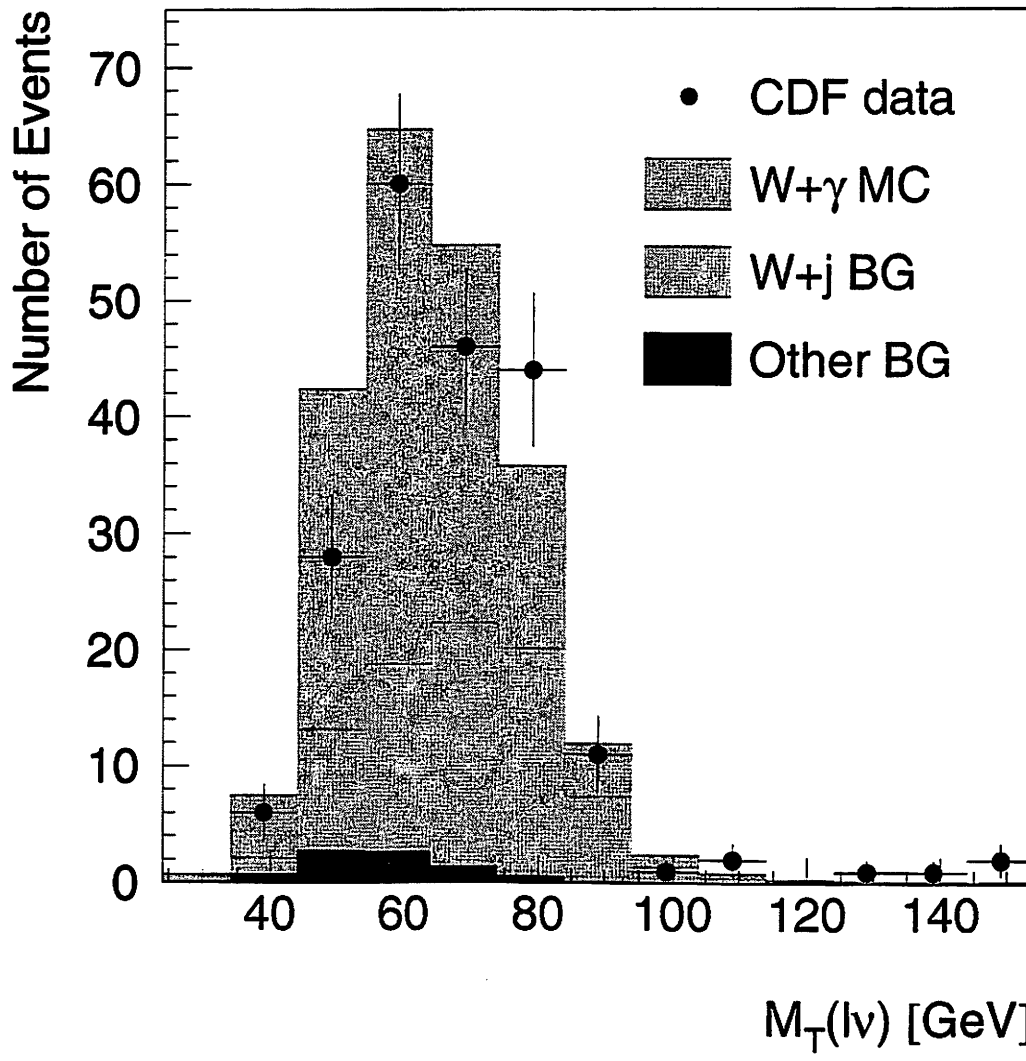

Figure 4.3: 2-body Transverse mass ($M_{T\,\ell\nu}$) distribution.

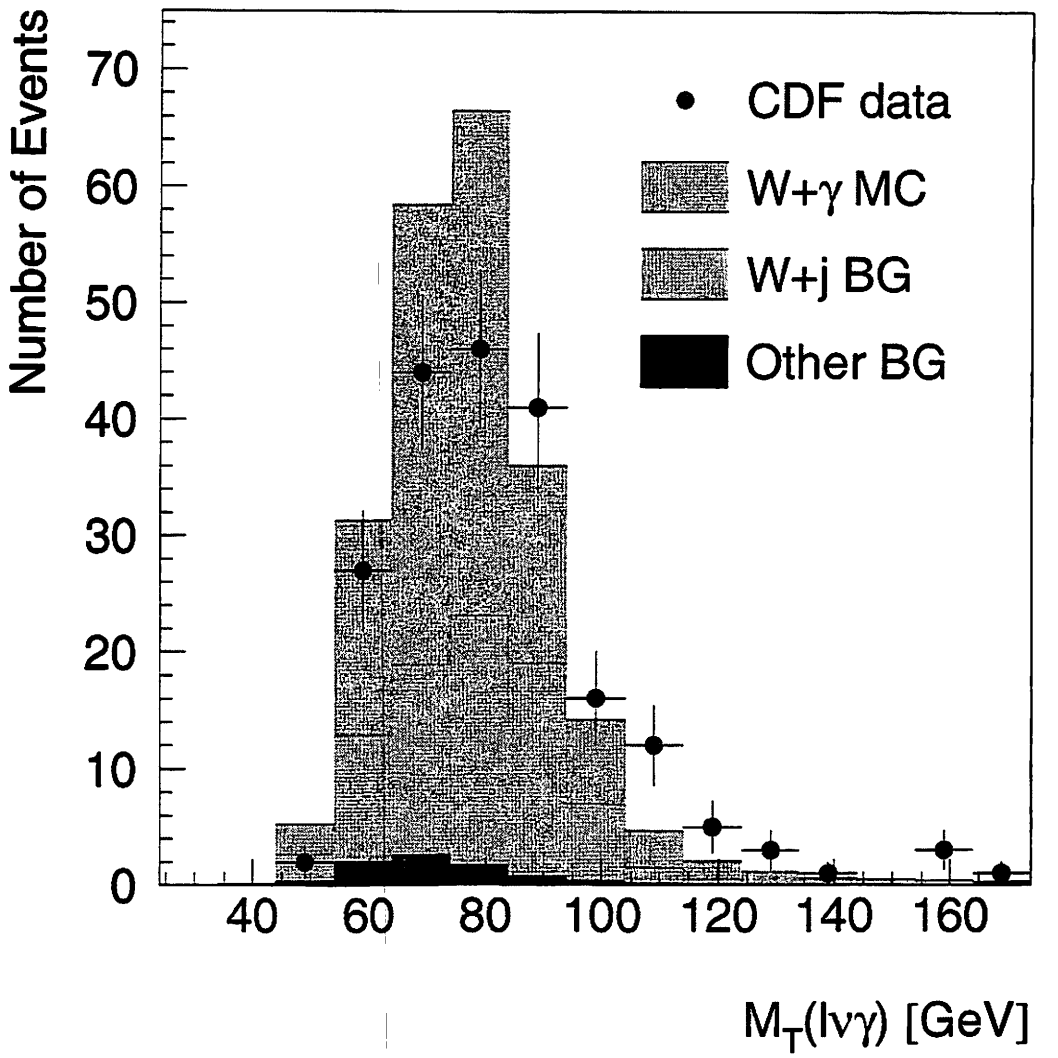

Figure 4.4: 3-body transverse mass ($M_{T\,l\nu\gamma}$) distribution.

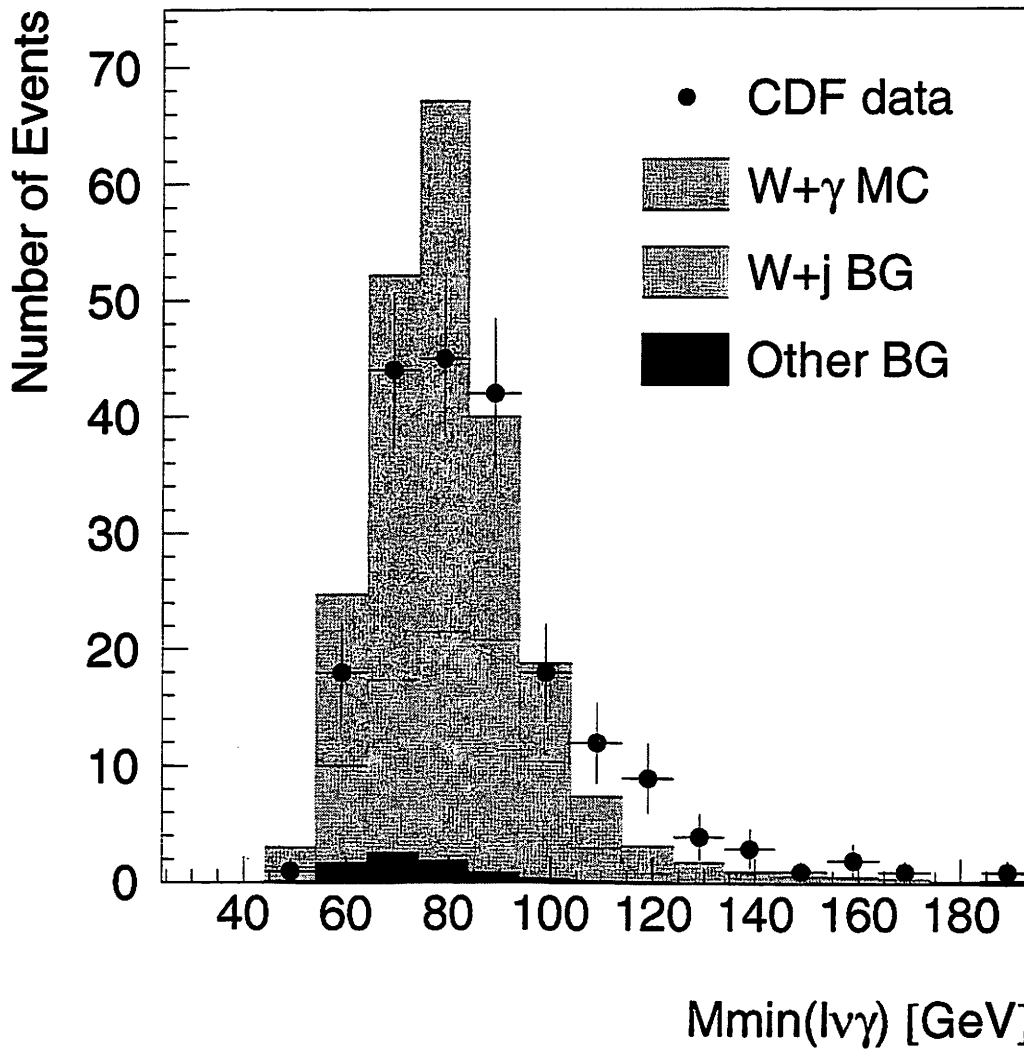

Figure 4.5: Wγ minimum invariant mass ($M_{min\ell\nu\gamma}$) distribution.

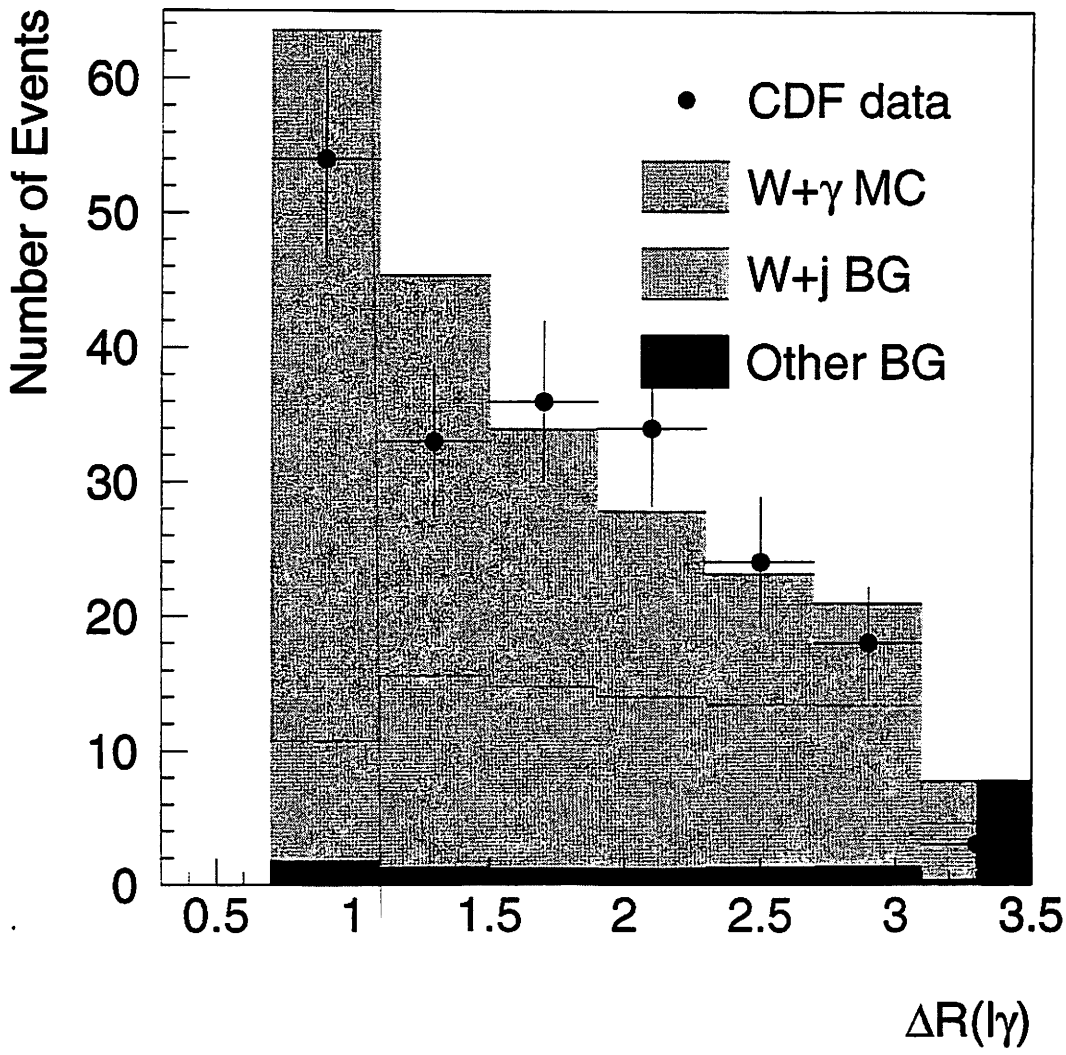

Figure 4.6: Angular separation ($\Delta R_{\ell\gamma}$) between the charged lepton from the W boson and the photon.

Chapter 5

Measuring the Photon Angular Distribution

Having obtained the Wγ inclusive samples as described in the previous chapter, we now turn our attention to the measurement of the photon angular distribution. The procedure itself is straightforward but there are a couple of technical difficulties:

- The radiative W decay process and the final state inner Bremsstrahlung process, Figure 1.1(b, c), do not contribute to the radiation amplitude zero in the Wγ production; Rather they tend to fill in the gap. Since their cross sections are considerably larger than the Wγ production processes, these events must be identified and removed.

- The neutrino four-momentum is needed to boost into the Wγ rest frame, but its z-component is not determined uniquely.

- We do not really know where the quark comes from; did it come from the proton or the antiproton? Since the angle θ^*_γ is defined with respect to the incident quark direction, it is impossible to unambiguously identify the proper direction.

- As discussed in the previous chapter, the most severe background for the Wγ final state is the W + *jets* events in which a jet is misidentified as a photon due to the much larger production cross section of the W + *jets* events. It is necessary to have a very good γ-*jet* discrimination factor to successfully identify the signal events.

We will address each of these issues in turn.

5.1 Wγ Production vs. Radiative Decay Events

The Feynman diagrams contributing to the radiation amplitude zero in the Wγ production are the three diagrams in Figure 1.1(a). The other two diagrams shown in Figure 1.1(b, c) are background events, which we refer to as "radiative decay processes" in this analysis. Since their cross sections are quite large, they must be removed as much as possible or our radiation ampliture zero would be washed away completely.

Although their final state particles are the same, their kinematics are not exactly the same. The photon in the radiative decay processes comes from the (on-shell) W boson or the decay lepton, which comes from the W boson, so the 3-body invariant

mass formed from the three final state particles is bounded to the mass of the W boson produced. The photon in the production processes on the other hand do not have such a constraint; The 2-body invariant mass formed from the charged lepton and the neutrino is bounded to the mass of the W boson, so adding the photon would make the mass larger. There are some grey zones because of the finite W decay width but the separation is fairly good.

Figure 5.1 shows the Baur Monte Carlo event simulation of Wγ events using all five Feynman diagrams in Figure 1.1. The abscissa is the generated 3-body invariant mass and the ordinate is the generated 2-body invariant mass. Two characteristic bands are clearly visible in the plot. The band with $M(\ell,\nu) \approx M_W$ is considered to be the production process and the other band with $M(\ell,\nu,\gamma) \approx M_W$ is considered to be the radiative decay processes. The overlap of the two bands is fairly small and the two processes can be separated well although there remain some events at the tails of the W mass Breit-Wigner distribution that cannot be assigned to either process.

In practice we do not know the exact mass of the W bosons involved in the process or the z-component of the neutrino momenta, so it is impossible to find either $M(\ell,\nu)$ or $M(\ell,\nu,\gamma)$ precisely. Most of the time however one of these two masses is very close to M_W, so if we constrain the invariant mass of the $\ell\nu$ or $\ell\nu\gamma$ system to the W mass and solve the two equations for $P_Z(\nu)$, we expect one of the four solutions (two possible solutions from two mass constraints) to be fairly close to the true value; We however do not know which of the four it is.

5.2 Removing the Radiative Decay Events

Since we have an extra photon in the Wγ production processes, their invariant mass is usually larger than the mass of the W boson. In other words, most of the production events have no answers to the constraint

$$M(\ell, \nu, \gamma) = M_W. \tag{5.1}$$

Most of the radiative decay events on the other hand do satisfy the constraint in Eq. 5.1 and any event that *are* found to satisfy the constraint are removed from the sample as possible radiative decay background. Appendix A discusses the mass constraint cuts in more detail.

5.3 Determination of the Wγ Rest Frame

To boost into the Wγ rest frame, we need all the four-momenta of the final state particles. The charged lepton and the photon are fully detected but we have limited information about the neutrino. The x- and y-components of the neutrino momentum are measured as $\vec{\not{E}}_T$ of the event, but the z-component cannot be "measured" in a similar manner, since initial parton momenta in $p\bar{p}$ collisions do not normally balance in the beam direction.

We therefore introduce a second constraint

$$\mathrm{M}(\ell,\nu) = \mathrm{M_W}. \tag{5.2}$$

which results in two possible answers to $\mathrm{P_Z}(\nu)$, as described in Section 5.2. The problem then is which of the two solutions to take. (Unlike the case with the radiative decay events, which are discarded once identified, we are actually interested in these solutions.[1]) Ref. [18] suggests that we always take one of the two solutions which is on average more probable in view of helicity conservation:

$$\mathrm{P_Z} = \begin{cases} \min(\mathrm{P_{Z_1}}, \mathrm{P_{Z_2}}) & \text{for } W^-\gamma, \\ \max(\mathrm{P_{Z_1}}, \mathrm{P_{Z_2}}) & \text{for } W^+\gamma. \end{cases} \tag{5.3}$$

where $\mathrm{P_{Z_1}}$ and $\mathrm{P_{Z_2}}$ are the two solutions. Note that the positive z-axis is defined along the proton direction. Taking the larger of the two $\mathrm{P_Z}$ solutions for $\mathrm{W^+\gamma}$ is based on the fact that ν tends to be emitted in the proton direction (cf. Figure 5.2).

Figure 5.3 compares the two photon angular distributions calculated at $\sqrt{s} = 1.8$ TeV: one obtained from the $\mathrm{P_Z}$ defined in Eq. 5.3, and the other using the solution not selected in Eq. 5.3. The difference between the two distributions in sensitivity to the radiation amplitude zero is evident. Using the Baur Monte Carlo event generator we find that Eq. 5.3 selects the correct solution about 70% of the time.

[1]Those events that fail the constraint (Eq. 5.2) are discarded in this analysis.

We use the neutrino P_Z defined in Eq. 5.3 to boost into the Wγ rest frame.

5.4 Definition of $\cos\theta^*_\gamma$

Another difficulty arises from our limited knowledge of the incident particle direction. The angle θ^*_γ is defined with respect to the incident quark, so it is impossible to unambiguously identify the proper direction without knowing the initial quarks involved in the collision. In $p\bar{p}$ collisions at Tevatron energies the contribution from valence quarks is dominant in the W production, so we can simply assume that the quark comes from the proton. However, the quark and the proton directions may not match exactly due to initial state Bremsstrahlung off the quark line, which induces non-zero P_T distribution to the Wγ system. The quark and the antiquark are no longer collinear in this case. To minimise this effect, we define our z-axis using both the quark and antiquark directions: The z-axis of the Collins-Soper reference frame [7] illustrated in Figure 5.4 is defined as the axis that bisects the angle between these two directions in the Wγ rest frame:

$$\vec{z} \equiv \frac{\vec{P}}{|\vec{P}|} - \frac{\vec{Q}}{|\vec{Q}|}, \tag{5.4}$$

where $\vec{P}$ and $\vec{Q}$ are the vectors $(0, 0, \pm 1)_{lab}$ boosted into the Wγ rest frame.

One more subtlety is that the radiation amplitude zero occurs at different positions depending on the charge of the quark involved; that is, according to Eq. 1.8, it occurs

Template	D	Significance Level	
SM+BG	0.0859	80.3%	
flat+BG	0.115	44.7%	(0.13 σ)
flat	0.126	33.6%	(0.42 σ)
BG only	0.190	3.6%	(1.80 σ)

Table 5.1: Results of Kolmogorov-Smirnov Test with four template distributions.

at $\cos\theta^*_\gamma = \mp\frac{1}{3}$ for the $W^\pm\gamma$ production. To account for this we multiply the $\cos\theta^*_\gamma$ by the charge factor $-Q_\ell$.

5.5 Measuring the Photon Angular Distribution

The photon angular distributions are presented in this section. Figure 5.5 shows the angular distribution using the 202 Wγ candidate events. Many radiative decay processes are still present and there is little trail of the radiation amplitude zero.

When radiative decay processes are suppressed by constraining the mass of the three final state particles to the W boson mass as discussed in Section 5.2, the distribution changes to Figure 5.6. The number of events drops to 75, but it is still unclear where the zero is.

We then tighten the angular separation $\Delta R_{\ell\gamma}$ between the charged lepton and the photon; as we increase the threshold, a dip consistent with the radiation amplitude zero is revealed. Figure 5.7 shows the distributions with $\Delta R_{\ell\gamma}$ thresholds between 0.7 and 1.5; with $\Delta R_{\ell\gamma} > 1.5$, the number of events drops to 56 events (Figure 5.8).

A Kolmogorov-Smirnov test (see Appendix B) is applied to the photon angular

distribution with $\Delta R_{\ell\gamma} > 1.5$ to see how consistent the shape of the distribution is with the expectations from the Standard Model, the flat signal distribution[2] background-only, and flat distributions. Figure 5.9 shows the cumulative distributions, with four template distributions: SM+BG, BG-only, flat, and flat+BG distributions. The Kolmogorov static D is computed in each case and significance levels are evaluated.

It is clear that the background distribution alone is not suited to describe the observed angular distribution, by just considering the difference between the number of events expected and that of events observed. Even if we neglect this large difference in the yields, we can reject it at the 96% level, by applying KS test, which corresponds to a Gaussian sigma of 1.80. The assumption that the observed distribution is flat is disfavoured at the 66% level (0.42σ).

The CDF data are consistent with the Standard Model predictions (SM+BG) at the significance level of 80% and the flat signal distribution assumption on the other hand is only applicable at the 44% level, hinting presence of a radiation amplitude zero.

[2]Flat+BG distribution is made by adding as much flat signal distribution on top of BG distribution as to make the number of events equal to SM+BG distribution.

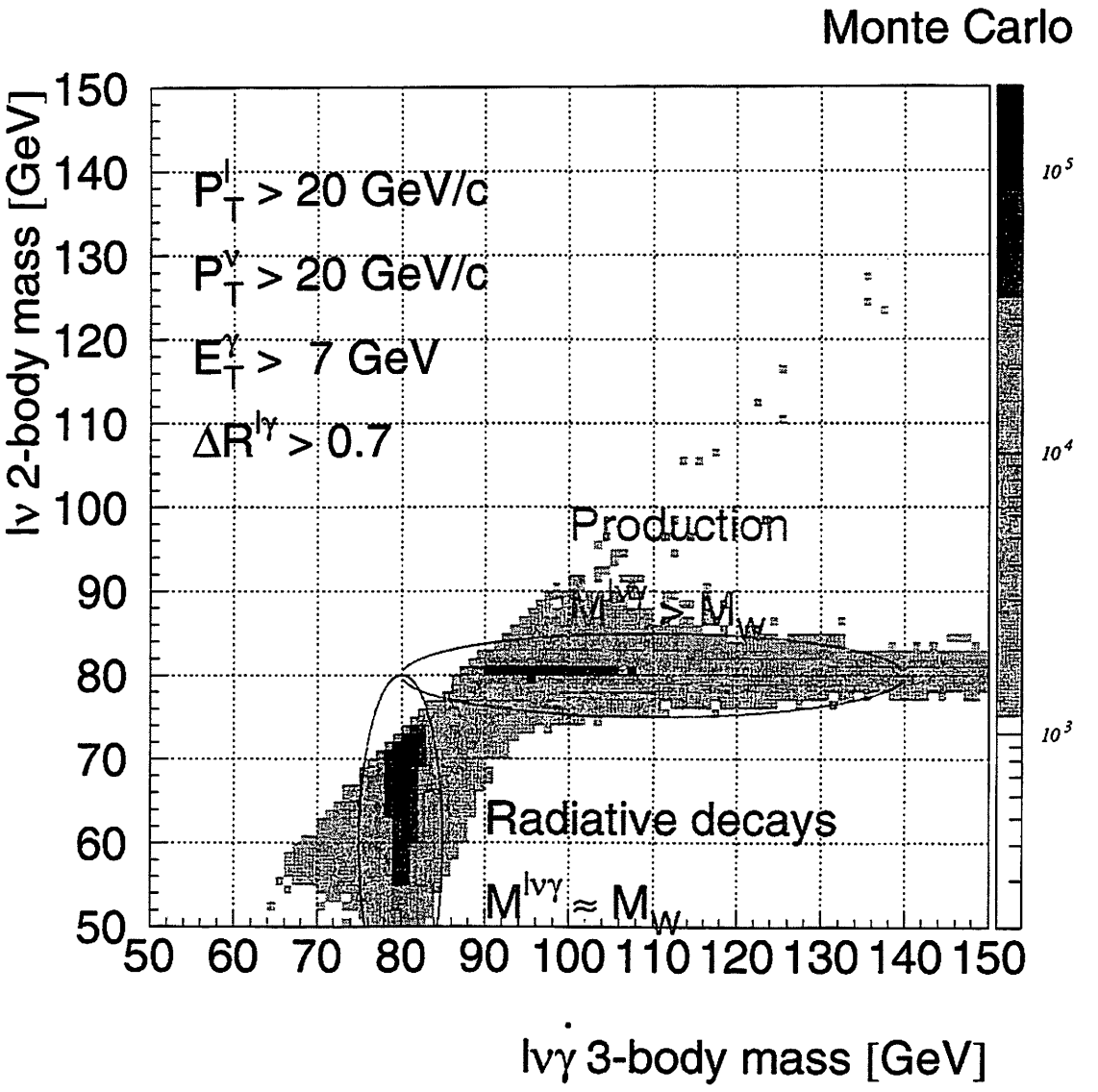

Figure 5.1: Two-body vs. three-body invariant masses using Baur MC. All five diagrams in Figure 1.1 are included.

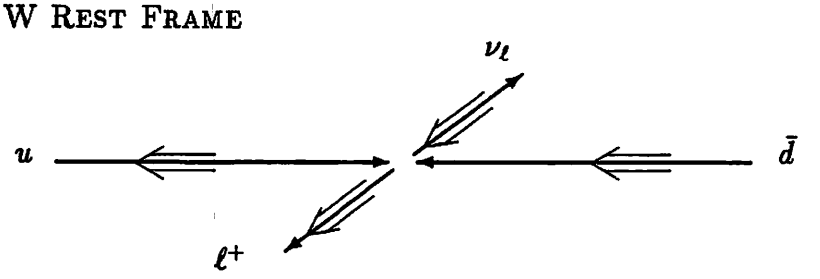

Figure 5.2: Subprocess for $W^+ \to \ell^+ \nu$ in W rest frame. Arrows denote momenta and double arrows denote helicities. ν_ℓ tends to be emitted in the u-quark's direction.

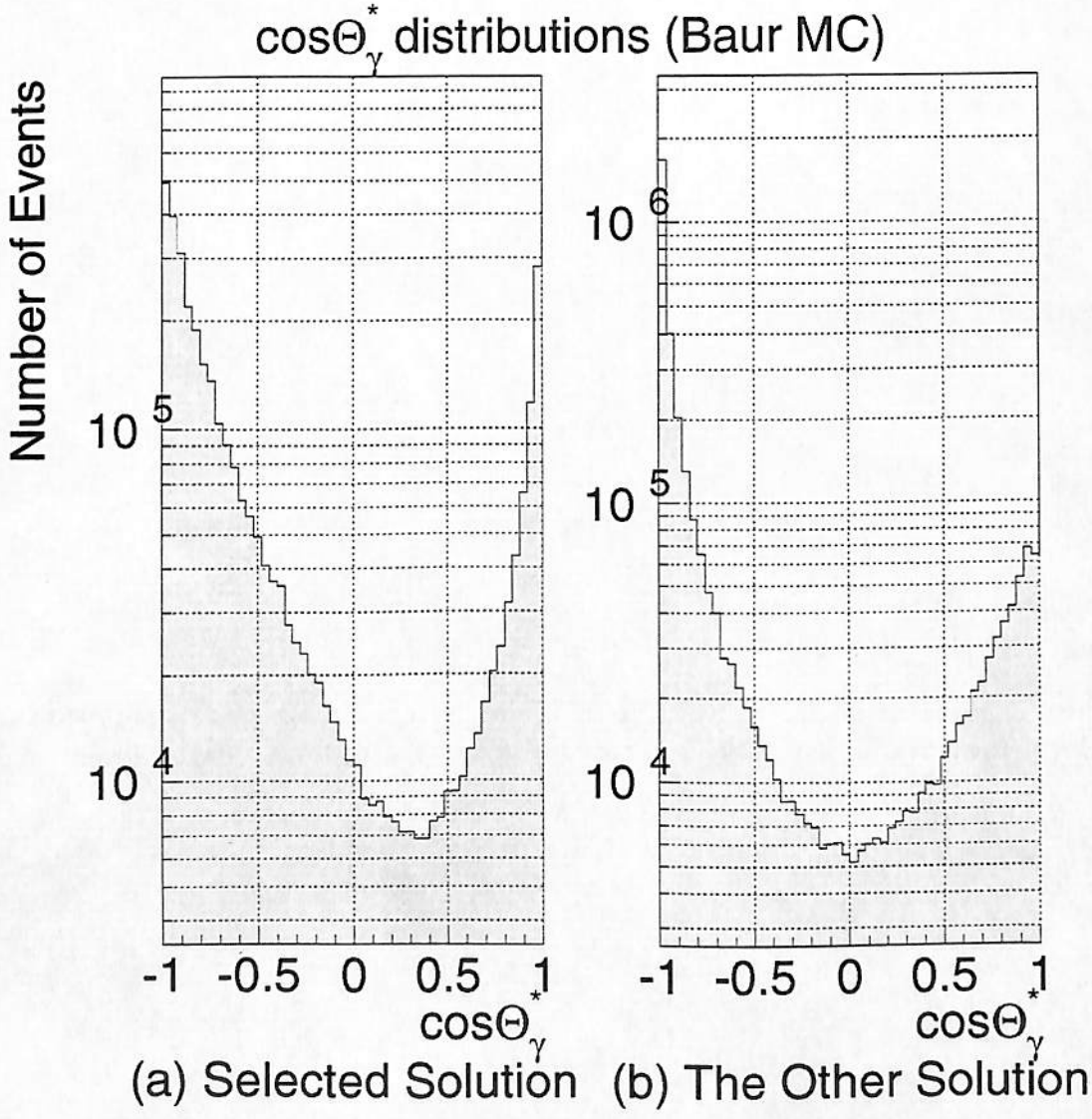

Figure 5.3: Comparison of the two photon angular distributions to verify the validity of Eq. 5.3. (a) The solution selected in Eq. 5.3 is used; (b) The other solution is used. The difference in sensitivity to the RAZ is evident.

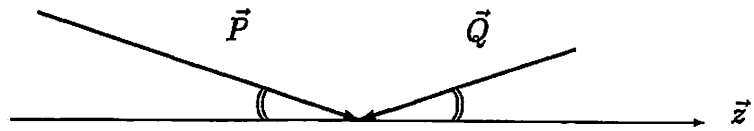

Figure 5.4: Illustration of the z-axis in the Collins-Soper reference frame. The axis is defined so as to bisect the two vectors $\vec{P}$ and $-\vec{Q}$.

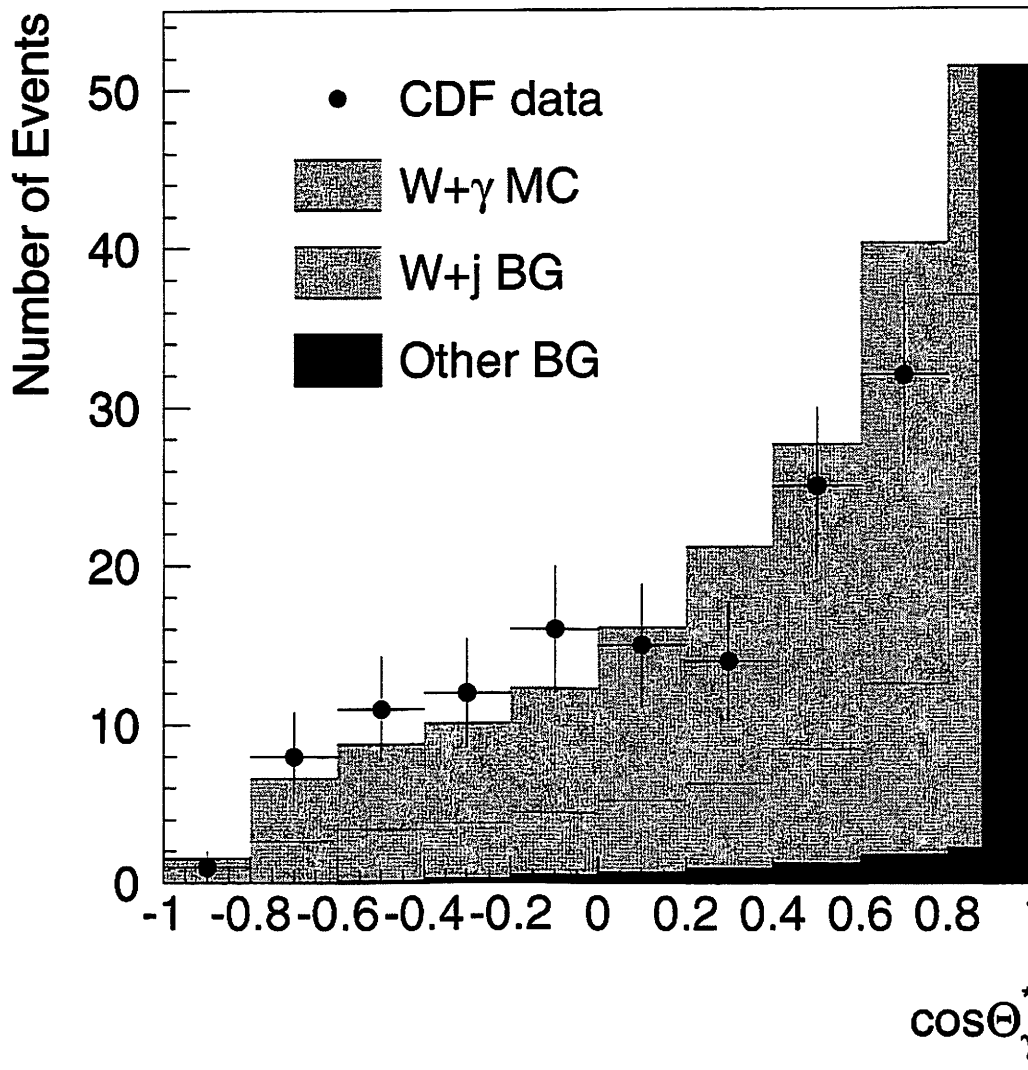

Figure 5.5: Photon angular distribution of the 202 Wγ candidate events.

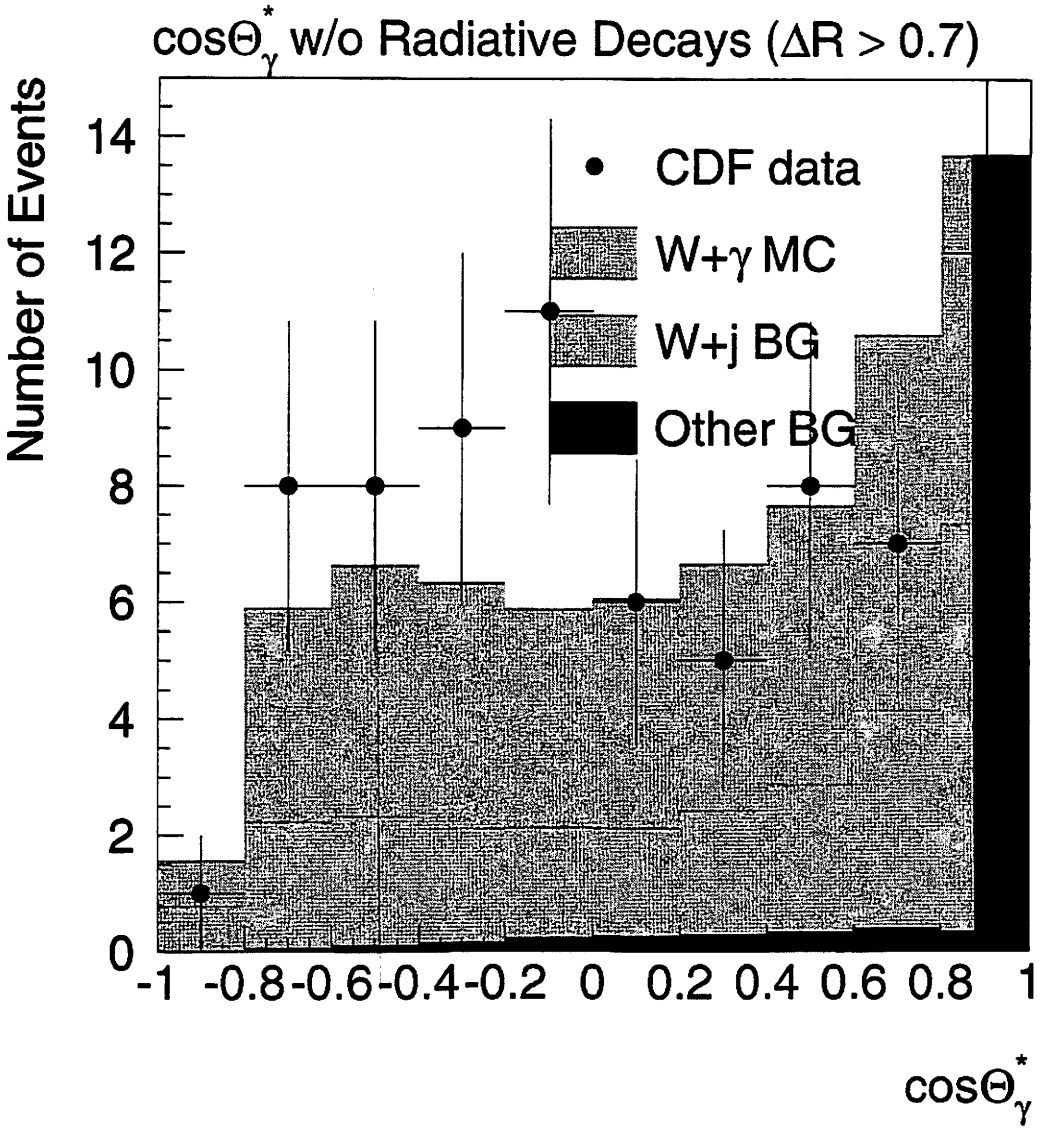

Figure 5.6: Photon angular distribution after the radiative decay events are removed as discussed in Sec. 5.2.

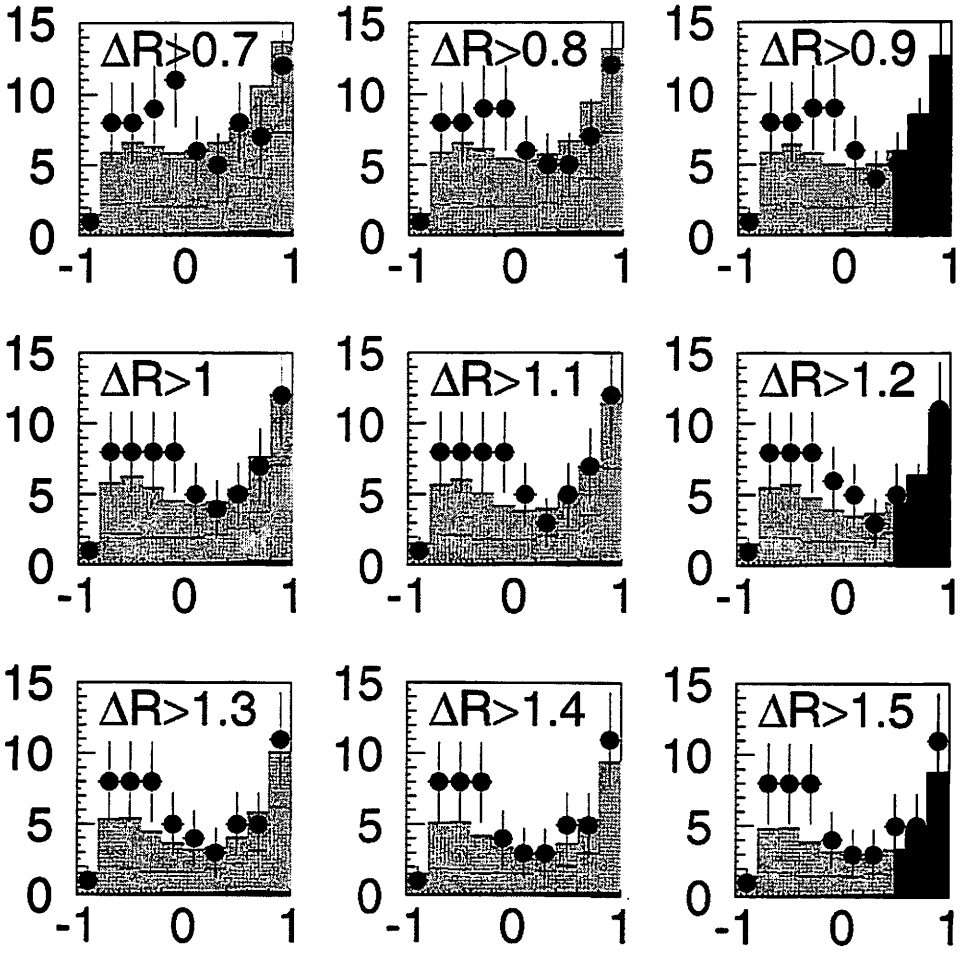

Figure 5.7: Photon angular distributions. ΔR threshold is varied between 0.7 and 1.5; As we raise the threshold we see a clear view of the RAZ.

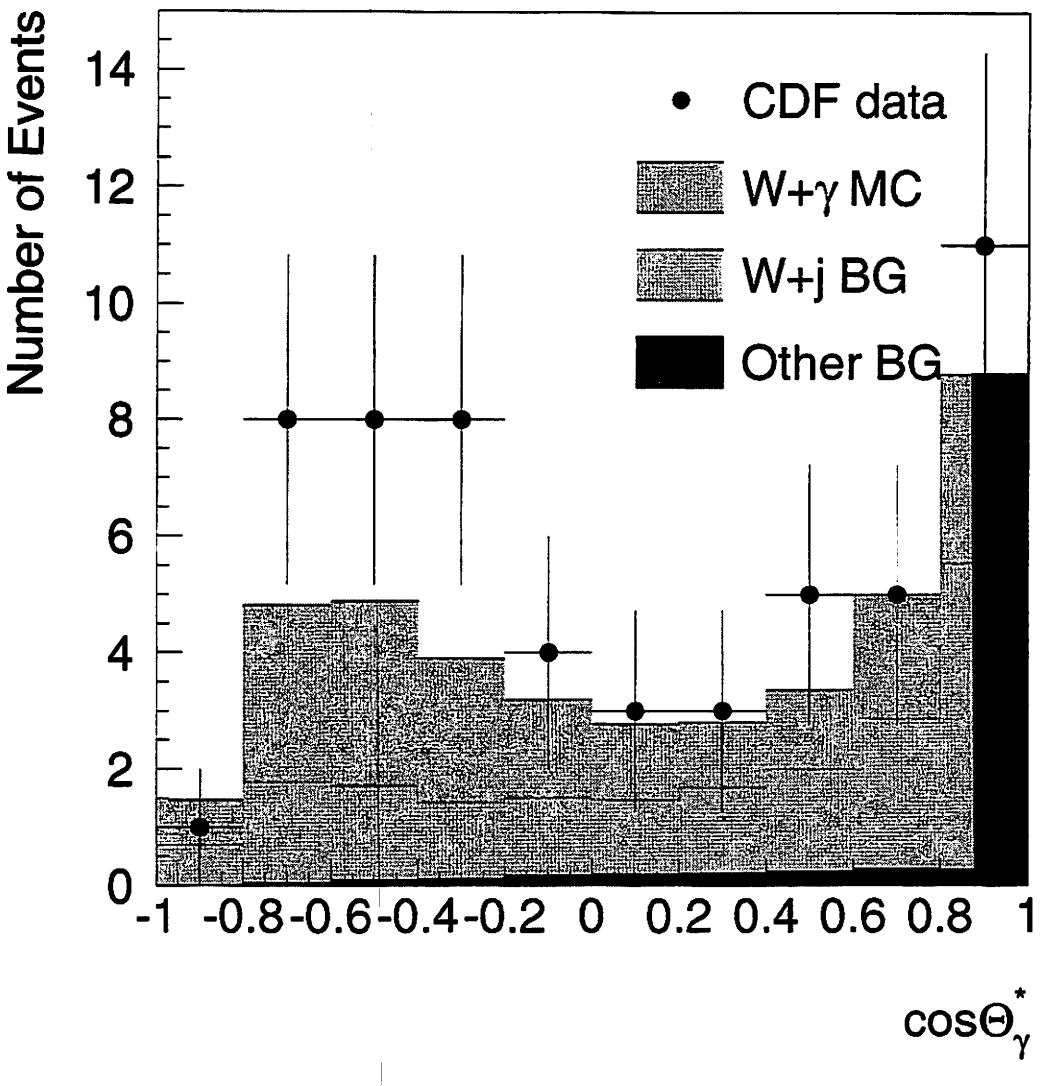

Figure 5.8: Photon angular distribution after the radiative decay events are removed as discussed in Sec. 5.2. ($\Delta R > 1.5$)

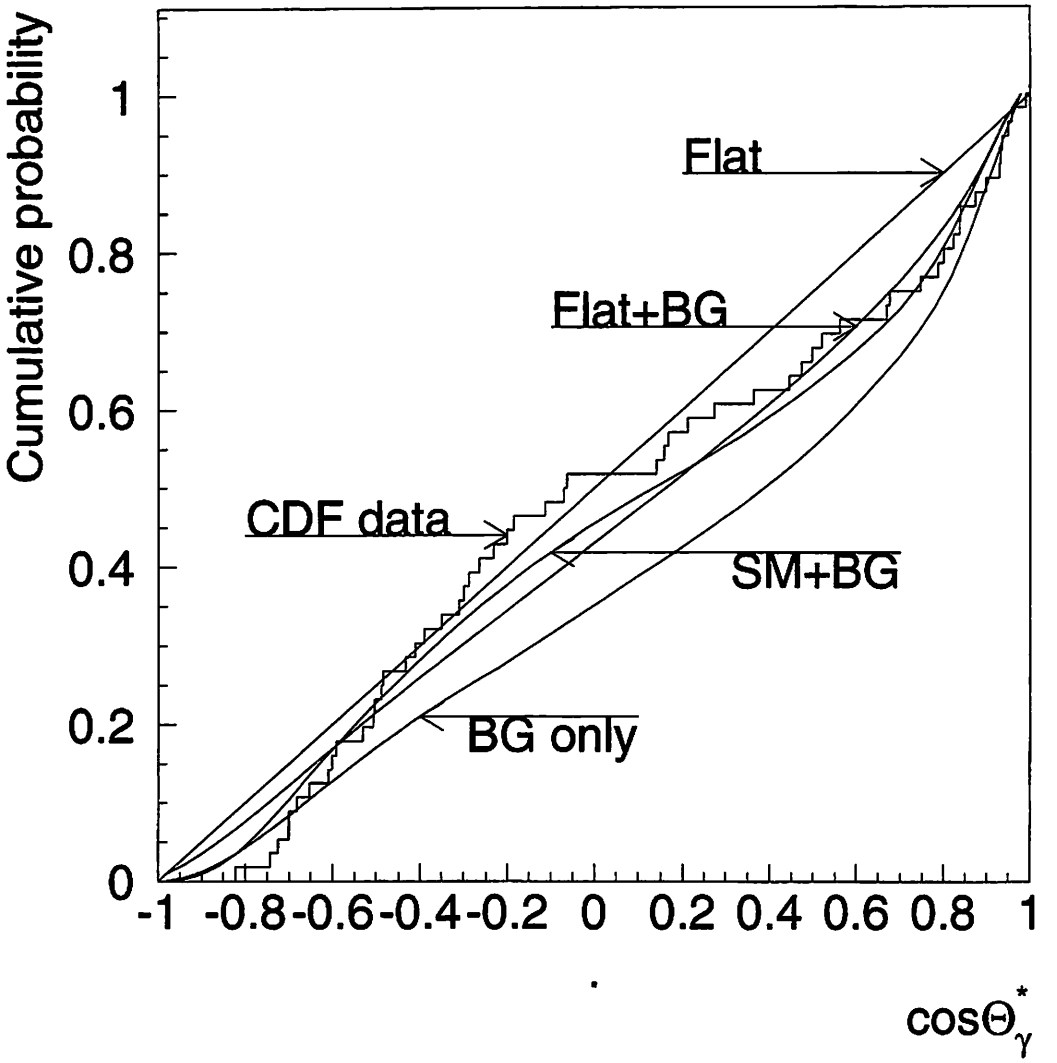

Figure 5.9: Photon angular distribution (Figure 5.8) expressed as a cumulative distribution, used for Kolmogorov-Smirnov Test. Four template curves are also drawn: flat, flat+BG, SM+BG, and BG-only distributions.

Chapter 6

Conclusions

The photon angular distribution is measured for the first time in the Wγ production in $p\bar{p}$ collisions at $\sqrt{s} = 1.8$ TeV. The data corresponding to an integrated luminosity of 110 pb^{-1} were collected with the CDF detector during Run I from 1992 to 1995.

A total of 202 Wγ events were extracted from high P_T electron and muon samples with $P_{T_\gamma} > 7.0$ GeV and $\Delta R_{\ell\gamma} > 0.7$.

By constraining the (ℓ,ν,γ) system to the W boson, we removed most of the radiative decay background events in the 202 event sample. We reconstructed the z-component of the neutrino momentum for the 75 remaining events by applying another mass constraint, this time with (ℓ,ν) system bounded to the W boson, and by always choosing one of the two possible solutions that is favoured by helicity conservation. We then boosted the Wγ system into its rest frame and obtained the photon angular distribution with respect to the z-axis defined in the Collins-Soper

frame, which minimises the effect of finite P_T (Wγ).

As we raised the cut in $\Delta R_{\ell\gamma}$ from 0.7 to 1.5, the number of candidate events dropped gradually to 56 events, and an angular distribution consistent with the radiation amplitude zero (RAZ) was revealed.

The Baur LO Monte Carlo generator was used to estimate the Standard Model predictions in the angular distribution. As possible background events, we considered W + *jets* events where a jet is misidentified as a photon and 1-legged Z events as well as Wγ events with the W decaying in the τ channel.

A Kolmogorov-Smirnov test was applied to obtain the significance levels of the data with theoretical predictions including background contributions and with the flat signal hypothesis, where the Baur Monte Carlo events were replaced with a simple flat distribution with no RAZ. The data were found to be consistent with the Standard Model predictions at the 80% significance level, with the flat signal distribution only at the 44% level, implying presence of a radiation amplitude zero around $\cos\theta^*_\gamma = \pm\frac{1}{3}$, as expected by the Standard Model.

Appendix A

Mass Constraint Cuts

In this appendix, we clarify what we mean by mass constraint cuts in Eqs. 5.1 and 5.2.

We constrain the invariant mass of the $\ell\nu$ system to the W mass M_W using the relation:

$$M_W^2 = (E_\ell + E_\nu)^2 - (\vec{p}_\ell + \vec{p}_\nu)^2 \quad \text{(A.1)}$$

$$= 2E_\ell\sqrt{\not{E}_T^{\,2} + x^2} - 2\vec{P}_{T\ell} \cdot \vec{\not{E}}_T - 2P_{Z\ell}x + m_\ell^2, \quad \text{(A.2)}$$

and similarly for the $\ell\nu\gamma$ system:

$$M_W^2 = (E_\ell + E_\nu + E_\gamma)^2 - (\vec{p}_\ell + \vec{p}_\nu + \vec{p}_\gamma)^2 \quad \text{(A.3)}$$

$$= (E_{\ell+\gamma} + E_\nu)^2 - (\vec{p}_{\ell+\gamma} + \vec{p}_\nu)^2 \quad \text{(A.4)}$$

$$= 2E_{\ell+\gamma}\sqrt{\not{E}_T^{\,2} + x^2} - 2\vec{P}_{T\ell+\gamma} \cdot \vec{\not{E}}_T - 2P_{Z\ell+\gamma}x + m_{\ell+\gamma}^2, \quad \text{(A.5)}$$

with unknown $x = P_{Z_\nu}$. It is simple enough to solve these equations for x and get two solutions in each case, but let us take some time and see when we have solutions to these equations.

We can use Eqs. A.2 and A.5 to compute the invariant mass of the $\ell\nu$ or $\ell\nu\gamma$ system with given P_{Z_ν}. Figure A.1 shows how the invariant mass of a particular event changes with the neutrino's P_Z as a free parameter. It is a simple parabolic curve as a function of the difference in rapidity between the charged lepton (or the vector sum of the charged lepton and the photon for Eq. A.5) and the neutrino. If the parabola intersects with $y = M_W$ we have an answer (well, two answers, in fact); if the curve lies above the line we have no answers, which means the event cannot be constrained to that mass. The invariant mass is minimum when the photon's rapidity equals the charged lepton's rapidity (or that of the vector sum), that is, when the opening angle between the two is minimum. The mass constraint cuts used in Chapter 5 are therefore equivalent to cuts on the minimum invariant mass of the two or three particles.

Finding events that satisfy Eq. 5.1 is equivalent to selecting those events which have their minimum invariant mass larger than the W mass:

$$M_{min\ell\nu\gamma} > M_W \quad \text{(Production)} \tag{A.6}$$

$$M_{min\ell\nu\gamma} \leq M_W \quad \text{(Radiative Decay).} \tag{A.7}$$

For Eq. 5.2,

$$M_{min\ell\nu} \leq M_W \quad \text{(Has solutions to } P_{Z\nu}\text{)} \tag{A.8}$$

$$M_{min\ell\nu} > M_W \quad \text{(No solutions. Event discarded).} \tag{A.9}$$

If we ignore m_ℓ, $M_{min\ell\nu}$ reduces to $M_{T\ell\nu}$.

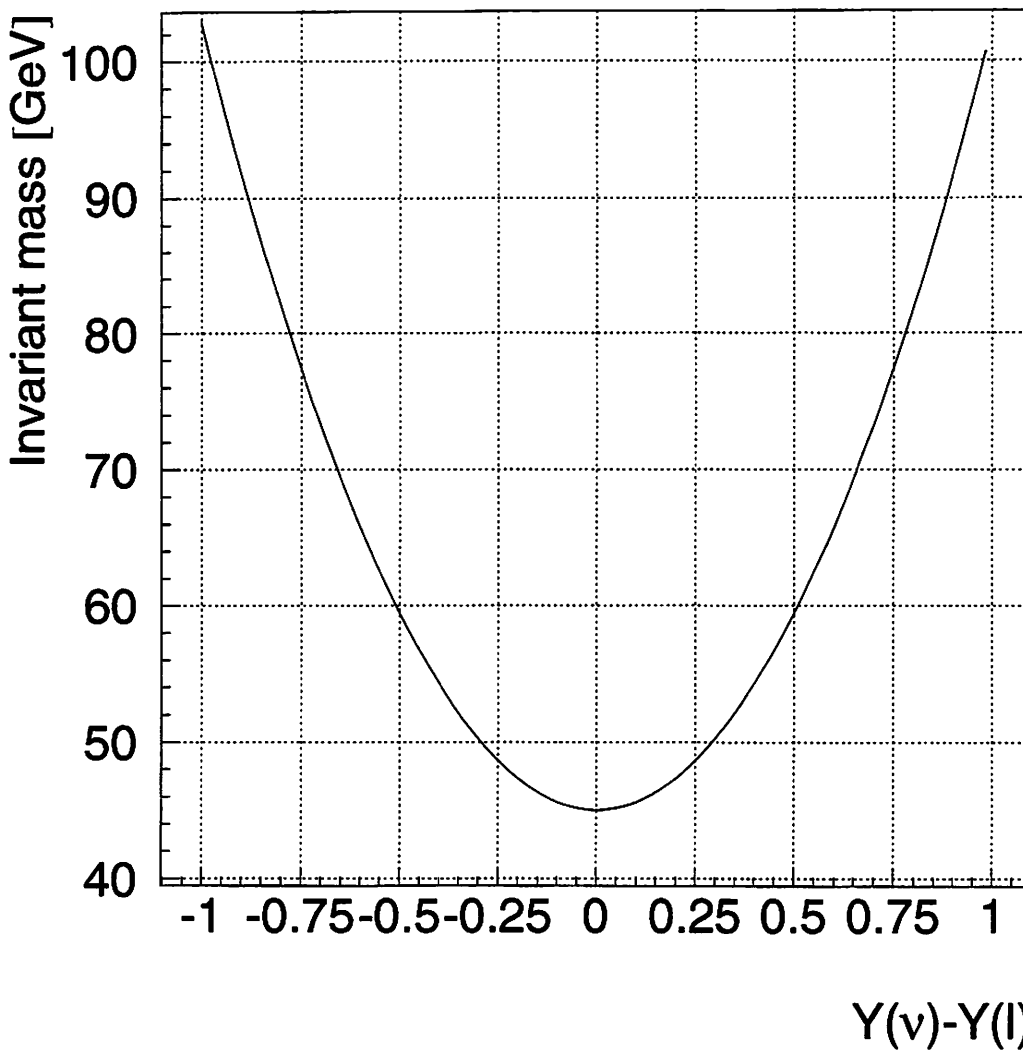

Figure A.1: Invariant mass of a ℓ-ν pair formed by varying $P_Z(\nu)$ as a free parameter. The abscissa is the difference in rapidity, $Y(\nu) - Y(\ell)$. The mass is minimum when the difference is zero. If we constrain the mass to be 80 GeV, we have $Y(\nu) = Y(\ell) \pm 0.78$ for this particular event.

Appendix B

Kolmogorov-Smirnov Test

The Kolmogorov-Smirnov Test (or K-S Test for short) [17] is often applied to see if two distributions are different; that is, to see if we can disprove the null hypothesis that they are drawn from the same population distribution function.

In the K-S Test the two distributions to be compared are first converted into two cumulative probability distributions. Different distribution functions give different cumulative probability distributions. They all agree at end points, however. That is, at the smallest value of x every cumulative distribution is zero; and at the largest value of x it is always unity. In other words, it is the behaviour between these two end points that distinguishes distributions. What makes the K-S Test ideal for comparing (low statistics) empirical distributions and theoretical curves is that it is applicable to unbinned distributions.

The Kolmogorov-Smirnov D is a simple statistic to measure the overall difference

between two cumulative distributions: It is defined as the maximum value of the absolute difference between two cumulative distributions. Thus, for comparing one data set to a known distribution the K-S statistic is

$$D = \max_{-\infty<x<+\infty} |S_N(x) - P(x)|, \tag{B.1}$$

where $S_N(x)$ and $P(x)$ denote the cumulative probability distribution of the data set and that of the known distribution.

Since these distributions are monotonically increasing, D reduces to

$$D = \max(D_1, \ldots, D_N), \tag{B.2}$$

where

$$D_i = \max(|S_N(x_i) - P(x_i)|, |S_N(x_{i-1}) - P(x_i)|). \tag{B.3}$$

Note

$$S_N(x_i) = \frac{i}{N} \tag{B.4}$$

regardless of where x_is are.

The value D is essentially a random variable but its distribution, when used in the context of null hypothesis, has been well studied. For large N, Kolmogorov found the limit distribution

$$Q_{KS}(\lambda) = 2\sum_{i=1}^{\infty}(-1)^{i-1}e^{-2i^2\lambda^2}, \tag{B.5}$$

where $\lambda = \sqrt{N}D$. Given λ, this function returns the probability that the two distributions are compatible. In practice, $N = 10 \sim 20$ is large enough.

Appendix C

The CDF Collaboration

F. Abe,[15] H. Akimoto,[34] A. Akopian,[29] M. G. Albrow,[7] S. R. Amendolia,[25] D. Amidei,[18] J. Antos,[31] C. Anway-Wiese,[4] S. Aota,[34] G. Apollinari,[29] T. Asakawa,[34] W. Ashmanskas,[16] M. Atac,[7] F. Azfar,[24] P. Azzi-Bacchetta,[23] N. Bacchetta,[23] W. Badgett,[18] S. Bagdasarov,[29] M. W. Bailey,[20] J. Bao,[37] P. de Barbaro,[28] A. Barbaro-Galtieri,[16] V. E. Barnes,[27] B. A. Barnett,[14] M. Barone,[25] E. Barzi,[8] G. Bauer,[17] T. Baumann,[10] F. Bedeschi,[25] S. Behrends,[3] S. Belforte,[25] G. Bellettini,[25] J. Bellinger,[36] D. Benjamin,[33] J. Benlloch,[17] J. Bensinger,[3] D. Benton,[24] A. Beretvas,[7] J. P. Berge,[7] J. Berryhill,[5] S. Bertolucci,[8] B. Bevensee,[24] A. Bhatti,[29] K. Biery,[13] M. Binkley,[7] D. Bisello,[23] R. E. Blair,[1] C. Blocker,[3] A. Bodek,[28] W. Bokhari,[17] V. Bolognesi,[2] G. Bolla,[23] D. Bortoletto,[27] J. Boudreau,[26] L. Breccia,[2] C. Bromberg,[19] N. Bruner,[20] E. Buckley-Geer,[7] H. S. Budd,[28] K. Burkett,[18] G. Busetto,[23] A. Byon-

Wagner,[7] K. L. Byrum,[1] J. Cammerata,[14] C. Campagnari,[7] M. Campbell,[18] A. Caner,[25] W. Carithers,[16] D. Carlsmith,[36] A. Castro,[23] D. Cauz,[25] Y. Cen,[28] F. Cervelli,[25] P. S. Chang,[31] P. T. Chang,[31] H. Y. Chao,[31] J. Chapman,[18] M. -T. Cheng,[31] G. Chiarelli,[25] T. Chikamatsu,[34] C. N. Chiou,[31] L. Christofek,[12] S. Cihangir,[7] A. G. Clark,[9] M. Cobal,[25] E. Cocca,[25] M. Contreras,[5] J. Conway,[30] J. Cooper,[7] M. Cordelli,[8] C. Couyoumtzelis,[9] D. Crane,[1] D. Cronin-Hennessy,[6] R. Culbertson,[5] T. Daniels,[17] F. DeJongh,[7] S. Delchamps,[7] S. Dell'Agnello,[25] M. Dell'Orso,[25] R. Demina,[7] L. Demortier,[29] M. Deninno,[2] P. F. Derwent,[7] T. Devlin,[30] J. R. Dittmann,[6] S. Donati,[25] J. Done,[32] T. Dorigo,[23] A. Dunn,[18] N. Eddy,[18] K. Einsweiler,[16] J. E. Elias,[7] R. Ely,[16] E. Engels, Jr.,[26] D. Errede,[12] S. Errede,[12] Q. Fan,[27] C. Ferretti,[25] I. Fiori,[2] B. Flaugher,[7] G. W. Foster,[7] M. Franklin,[10] M. Frautschi,[33] J. Freeman,[7] J. Friedman,[17] H. Frisch,[5] T. A. Fuess,[1] Y. Fukui,[15] S. Funaki,[34] S. Galeotti,[25] M. Gallinaro,[23] M. Garcia-Sciveres,[16] A. F. Garfinkel,[27] C. Gay,[10] S. Geer,[7] D. W. Gerdes,[14] P. Giannetti,[25] N. Giokaris,[29] P. Giromini,[8] G. Giusti,[25] L. Gladney,[24] D. Glenzinski,[14] M. Gold,[20] J. Gonzalez,[24] A. Gordon,[10] A. T. Goshaw,[6] Y. Gotra,[25] K. Goulianos,[29] H. Grassmann,[25] L. Groer,[30] C. Grosso-Pilcher,[5] G. Guillian,[18] R. S. Guo,[31] C. Haber,[16] E. Hafen,[17] S. R. Hahn,[7] R. Hamilton,[10] R. Handler,[36] R. M. Hans,[37] F. Happacher,[25] K. Hara,[34] A. D. Hardman,[27] B. Harral,[24] R. M. Harris,[7] S. A. Hauger,[6] J. Hauser,[4] C. Hawk,[30] E. Hayashi,[34] J. Heinrich,[24] K. D. Hoffman,[27] M. Hohlmann,[5] C. Holck,[24] R. Hollebeek,[24] L. Holloway,[12] A. Hölscher,[13] S. Hong,[18] G. Houk,[24] P. Hu,[26]

B. T. Huffman,[26] R. Hughes,[21] J. Huston,[19] J. Huth,[10] J. Hylen,[7] H. Ikeda,[34] M. Incagli,[25] J. Incandela,[7] G. Introzzi,[25] J. Iwai,[34] Y. Iwata,[11] H. Jensen,[7] U. Joshi,[7] R. W. Kadel,[16] E. Kajfasz,[23] H. Kambara,[9] T. Kamon,[32] T. Kaneko,[34] K. Karr,[35] H. Kasha,[37] Y. Kato,[22] T. A. Keaffaber,[27] L. Keeble,[8] K. Kelley,[17] R. D. Kennedy,[30] R. Kephart,[7] P. Kesten,[16] D. Kestenbaum,[10] R. M. Keup,[12] H. Keutelian,[7] F. Keyvan,[4] B. Kharadia,[12] B. J. Kim,[28] D. H. Kim,[7a] H. S. Kim,[13] S. B. Kim,[18] S. H. Kim,[34] Y. K. Kim,[16] L. Kirsch,[3] P. Koehn,[28] K. Kondo,[34] J. Konigsberg,[10] S. Kopp,[5] K. Kordas,[13] A. Korytov,[17] W. Koska,[7] E. Kovacs,[7a] W. Kowald,[6] M. Krasberg,[18] J. Kroll,[7] M. Kruse,[28] T. Kuwabara,[34] S. E. Kuhlmann,[1] E. Kuns,[30] A. T. Laasanen,[27] S. Lammel,[7] J. I. Lamoureux,[3] T. LeCompte,[1] S. Leone,[25] J. D. Lewis,[7] P. Limon,[7] M. Lindgren,[4] T. M. Liss,[12] N. Lockyer,[24] O. Long,[24] C. Loomis,[30] M. Loreti,[23] J. Lu,[32] D. Lucchesi,[25] P. Lukens,[7] S. Lusin,[36] J. Lys,[16] K. Maeshima,[7] A. Maghakian,[29] P. Maksimovic,[17] M. Mangano,[25] J. Mansour,[19] M. Mariotti,[23] J. P. Marriner,[7] A. Martin,[12] J. A. J. Matthews,[20] R. Mattingly,[17] P. McIntyre,[32] P. Melese,[29] A. Menzione,[25] E. Meschi,[25] S. Metzler,[24] C. Miao,[18] T. Miao,[7] G. Michail,[10] R. Miller,[19] H. Minato,[34] S. Miscetti,[8] M. Mishina,[15] H. Mitsushio,[34] T. Miyamoto,[34] S. Miyashita,[34] N. Moggi,[25] Y. Morita,[15] J. Mueller,[26] A. Mukherjee,[7] T. Muller,[4] P. Murat,[25] H. Nakada,[34] I. Nakano,[34] C. Nelson,[7] D. Neuberger,[4] C. Newman-Holmes,[7] C.-Y. Ngan,[17] M. Ninomiya,[34] L. Nodulman,[1] S. H. Oh,[6] K. E. Ohl,[37] T. Ohmoto,[11] T. Ohsugi,[11] R. Oishi,[34] M. Okabe,[34] T. Okusawa,[22] R. Oliveira,[24] J. Olsen,[36] C. Pagliarone,[2] R. Paoletti,[25] V. Papadimitriou,[33] S. P. Pappas,[37]

N. Parashar,[25] S. Park,[7] A. Parri,[8] J. Patrick,[7] G. Pauletta,[25] M. Paulini,[16] A. Perazzo,[25] L. Pescara,[23] M. D. Peters,[16] T. J. Phillips,[6] G. Piacentino,[2] M. Pillai,[28] K. T. Pitts,[7] R. Plunkett,[7] L. Pondrom,[36] J. Proudfoot,[1] F. Ptohos,[10] G. Punzi,[25] K. Ragan,[13] D. Reher,[16] A. Ribon,[23] F. Rimondi,[2] L. Ristori,[25] W. J. Robertson,[6] T. Rodrigo,[25] S. Rolli,[25] J. Romano,[5] L. Rosenson,[17] R. Roser,[12] W. K. Sakumoto,[28] D. Saltzberg,[5] A. Sansoni,[8] L. Santi,[25] H. Sato,[34] P. Schlabach,[7] E. E. Schmidt,[7] M. P. Schmidt,[37] A. Scribano,[25] S. Segler,[7] S. Seidel,[20] Y. Seiya,[34] G. Sganos,[13] M. D. Shapiro,[16] N. M. Shaw,[27] Q. Shen,[27] P. F. Shepard,[26] M. Shimojima,[34] M. Shochet,[5] J. Siegrist,[16] A. Sill,[33] P. Sinervo,[13] P. Singh,[26] J. Skarha,[14] K. Sliwa,[35] F. D. Snider,[14] T. Song,[18] J. Spalding,[7] T. Speer,[9] P. Sphicas,[17] F. Spinella,[25] M. Spiropulu,[10] L. Spiegel,[7] L. Stanco,[23] J. Steele,[36] A. Stefanini,[25] K. Strahl,[13] J. Strait,[7] R. Ströhmer,[7a] D. Stuart,[7] G. Sullivan,[5] A. Soumarokov,[31] K. Sumorok,[17] J. Suzuki,[34] T. Takada,[34] T. Takahashi,[22] T. Takano,[34] K. Takikawa,[34] N. Tamura,[11] B. Tannenbaum,[20] F. Tartarelli,[25] W. Taylor,[13] P. K. Teng,[31] Y. Teramoto,[22] S. Tether,[17] D. Theriot,[7] T. L. Thomas,[20] R. Thun,[18] M. Timko,[35] P. Tipton,[28] A. Titov,[29] S. Tkaczyk,[7] D. Toback,[5] K. Tollefson,[28] A. Tollestrup,[7] J. F. de Troconiz,[10] S. Truitt,[18] J. Tseng,[14] N. Turini,[25] T. Uchida,[34] N. Uemura,[34] F. Ukegawa,[24] G. Unal,[24] J. Valls,[7a] S. C. van den Brink,[26] S. Vejcik, III,[18] G. Velev,[25] R. Vidal,[7] M. Vondracek,[12] D. Vucinic,[17] R. G. Wagner,[1] R. L. Wagner,[7] J. Wahl,[5] N. B. Wallace,[25] A. M. Walsh,[30] C. Wang,[6] C. H. Wang,[31] J. Wang,[5] M. J. Wang,[31] Q. F. Wang,[29] A. Warburton,[13] T. Watts,[30] R. Webb,[32] C. Wei,[6] C. Wendt,[36]

H. Wenzel,[16] W. C. Wester, III,[7] A. B. Wicklund,[1] E. Wicklund,[7] R. Wilkinson,[24] H. H. Williams,[24] P. Wilson,[5] B. L. Winer,[21] D. Winn,[18] D. Wolinski,[18] J. Wolinski,[19] S. Worm,[20] X. Wu,[9] J. Wyss,[23] A. Yagil,[7] W. Yao,[16] K. Yasuoka,[34] Y. Ye,[13] G. P. Yeh,[7] P. Yeh,[31] M. Yin,[6] J. Yoh,[7] C. Yosef,[19] T. Yoshida,[22] D. Yovanovitch,[7] I. Yu,[7] L. Yu,[20] J. C. Yun,[7] A. Zanetti,[25] F. Zetti,[25] L. Zhang,[36] W. Zhang,[24] and S. Zucchelli[2]

[1] *Argonne National Laboratory, Argonne, Illinois 60439*

[2] *Istituto Nazionale di Fisica Nucleare, University of Bologna, I-40126 Bologna, Italy*

[3] *Brandeis University, Waltham, Massachusetts 02254*

[4] *University of California at Los Angeles, Los Angeles, California 90024*

[5] *University of Chicago, Chicago, Illinois 60637*

[6] *Duke University, Durham, North Carolina 27708*

[7] *Fermi National Accelerator Laboratory, Batavia, Illinois 60510*

[8] *Laboratori Nazionali di Frascati, Istituto Nazionale di Fisica Nucleare, I-00044 Frascati, Italy*

[9] *University of Geneva, CH-1211 Geneva 4, Switzerland*

[10] *Harvard University, Cambridge, Massachusetts 02138*

[11] *Hiroshima University, Higashi-Hiroshima 724, Japan*

[12] *University of Illinois, Urbana, Illinois 61801*

[13] *Institute of Particle Physics, McGill University, Montreal H3A 2T8, and University of Toronto, Toronto M5S 1A7, Canada*

[14] *The Johns Hopkins University, Baltimore, Maryland 21218*

[15] *National Laboratory for High Energy Physics (KEK), Tsukuba, Ibaraki 305, Japan*

[16] *Ernest Orlando Lawrence Berkeley National Laboratory, Berkeley, California 94720*

[17] *Massachusetts Institute of Technology, Cambridge, Massachusetts 02139*

[18] *University of Michigan, Ann Arbor, Michigan 48109*

[19] *Michigan State University, East Lansing, Michigan 48824*

[20] *University of New Mexico, Albuquerque, New Mexico 87131*

[21] *The Ohio State University, Columbus, OH 43210*

[22] *Osaka City University, Osaka 588, Japan*

[23] *Universita di Padova, Istituto Nazionale di Fisica Nucleare, Sezione di Padova, I-35131 Padova, Italy*

[24] *University of Pennsylvania, Philadelphia, Pennsylvania 19104*

[25] *Istituto Nazionale di Fisica Nucleare, University and Scuola Normale Superiore of Pisa, I-56100 Pisa, Italy*

[26] *University of Pittsburgh, Pittsburgh, Pennsylvania 15260*

[27] *Purdue University, West Lafayette, Indiana 47907*

[28] *University of Rochester, Rochester, New York 14627*

[29] *Rockefeller University, New York, New York 10021*

[30] *Rutgers University, Piscataway, New Jersey 08854*

[31] *Academia Sinica, Taipei, Taiwan 11529, Republic of China*

[32] *Texas A&M University, College Station, Texas 77843*

[33] *Texas Tech University, Lubbock, Texas 79409*

[34] *University of Tsukuba, Tsukuba, Ibaraki 305, Japan*

[35] *Tufts University, Medford, Massachusetts 02155*

[36] *University of Wisconsin, Madison, Wisconsin 53706*

[37] *Yale University, New Haven, Connecticut 06511*

Bibliography

[1] S. L. Glashow, Nucl. Phys. **22**, 579 (1961).

[2] N. Cabibbo, Phys. Rev. Lett. **10**, 531 (1963).

[3] S. Weinberg, Phys. Rev. Lett. **19**, 1264 (1967).

[4] A. Salam, in *Elementary Particle Theory: Relativistic Groups and Analyticity (Nobel Symposium No. 8)*, edited by N. Svartholm (Almqvist and Wiksell, Sweden, 1968), p. 367.

[5] S. L. Glashow, J. Illiopoulous, and L. Maiani, Phys. Rev. D**2**, 1285 (1970).

[6] M. Kobayashi and M. Maskawa, Prog. Theor. Phys. **49**, 652 (1973).

[7] J. C. Collins and D. E. Soper, Phys. Rev. D**16**, 2219 (1977).

[8] K. O. Mikaelian, Phys. Rev. D**17**, 750 (1978).

[9] G. P. Lepage, Jour. of Comp. Phys. **27**, 192 (1978).

[10] K. O. Mikaelian, M. A. Samuel, and D. Sahdev, Phys. Rev. Lett. **43**, 746 (1979).

[11] R. W. Brown, D. Sahdev, and K. O. Mikaelian, Phys. Rev. D**20**, 1164 (1979).

[12] G. P. Lepage, CLNS-80/447.

[13] C. J. Goebel, F. Halzen, and J. P. Leveille, Phys. Rev. D**23**, 2682 (1981).

[14] S. J. Brodsky and R. W. Brown, Phys. Rev. Lett. **49**, 966 (1982).

[15] R. W. Brown, K. L. Kowalski, and S. J. Brodsky, Phys. Rev. D**28**, 624 (1983).

[16] H. Minemura, *et al.*, Nucl. Inst. Meth. A**238**, 18 (1985).

[17] W. H. Press, Section 13.5 in *Numerical Recipes: The Art of Scientific Computing.*

[18] J. Cortés, K. Hagiwara, and F. Herzog, Nucl. Phys. B**278**, 26 (1986).

[19] U. Baur and D. Zeppenfeld, Nucl. Phys. B**308**, 127 (1988).

[20] S. Cihangir, *et al.*, Nucl. Inst. Meth. A**267**, 249 (1988).

[21] L. Balka, *et al.*, Nucl. Inst. Meth. A**267**, 272 (1988).

[22] Y. Fukui, *et al.*, Nucl. Inst. Meth. A**267**, 280 (1988).

[23] S. Bertolucci, *et al.*, Nucl. Inst. Meth. A**267**, 301 (1988).

[24] Yasuoka, *et al.*, Nucl. Inst. Meth. A**267**, 315 (1988).

[25] R. G. Wagner, *et al.*, Nucl. Inst. Meth. A**267**, 330 (1988).

[26] S. R. Hahn, *et al.*, Nucl. Inst. Meth. A**267**, 351 (1988).

[27] T. Devlin, *et al.*, Nucl. Inst. Meth. **A268**, 24 (1988).

[28] G. Ascoli, *et al.*, Nucl. Inst. Meth. **A268**, 33 (1988).

[29] G. Ascoli, *et al.*, Nucl. Inst. Meth. **A268**, 41 (1988).

[30] F. Bedeschi, *et al.*, Nucl. Inst. Meth. **A268**, 50 (1988).

[31] F. Snider, *et al.*, Nucl. Inst. Meth. **A268**, 75 (1988).

[32] D. Amidei, *et al.*, Nucl. Inst. Meth. **A269**, 51 (1988).

[33] G. Ascoli, *et al.*, Nucl. Inst. Meth. **A269**, 63 (1988).

[34] G. Drake, *et al.*, Nucl. Inst. Meth. **A269**, 68 (1988).

[35] E. Barsotti, *et al.*, Nucl. Inst. Meth. **A269**, 82 (1988).

[36] G. W. Foster, *et al.*, Nucl. Inst. Meth. **A269**, 93 (1988).

[37] F. Abe, *et al.*, CDF Collaboration, Nucl. Inst. Meth. **A271**, 387 (1988).

[38] J. Proudfoot, in the proceedings of *Calorimetry for the Superconducting Supercollider*, Alabama, 1989, edited by R. Donaldson and M. Gilchriese (World Scientific, Singapore, 1989).

[39] U. Baur and E.L. Berger, Phys. Rev. **D41**, 1476 (1990).

[40] U. Baur, E. W. N. Glover, and W. J. Stirling, Phys. Rev. **D42**, 798 (1990).

[41] The CDF Collaboration, CDF/DOC/PUBLIC/**1172**, October 9. 1990.

[42] J. Alitti, *et al.*, UA2 Collaboration, Phys. Lett. **B277**, 194 (1992).

[43] U. Baur, S. Errede, and J. Ohnemus, Phys. Rev. **D48**, 4103 (1993).

[44] U. Baur, T. Han, and J. Ohnemus, Phys. Rev. **D48**, 5140 (1993).

[45] A. D. Martin, R. G. Roberts, and W. J. Stirling, Phys. Lett. **306B**, 145 (1993).

[46] F. Abe, *et al.*, Phys. Rev. Lett. **73**, 225 (1994), Phys. Rev. **D50**, 2966 (1994).

[47] U. Baur, T. Han, and J. Ohnemus, FSU-HEP-940307.

[48] D. Benjamin, *et al.*, CDFnote 2575 (1994).

[49] J. D. Lewis, *et al.*, CDF note 2858, to be submitted to Nucl. Inst. Meth.

[50] F. Abe, *et al.*, CDF Collaboration, Phys. Rev. Lett. **74**, 850 (1995)

[51] F. Abe, *et al.*, CDF Collaboration, Phys. Rev. Lett. **74**, 1936 (1995).

[52] F. Abe, *et al.*, Phys. Rev. Lett. **74**, 2626 (1995).

[53] H. Aihara, *et al.*, MAD/PH/871, to be published in "Electroweak Symmetry Breaking and Beyond the Standard Model."

[54] T. Han, in AIP Conference Proceedings 350 "International Symposium on Vector Boson Self-interactions," Los Angeles, CA, Feb. 1995.

[55] R. Brown, in AIP Conference Proceedings 350 "International Symposium on Vector Boson Self-interactions," Los Angeles, CA, Feb. 1995.

[56] S. Abachi, *et al.*, DØ Collaboration, hep-ex/9612002, Fermilab-Pub-96/434-E.

[57] T. Barklow, *et al.*, hep-ph/9611454, to appear in the Proceedings of the 1996 DPF/DPB Summer Study on New Directions in High-Energy Physics, June 25–July 12, 1996, Snowmass, CO, USA.

[58] http://www.cern.ch/Press/Releases96/PR05.96ELEP2StartUp.html.